COMPUTATIONAL AND EXPERIMENTAL STUDIES OF GLUTAMATE RECEPTOR LIGAND BINDING DOMAINS

by

John Belcher

A dissertation submitted to Johns Hopkins University in conformation with the
requirements for the degree of Doctor of Philosophy

Baltimore, Maryland
April 2018

Abstract

Ionotropic glutamate receptors (iGluRs) are proteins that allow for the propagation of electrical signals in neurons. These proteins work by opening a transmembrane pore in response to the binding of the excitatory neurotransmitter glutamate by an extracellular ligand binding domain (LBD). Here we investigate how the free energy landscape of a prokaryotic analog to these eukaryotic iGluRs, GluR0, changes in response to the binding of various ligands. We find a very flexible LBD, which clamps down in response to ligand binding. We present potential of mean force (PMF) maps of the GluR0 LBD in apo, glutamate, and serine bound forms. In addition to our computational work on GluR0, experiments were done to observe shape changes in AMPA receptor LBD dimers. Analytical ultracentrifugation (AUC) was performed on two GluA2 mutants, one biased towards the desensitized state, the other not. We performed sedimentation velocity experiments on the two mutants, and use the c(s) fits to observe changes in the f/f0 values. Finally we used principal component analysis (PCA) to analyze the trajectories of molecular dynamics simulations in NMDA receptors. Analysis of the trajectories shows how the LBD explores the ensemble of conformations available to it, and how that changes upon ligand binding.

Thesis advisor: Dr. Albert Lau

Second reader: Dr. Cynthia Wolberger

Thesis committee: Dr. Tom Woolf, Dr. Jeff Gray, Dr. Mario Amzel

Acknowledgements

I'm incredibly fortunate to have had the support of an amazing group of people throughout my time in graduate school. First and foremost I need to thank my parents, Jerry and Marilyn Belcher, their constant love and support has been a boon throughout my career.

I'm grateful to have spent my time at Hopkins surrounded by some of the most accomplished scientists around, none more so than Dr. Albert Lau. Albert has been everything one could ask for in a PI, and his advice and teaching will be of use for all my future endeavors. I must thank the other members of my committee, Dr. Cynthia Wolberger, Dr. Mario Amzel, Dr. Tom Woolf, and Dr. Jeff Gray, for all their support and expertise.

I'm thankful for all the time spent with my fellow Lau lab members: Dr. Alvin Yu, Tyler Wied, and Afif Bandak. Alvin always kept me on my toes with his sharp arguments. Tyler managed to laugh at my jokes, and Afif proved to be a great roommate.

Finally, I have to thank my loving girlfriend, Kathleen Mazurek. Her and her family helped me find a second home in Baltimore, and I can't thank them enough.

Table of Contents

List of Figures

List of Tables

Chapter 1: Introduction to Ionotropic Glutamate Receptors

1.1: Ionotropic Glutamate Receptors and Their Role in Neuronal Signaling

The nervous system is a complex network of nerves and neurons that transmit electrical signals across the body. Synapses exist to allow neurons to convert electrical signals into chemical signals, and then back into electrical signals. This is a four step process that begins with a flood of calcium into the presynaptic neurons. This triggers an exocytosis of vesicles carrying neurotransmitters such as glutamate or acetylcholine. These neurotransmitters enter the synaptic cleft, where they bind to their target receptor. This binding induces structural changes in these receptors, which allow ions to flow through the membrane [Figure 1] (Purves et al. 2001). In the mammalian system the majority of these excitatory interactions are mediated by the amino acid glutamate (Institute of Medicine 2011). Correspondingly, there is a class of transmembrane receptors, ionotropic glutamate receptors (iGluRs), which bind glutamate in order to propagate these signals. The structure and function of these receptors are crucial to proper brain development, learning, and memory formation. These receptors are assosciated with multiple neurological diseases and disorders, including Alzheimer’s, depression, and traumatic brain injury (Karakas et al. 2015).

1.2 Structure of Ionotropic Glutamate Receptors

iGluRs can be divided into four families, that can be distinguished by their response to three agonists [Figure 2]. Those that respond most to α-amino-3-hydroxy-5-methyl-4-

isoxazole propionic acid (AMPA) are called AMPA receptors, and follow a GluA* naming convention. Those that respond to *N*-methyl-D-aspartate are called NMDA receptors, and obey a GluN* naming convention. Those that respond to kainate are called kainate receptors, and obey a GluK* naming convention. Finally there are the delta receptors, which although not actually glutamate binding receptors, show ~18%-25% sequence homology with the NMDA, AMPA, and kainate receptors and are involved in synaptogenesis and synaptic plasticity (Dingledine et al. 1999). Although they share a similar overall structure, these receptor subtypes show differences in pharmacology, unique activation, deactivation and desensitization kinetics, selective permeability, single-channel properties, and the unique roles they play in different forms of both neuronal and glial signaling (Armstrong et al. 2000).

iGluRs share a modular structure consisting of four distinct domains: an amino terminal domain (ATD), a transmembrane domain (TMD), a ligand binding domain (LBD), and a carboxylic terminal domain (CTD) [Figures 3 and 4].

The amino terminal domain sits outside the cell as a clamshell-like structure that is thought to aid in the formation of higher order complexes in all families of glutamate receptors (Bigge et al. 1999). It also interacts with extracellular proteins to aid with the organization of iGluRs within the membrane (Furukawa 2012). It is not necessary for the function of the receptor in the AMPA and kainate families, with both forming functional receptors in the absence of this amino terminal domain (Furukawa 2012). In the NMDA receptor however, it has two clear and defined functions. The first is tuning the probability of the NMDAR LBD being in the open state (Gielen et al. 2009; Yuan et al. 2009). The second is serving as a site for allosteric modulation, with the NTD providing a binding site for zinc, which lowers channel activity in the pore (Choi & Lipton, 1999; Low et al. 2000).

The LBD is a bi-lobed glutamate binding pocket. The first lobe (D1) is adjacent to the M1 helix. The second lobe (D2) of this binding domain comes in between the M3 and M4 helices [Figure 4]. It is here that the conformational changes associated with gating begin. The binding of an agonist ligand in the LBD induces a conformational change that is transmitted through peptide linkers to the TMD. This change opens the pore and allows depolarization to occur (Krieger et al. 2015). In all AMPA and Kainate receptors, this agonist is glutamate. In NMDA receptors two of the ligand binding domains, GluN1 and GluN3, instead bind glycine and D-serine (Furukawa et al. 2003, Yao et al. 2008). So far, crystal structures of iGluR dimer have all been constructed as homodimers, with the exception of the NMDA receptor, which has been found as a GluN1/GluN2A heterodimer (Furukawa et al. 2005). It has been shown that interactions at this dimer interface affect the extent of desensitization and the speed with which the receptor deactivates (Schauder et al. 2013, Armstrong et al. 2006).

The TMD consists of three transmembrane helices (M1, M3, and M4) along with a cytoplasm facing transmembrane re-entrant loop (M2). The M1, M3, and M4 helices combine to form a fourfold symmetric pore that resembles an inverted potassium channel (Traynelis et al. 2005). This TMD is selective for the cations Na^+, K^+ and $Ca2^+$. In NMDA receptors, this TMD is blocked by a Mg^{2+} under physiological conditions, and must be removed by depolorization before ions can flow through (Blanke et al 2009). The TMD is attached to the CTD, which interacts with intracellular proteins to control the spatial and temporal regulation of these receptors (Shepard and Huganir, 2007).

Functional glutamate receptors are assembled as dimers of dimers to form a tetrameric complex. In the all of the AMPA ,GluA(1-4), and most of the kainate, GluK(1-3), the subunits can form both homo and hetero tetramers (Dingledine et al. 1999). The last two kainate receptors, GluK4 and GluK5, both require two of the other kainate receptors to form a functional receptor (Dingledine et al. 1999). NMDA receptors are unique in that they are all obligate heterotetramers. They assemble by combining a glutamate binding domain, GluN2, with one of two glycine binding domains, either GluN1 or GluN3 (Dingledine et al. 1999).

1.3 GluR0, a Prokaryotic Glutamate Receptor

GluR0 is a hypothetical precursor to eukaryotic glutamate receptors, discovered in the freshwater cyanobacteria Synechocystis PCC 6803 (Chen et al. 1999). This protein was found by performing a BLAST (Basic Local Alignment Search Tool) search on the Synechocystis genome with the first three membrane-associated segments of the rat AMPA receptor, GluA2. This search turned up a protein similar to the eukaryotic iGluRs, but with some key differences [Figure 5]. To begin with, while it contains regions similar to the S1 and S2 sequences of the iGluR ligand binding domain, and was subsequently found to be able to bind glutamate, it lacked any response to AMPA, NMDA, or kainate (Chen et al. 1999). Unlike the eukaryotic glutamate receptors though, GluR0 does respond to L-serine, L-alpha-amino adipic acid, and D,L-alpha-aminopimelic acid (Chen et all. 1999). Crystal structures of both the serine and glutamate bound states reveal differences in the ways GluR0 binds ligands as compared to the eukaryotic iGluRs

(Mayer et al. 2001). In the case of serine, GluR0 requires additional water molecules to occupy the binding cleft in order to bind serine (Mayer et al. 2001). In the case of glutamate, the ligand occupies an ‘extended’ conformation, with its γ-carboxyl pointed towards Asn51 in the upper lobe (Mayer et al. 2001) [Figure 6]. This is in contrast with the eukaryotic iGluRs which adopt a ‘bent’ conformation, γ-carboxyl pointed down towards the lower lobe [Figure 6] (Mayer et al.2001). It is speculated by Mayer that, due to the difference in how GluR0 and eukaryotic iGluRs bind ligands, that the conformational changes induced by the ligands should also differ (Mayer et al. 2001).

The transmembrane domain of GluR0 is also unique. Rather than the Na^+, K^+ and $Ca2^+$ ions that eukaryotic gluRs allow through, GluR0 contains a gating region and transmembrane topology more similar to the potassium channel KcsA, and thus only lets through potassium ions (Chen et al. 1999, Yalini et al. 2003). These ion channels show many spontaneous openings, even in the unliganded state (Cheng et al. 2002). These channels have slower activation kinetics than the eukaryotic iGluRs, GluR0 being (290 ± 15 ms) versus the GluA2 rise time of (18 ± 3 ms) (Chen et al. 1999). The structural basis for slower kinetics and spontaneous activation is currently unknown.

1.4 Overview of Data Presented Here

The central question of this thesis is in the similarities and differences in large-scale conformational transitions exhibited by the LBDs of these iGluRs. Since the LBD is the ‘control center’ of the receptor understanding its molecular mechanics can help us understand both how the receptor functions, and the molecular basis of functional differences among the iGluRs. This focus on motion serves to complement the multiple static structures currently available of the various iGluRs, obtained through means such as X-ray crystallography or electron microscopy. Using a combination of computational and experimental techniques we can observe both the ensemble of states available to these LBDs, how the binding of ligands affects the closure of the LBD, and the motions by which the LBD navigates that ensemble.

In Chapter 2 we focus on simulations of the monomeric ligand binding domain of GluR0. Here we begin with crystal structure of the LBD in various binding states: apo, glutamate bound, and serine bound. Using umbrella sampling we show which states, either open or closed, that the LBD can access in either the apo or ligand bound state, and we see how the change in glutamate binding modes between GluR0 and eukaryotic iGluRs effects the changes observed upon ligand binding in the LBDs. In contrast with the eukaryotic receptors, which have been studied using dynamic methods such as NMR or FRET, GluR0 has not been subject to the same level of investigation. Interestingly, despite the lack of an open apo crystal structure, we show that this state should be accessible to the GluR0 LBD. Having generated an ensemble of structures and knowing the energetics associated with each of those structures, we attempted to use small angle X-ray scattering (SAXS) to see if our PMF could predict experimental SAXS curves of the GluR0 monomer. Finally, we use principal component analysis (PCA) to see how the LBD explores the conformations available to it. We show that there is a rearrangement of principal components (PCs) that occurs upon ligand binding for glutamate, but not for serine.

Chapter 3 looks at the structural rearrangements that occur during desensitization in the AMPA receptor GluA2. We construct modified versions of the GluA2 LBD, attaching a linker region to allow for the creation of cysteine linked dimers. We made two variants of the GluA2 LBD, one with a mutation designed to promote dimerization, one with a set of mutations designed to inhibit it. We then use analytical ultracentrifugation to observe the effect of these mutations on the shape of the GluA2 dimers.

Chapter 4 uses PCA to analyze the motions that various GluNs use to traverse their ensemble. We perform PCA on multiple GluN ligand binding domains including both glutamate and glycine binding domains. We show how these modes change upon ligand binding, and how the LBD samples the ensemble of structures available to it. We then models these motions onto the full length NMDA receptor, and see how they affect distances between LBDs within the tetramer.

Figure 1

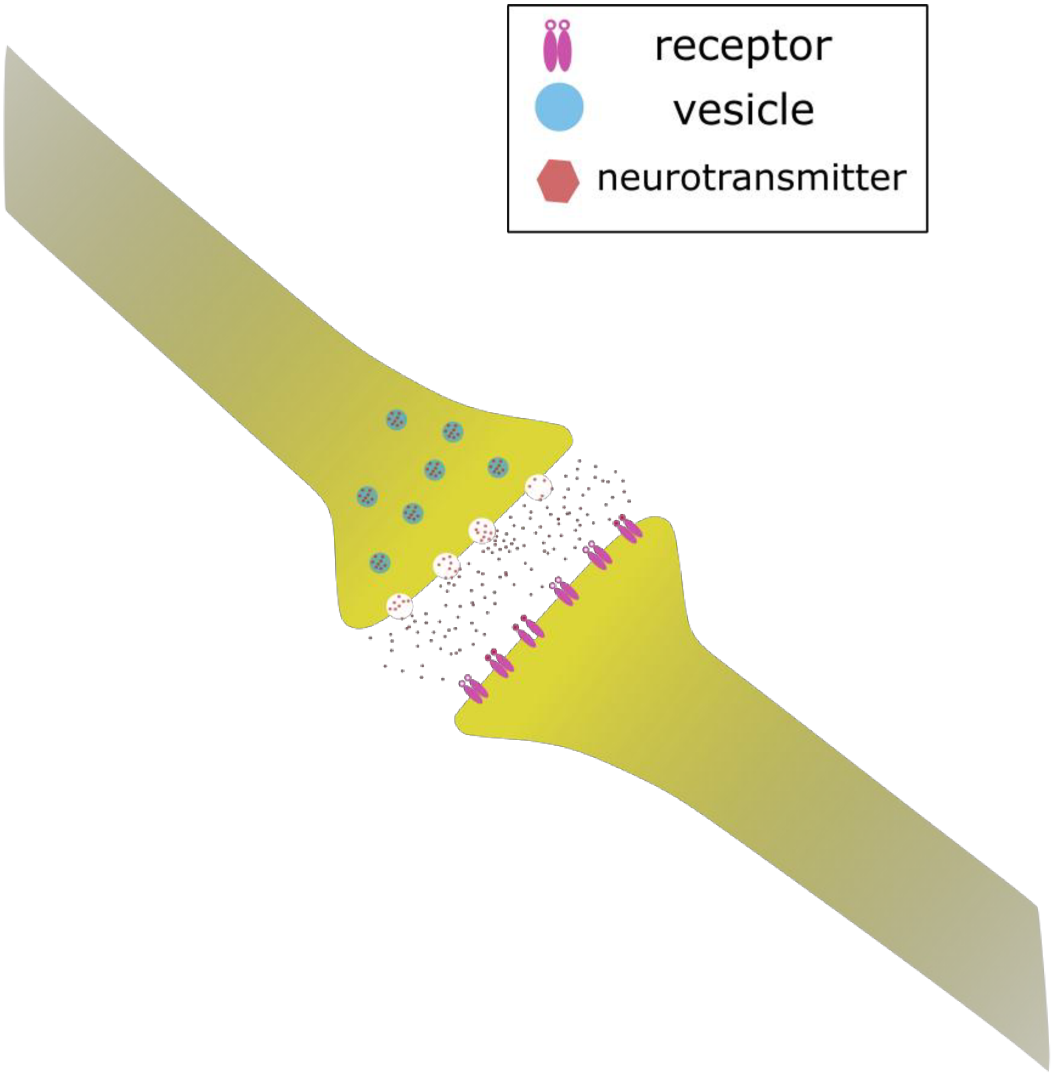

Fig 1. **Model of a synapse.**

Synaptic vesicles within the upper lobe are loaded with neurotransmitters. These vesicles fuse with the presynaptic membrane, and release neurotransmitters into the synaptic gap. These neurotransmitters bind to the receptors and induce depolarization in the synaptic cell.

Figure 2

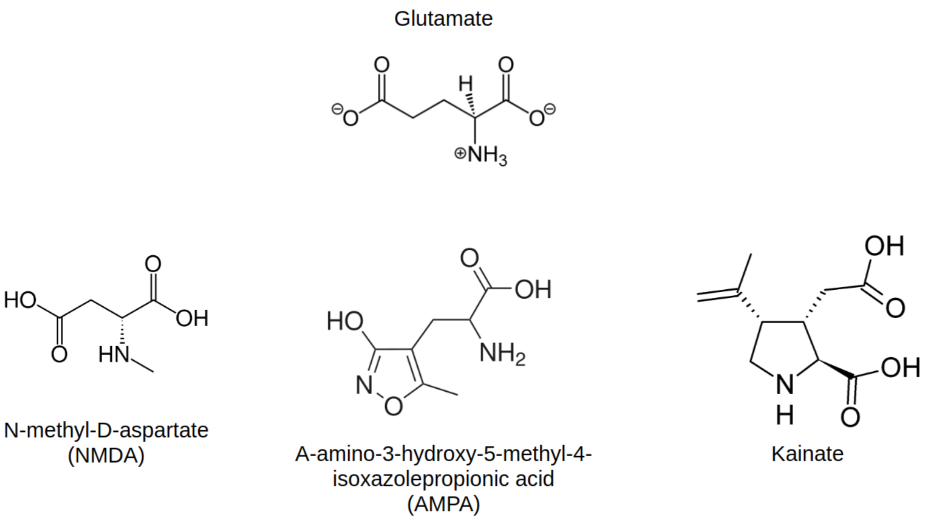

Glutamate

N-methyl-D-aspartate
(NMDA)

A-amino-3-hydroxy-5-methyl-4-
isoxazolepropionic acid
(AMPA)

Kainate

Fig 2. **Chemical structures of glutamate and specific agonists for each GluR family.**

Figure 3

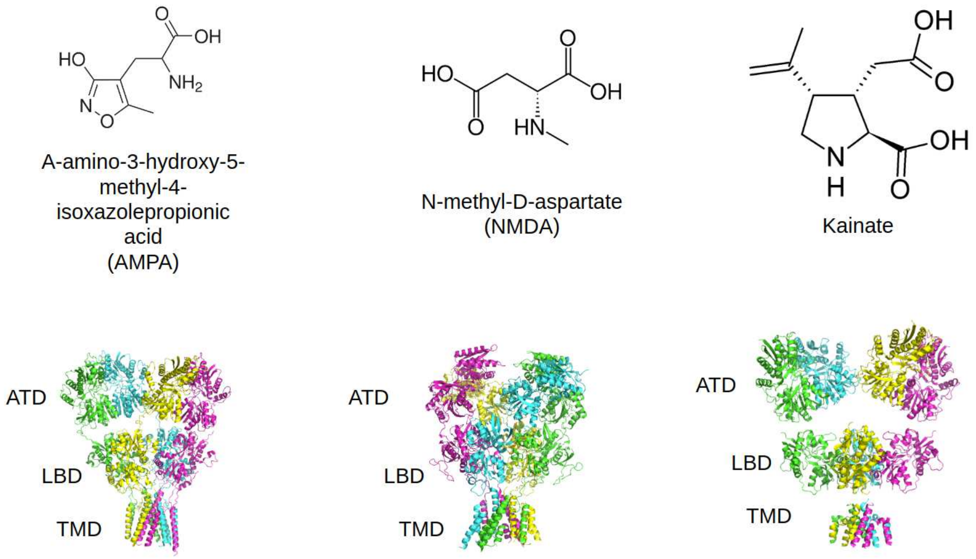

Fig 3. **Full length structures for the NMDA, AMPA, and Kainate structures respectively.**

Structures of three main iGluRs. From left to right: AMPA receptor in the competitive antagonist MPQX bound state (PDB: 5KK2), NMDA receptor in the glycine/glutamate bound state (PDB: 5IOU), and kainate receptor in the presence of the agonist 2S,4R-4-methylglutamate (PDB: 5KUF). All iGluRs assemble as dimers of dimers, with the AMPA and kainate shown as homomers, while the NMDAR is a heteromer. Each iGluR shares a common architecture, with the LBD, TMD, and ATD shown here.

Figure 4

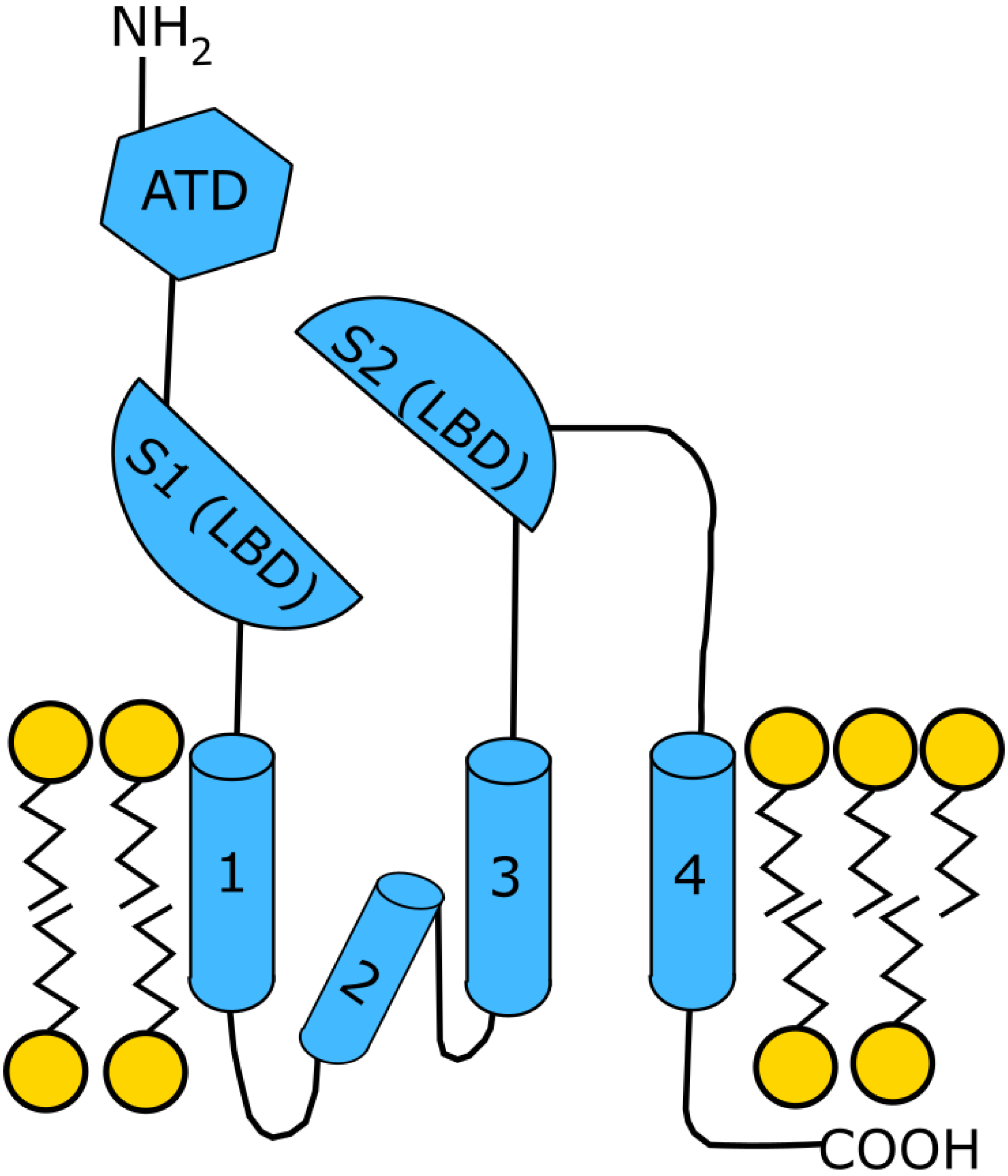

Fig 4. **Eukaryotic Glutamate Receptor Schematic.**

Cartoon schematic showing the main structures regions observed in all families of iGluRs. A well-defined amino terminal domain, the ligand binding sites S1 and S2, and the transmembrane topology

Figure 5

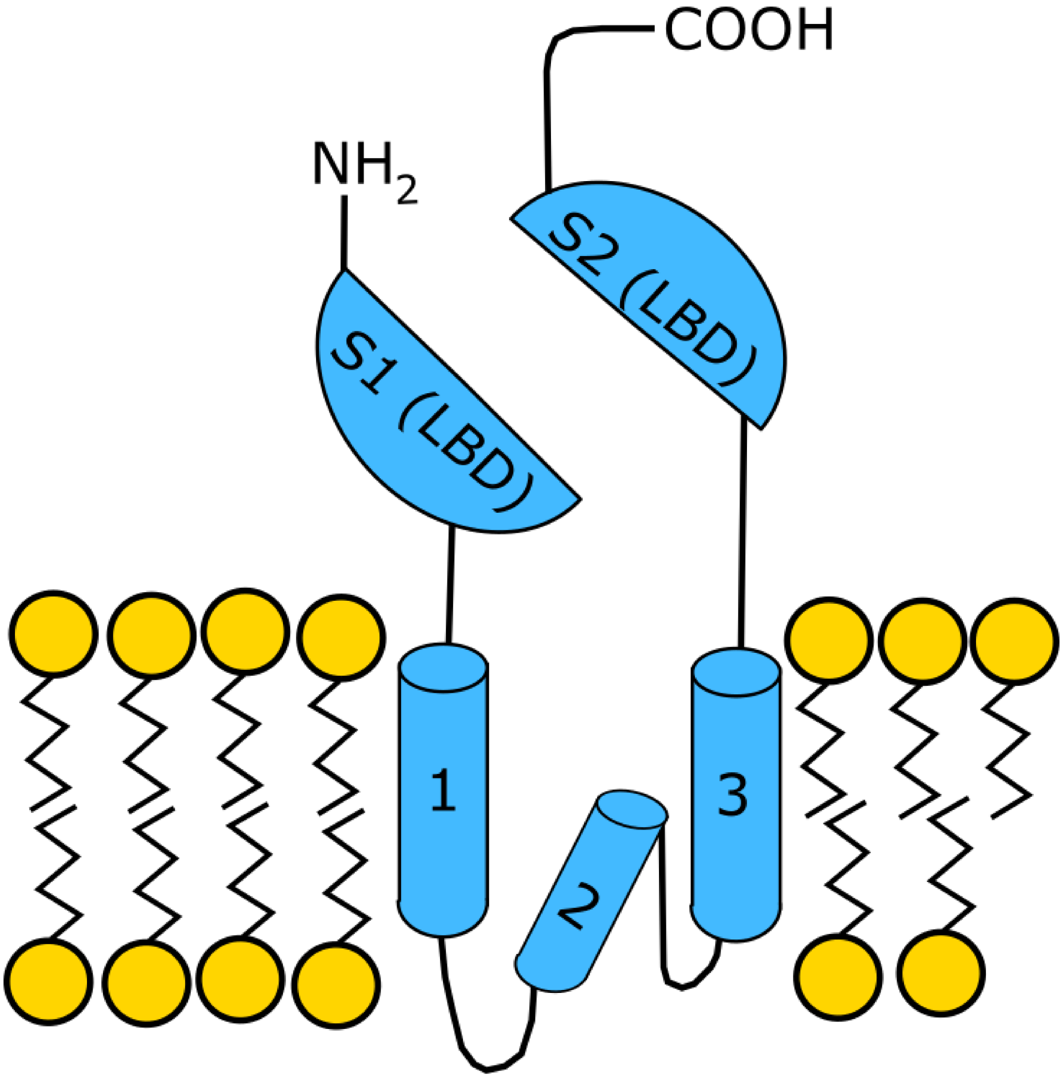

Fig 5. **Schematic of prokaryotic GluR0**

Cartoon schematic showing the main structures observed in the prokaryotic GluR0, and how these changes differ from the eukaryotic iGluRs. GluR0 lacks the structured amino terminal domain found in the other glutamate receptors, is missing one of the transmembrane helices, and features an extracellular C-terminus.

Figure 6

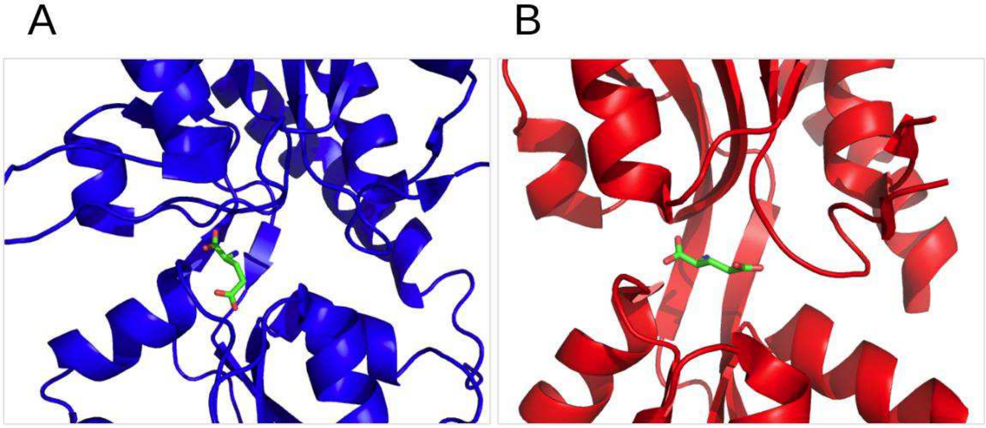

Fig 6. **Schematic of the differences in glutamate binding in GluR0 and GluA2**

How glutamate, colored green, binds within the cleft of the the ligand binding domain for GluA2 (PDB: 4Z0I, colored blue) and GluR0 (PDB: 1ii5, colored red) respectively. In GluA2, on the left, glutamate adopts a ‘relaxed’ conformation, and in GluR0 the glutamate adopts an ‘extended’ conformation. This change means that the γ-carboxy of glutamate makes no contact with the lower lobe of the ligand binding domain in GluR0.

Chapter 2: Computational and Experimental Characterization of GluR0

Reproduced in part from:

Ionotropic Glutamate Receptor Technologies, Neuromethods vol. 106 chap 9

DOI 10.1007/978-1-4939-2812-5_9, Springer Science+Business Media New York 2016

by

Alvin Yu, Tyler Wied, John Belcher, and Albert Y. Lau

Molecular Dynamics (MD) simulations are a tool for investigation biological macromolecules beyond the static structures of x-ray crystallography and electron microscopy. This ability to see these molecules in motion allows one to explore conformations of the macromolecule that are unreachable by experimental methods alone. Within the case of ionotropic glutamate receptors (iGluRs), this technique allows us to study the complex network of actions and interactions that govern the function of the receptor. This chapter briefly introduces the theory behind these MD simulations, the Umbrella Sampling technique, and their use on the GluR0 LBD. The results of these computational techniques are then tested using Small Angle X-Ray Scattering (SAXS)

2.1 Molecular Dynamics Theory

To explain a molecular dynamics simulation is relatively straightforward. Newton's laws of motion are used to evolve the positions and velocities of a system of atoms. For a two-atom system, this is a relatively trivial task. For an 80,000 atom system, this requires advanced computing resources. Regardless of the size of the system or the software package chosen to run it on, there are commonalities within the force fields that will be applied to the atoms. Most molecular dynamics force fields will include the following terms:

$$U(\mathbf{R}) = \sum_{bonds} K_b(b - b_0)^2 + \sum_{angles} K_\theta(\theta - \theta_0)^2 + \sum_{dihedrals} K_\phi\,[1 + \cos(n\phi - \delta)] + \sum_{\substack{Improper \\ Dihedrals}} K_\chi(\chi - \chi_0)^2 + \sum_{nonbonded} \left\{ \frac{q_i q_j}{\varepsilon\, r_{ij}} + \varepsilon_{ij}\left(\frac{R_{minij}}{r_{ij}}\right)^{12} - 2\left(\frac{R_{minij}}{r_{ij}}\right)^{6} \right\} \qquad (1)$$

The ‘bonded’ terms are the bonds, angles, dihedrals, and improper dihedrals. The first term contains b, the bond distance, b_0, the equilibrium value for bond distance, and K_b, the force constant. The angle term is formatted similarly, with θ, the valence angle, θ_0, the equilibrium value, and K_θ, the force constant for the angle. The dihedral terms are represented by a force constant, K_ϕ, the dihedral angle, ϕ, and the multiplicity and phase for the dihedral angle, *n* and δ respectively. The improper dihedral term, a measure of out of plane distortion, contains the angle χ, its equilibrium value χ_0, and the force constant K_χ. The ‘nonbonded’ terms are the electrostatic interactions treated using a Coulombic term and the interatomic repulsion and dispersion interactions treated using a Lennard-Jones “6-12” term. In these non-bonded interactions q_i and q_j are the partial atomic charges on atoms *i* and *j*; ε is the dielectric constant; r_{ij} is the distance between atoms *i* and *j*; and the Lennard-Jones potential well depth and minimum interaction radius are ε_{ij} and $R_{min,ij}$.

The above parameters describe all that is necessary to run a “brute force” simulation. However, complex systems with high energy barriers such as an iGluR ligand binding domain will require more tools to fully explore the energy landscape in ordinary time. Numerous methods have been developed to deal with these limitations, one of which, umbrella sampling will be explained below.

2.2 Umbrella Sampling

Umbrella sampling begins with the choice of an order parameter. A well-chosen order parameter is key to a successful umbrella sampling simulation. In theory anything could be an order parameter, a distance, an angle, or a deviation from a reference state. A well-chosen order parameter will traverse the conformational states of the protein, and differentiate between these states. Choosing an appropriate order parameter for a given system often requires a mix of physical intuition and prior knowledge of the chemical process under consideration.

Once an order parameter, ξ, is chosen, our quantity of interest is the free energy, or potential of mean force (PMF), $W(\xi)$, along ξ:

$$W(\xi) = W(\xi^*) - k_B T \ln\left[\frac{\langle\rho(\xi)\rangle}{\langle\rho(\xi^*)\rangle}\right] \qquad (2)$$

where ξ^* is an arbitrary reference value, $\langle\rho(\xi)\rangle$ is the Boltzmann weighted average distribution function along ξ, k_b is Boltzmann's constant, and T is the temperature.

Although in principle it would be possible to arrive at $W(\xi)$ by running brute force simulations, in practice energy barriers can impede sampling along ξ. In the finite amount of time that a simulation can run, low energy regions would be highly sampled, while higher energy regions would be sampled rarely, and states on the other side of barriers higher than k_bT may not be sampled at all [Figure 1]. This poor sampling would lead to unreliable statistics from which to calculate the PMF. One of the solutions to this lack of sampling is the umbrella sampling technique, developed by Torrie and Valleau. In this technique, 'windows' are created along a reaction coordinate ξ. These windows are biased towards a reference value of ξ through the use of a harmonic restraining potential, with the complete set of ξ values spanning the conformational space of interest. The effect of this bias is to ensure sampling in regions that may not be energetically connected.

It is possible to compute the unbiased PMF of an individual sampling window from the biased probability distribution through the following:

$$W_i(\xi) = W(\xi^*) - k_b T \, ln\left[\frac{\langle\rho(\xi)\rangle_{(i)}}{\langle\rho(\xi^*)\rangle}\right] - w_i(\xi) + F_i \qquad (3)$$

Where F_i is the free energy associated with introducing the window potential, $w_i(\xi)$, and $\langle\rho(\xi)\rangle_{(i)}$ is the biased distribution function generated by the i-th window. In the one window case, F_i can be left undetermined, since the probability distribution can only determine the PMF up to a constant. In the multi-window case however, we have different weights to each of our different distributions, and must figure out how to weight them accordingly.

Numerous approaches have been developed to accomplish this task (Roux 1995, Kastner 2011). We will discuss only one of these approaches, the weighted histogram analysis method (WHAM) (Kumar et al. 1992), although other valid approaches are certainly available. WHAM works through two equations, known as the WHAM equations:

$$\langle\rho(\xi)\rangle = \sum_{i=1}^{N} n_i \langle\rho(\xi)\rangle_{(i)} \text{ x } \left[\sum_{j=1}^{N} n_j e^{-[w_j(\xi)-F_j]/k_B T}\right]^{-1} \qquad (4)$$

and

$$e^{-F_i/k_B T} = \int \langle\rho(\xi)\rangle \, e^{-w_i(\xi)/\mathrm{k_B} T} d\xi \quad (5)$$

Where N is the number of simulations, and n_i are the number of sampling data points used to generate each biased distribution function. Equations (4) and (5), are interdependent, with F_i and $\langle \rho(\xi) \rangle$ as unknowns. WHAM uses an iterative process to solve for $\langle \rho(\xi) \rangle$ and F_i until self-consistency is achieved. The equations above are written in terms of a one-dimensional ξ. The approach can be applied to multi-dimensional scenarios as well.

2.3 Umbrella Sampling of GluR0

This study used all atom molecular simulations, combined with umbrella sampling, to reveal the energetics of opening and closing of the GluR0 S1S2 ligand binding domain, in its apo, serine, and glutamate bound forms. The study began with crystal structures from the Mayer lab, of GluR0 in all three of the above states. Missing sidechains were built in using SCWRL, and missing backbone atoms using MODELLER (Wang et al. 2008, Sali et al 1993, Fiser et al. 2000). Initial configurations were generated using a targeted MD simulation, in which the two lobes of the LBD were moved apart in vacuum along the chosen order parameters, ξ_1 and ξ_2 For the GluR0 simulation ξ_1 represents the distance between the center of mass of the 54th and 55th residues and the 124th, 125th, and 126th. ξ_2 represents the distance between the center of mass of the 13th, 14th and 17th residues and the center of mass for the 143rd and 144th residues [Figure 2]. Previous studies by the Lau lab have used similar order parameters on iGluR LBDs, yielding good results. Starting from the initial closed conformation, new windows were created by incrementally increasing the values of ξ_1 and ξ_2 in vacuum. After this initial setup was complete, the windows were solvated with explicit waters, and 150 mM NaCl. Additional sodium and chlorine atoms were then added to neutralize the charge of the protein and its ligands. Any crystallographically observed waters were kept in their original positions. After this setup, the system must then be equilibrated before production runs can begin. First, the protein and ligand atoms are held fixed while dynamics are carried out on the solvent. Next, dynamics are carried out in the presence of stabilizing restraining potentials on the protein and ligand. These restraints are gradually reduced over the course of the equilibration, which is carried out in the constant atom number, volume, and temperature (NVT) ensemble. Finally, after these restraints have been removed, the simulation is transitioned to a constant pressure (NPT) ensemble. In all steps of the equilibration involving non-fixed protein and ligand atoms, the umbrella restraints on ξ_1 and ξ_2 are also applied, there is a restraining potential keeping the ligand tethered to the binding pocket, as well as weak restraints on the COM of three regions in the core of lobe 1. The latter restraint, which does not hinder inter-lobe dynamics, prevents translation and rotation of the protein during the production phase of the simulations.

The simulations enter production phase after equilibration has completed. Here, the values for ξ_1 and ξ_2 in each window *i* are recorded, which contribute to the biased distribution function $\langle\rho(\xi_1,\xi_2)\rangle_{(i)}$. For NPT runs in GluR0 we used a two femtosecond timestep, and ran 102 windows for 1.2 ns each, yielding ~120 ns of simulation time.

Presented here are the results of the umbrella sampling simulations [Figures 3-5].

We start with apo PMF in figure 3. This PMF features a broad free energy basin, with the vast majority of the PMF falling below 2 kcal/mol. This indicates a high degree of conformational flexibility in the absence of ligand. While the only apo crystal structure of GluR0 shows it in the closed state, our PMF shows that it does have access to open conformations in its apo form, with a free energy basin below 1 kcal/mol available at (ξ_1, ξ_2) = (12.5, 13 Å). The global free energy minimum is located at. This closed state minimum may explain the random activation observed in electrophysiology experiments (Chen et al. 1999).

As expected, the glu-bound LBD PMF features an energy basin that is narrower, indicating stabilized closed cleft conformations [Figure 4]. The global free energy minimum is located at (ξ_1, ξ_2) = (8.1, 10.4 Å). The minima for both the apo and glutamate bound forms of the PMF are relatively close. GluR0 only shows a negligible difference between the apo and ligand bound PMFs. This closeness suggests that glutamate binding works through an conformational selection mechanism, where a subset of previously accessible structures are stabilized by ligand binding, rather than induced fit, where ligand binding stabilizes previously less favored energetic states (Freire, 1998; Ma et al., 1999; Monod et al., 1965). This is in contrast with previously done work on the GluA2 ligand binding domain. In the case of GluA2, the minima moves ~4.1 Å between the apo and ligand bound PMFs (Yao et al 2014).

The serine bound PMF is somewhere in between the apo and glutamate bound forms [Figure 5]. A much more stable closed conformation as compared to apo form, but not as dramatically closed as the glutamate bound version. It features a similar minima at (ξ_1, ξ_2) = (7.5, 10.2 Å). The PMF shows a LBD that has access to its open state, even in this ligand bound form. The serine bound LBD shows a stable open conformation, relative to the glutamate bound PMF. This accessible open conformation may explain why serine produces weaker and slower activations compared to glutamate in previous electrophysiology experiments (Chen et al. 1999).

2.4 Principal Component Analysis of GluR0

While hinge bending motions that move diagonally across the PMF, are of great importance to the activation of iGluRs, additional motions may contribute to how the LBD explores the ensemble. Principal Component Analysis (PCA) allows us to observe motions outside of hingebending that may contribute to how the LBD explores the ensemble of states available to it. PCA calculations involve the diagonalization of the covariance matrix C_{ij} of positional deviations among an ensemble of protein structures (Grossfield et al. 2009, Levy et al 1984):

$$C_{ij} = cov(X_i, X_j) = E[(X_i - \mu_i)(X_j - \mu_j)] \quad (6)$$

Where X_i represents a specific Cα coordinate, E is an operator that denotes the mean of its argument, and μ_i is the average positional value for the i-th Cα. The ensemble, generated separately for the GluR0 LBD in either the apo- or glutamate/serine-bound state, consists of protein conformers from all umbrella sampling windows in which W(ξ_1, ξ_2) is less than 2 kcal/mol. These conformers are then weighted in such a way that all conformers with an energy less than 1 kcal/mol are counted 5 times and those with an energy between 1 kcal/mol and 2 kcal/mol are counted only once, this crude weighting allows us to approximate the actual energetics associated with the ensemble. The ratio of two Boltzmann weighted states is:

$$\frac{F(state\ 2)}{F(state\ 1)} = e^{\frac{E_1 - E_2}{kT}} \quad (7)$$

Where F(x) is the frequency of x and E_i is the energy of the i-th state. For a delta of one and a kT of .5922, this ratio is roughly five to one. Only Cα coordinates were used in the calculations. All conformers were first superimposed onto lobe 1 of a reference structure, PDBid 1IIT, 1II5, and 1IIW respectively (Mayer et al. 2001), using a selection of Cα atoms that excludes flexible loops. Next, the lobe 1 Cα atoms of the reference structure were joined to the lobe 2 Cα atoms of each simulated conformer to construct an ensemble of pseudo-rigid-body structures. The ensembles for the apo LBD contained 32797 structures, the serine bound contained 7979 structures, and the glutamate bound had 9958 structures. These structures were stitched into pseudo trajectories, and PCA performed using the Bio3d package in R (Grant et al. 2006). The axes of rotation characterizing PC1–PC3 were calculated using the DomainSelect method provided by the DynDom server (Hayward et al. 1998). Endpoint coordinates were generated using Bio3D. Lobe 1 is the ‘‘fixed’’ domain, and lobe 2 is the ‘‘moving’’ domain. For GluR0, lobe 1 is defined as residues 1-94 and 189-235, and lobe 2 is defined as residues 95–188. For the apo and serine bound forms of GluR0 the PCs that define interlobe transitions are similar to those found in the GluA2 and GluN LBDs (Yao et al. 2013). The first PC in the apo form is a hingebinding motion that accounts for the largest portion of the variance [Figure 6, Table 1]. PC2 and PC3 also follow the precedent seen in the GluA2 and GluN results, and can be described as a rocking and twisting motion [Figure 6].

The glutamate bound version of the LBD reverses the order of the first and second PCs, with PC1 showing a rocking motion, and PC1 hingebending [Figure 7, Table 1]. PC3 remains the same.

The Serine bound PCs reflect those seen in the apo state, with hinge-bending once again being the dominant motion [Figure 8, Table 1]. PC2 and PC3 are also the same, sharing the rocking and twisting motions with the apo form of the LBD.

2.5 Error Analysis

Uncertainty for the PMFs was calculated using block averaging (Zhu et al 2012). Each set of ξ_1, ξ_2 values for each window was split into 10 blocks of equal size. WHAM was used to calculate a PMF for each replicate, and then the standard deviation for each of the PMFs was calculated [Figures 9-11].

2.6 Small Angle X-Ray Scattering

Small Angle X-Ray Scattering (SAXS) is a powerful technique for determining size and shape distributions of proteins and other biological macromolecules in solution (Hayden et al 2010). SAXS is useful for working with proteins that may not crystallize, that have more than one biologically relevant conformation, and those with large regions of intrinsically disordered amino acids. SAXS works with proteins ranging from the small, kilodaltons, to gigantic gigadalton complexes (Hayden et al. 2010).

SAXS experiments start from a similar place as a crystallography experiment, with a highly collimated beam of X-rays or neutrons. These waves interact with atoms in the protein to generate secondary wavelets, and these wavelets then either constructively or destructively interfere, creating a scattering pattern [Figure 12] (Jacques et al. 2010). X-ray crystallography looks at the scattering pattern generated by individual atoms in a protein within an ordered crystal lattice, while SAXS looks at the scattering profile generated by the collective atoms within a single protein in solution. The limiting factor for resolution within these SAXS experiments is the rotational averaging of the molecules in solution, with the smallest angle that can be measured determining the greatest distance that can be characterized (Jacques et al. 2010). The scattering intensity is reported as a function of the amplitude of the scattering vector q:

$$q = \frac{4\pi\sin(\theta)}{\lambda} \quad (8)$$

where λ is the wavelength of the incident radiation, and θ is half the angle between the incident and scattered radiation elements, weighted by their scattering densities. This parameter gives information about the shape and density of the protein. One other use of the scattering profile is the generation of a Kratky plot which is a plot of $I(q) \text{ x } q^2$ vs q (Kikhney et al. 2015). This division removes the decay portion of the scattering, and allows one to distinguish between disordered and globular proteins. A bell shaped Kratky plot is indicative of a well folded globular protein, as the I(q) value for solid bodies decays as s approaches values of $I(q)/q^4$ (Kikhney et al. 2015). Kratky plots with plateaus for large values of q are characteristic of unfolded proteins. If the plateau is only for a defined range of q, then the protein is partially unfolded, while a Kratky plot that extends its plateau for all high values of s represents a completely unfolded protein (Kikhney et al. 2015).

All of these techniques represent quick information that can readily be extracted from a few quick transformations of an experimental scattering profile. Further information about the shape and organization of a protein requires more computationally advanced techniques, such as the DAMMIN technique, developed by D.I. Svergun (Svergun 1999). This technique uses a combination of Monte Carlo algorithms and the generation of theoretical SAXS curves to evaluate a series of models and find those that best match the experimental curve (Svergun 1999). The DAMMIN technique begins with a search volume of roughly the maximum particle size, and fills it with dummy atoms with a radius much smaller than this maximum search size (Franke et al. 2009). These dummy atoms are assigned to either solvent or object, forming the DAM or Dummy Atom Model [Figure 2] (Franke et al. 2009). This dummy atom model can be described as a configuration vector with length N, with N being proportional to $(R_g/r)^3$. The scattering intensities of the vector can be computed as:

$$I(q) = 2\pi^2 \sum_{l=0}^{\infty} \sum_{m= l}^{l} |A_{lm}(s)|^2 \quad (9)$$

Where A(s) is:

$$A_{lm}(s) = i\sqrt{2/\pi} v_a \sum^{M}{}_{\substack{j=l \\ X(j)=l}} \; j_l(sr_j) Y_{lm}^{*}(w_j) \quad (10)$$

Where r is the polar coordinates, v_a is the displaced volume per dummy atom, Y_{lm}^{*} are the spherical harmonics, and $j_l(sr_j)$ is the spherical Bessel function (Franke et al. 2009). Having a calculated a theoretical scattering profile, we can begin to make changes to bring it in line with an experimental profile. DAMMIN uses a simulated annealing algorithm to minimize the function f(X):

$$f(X) = R^2(I, X) + \sum_k \alpha_k P_k(X) \quad (11)$$

Where $R^2(I, X)$ is the discrepancy between the experimental and theoretical scattering curves, and $\sum_k \alpha_k P_k(X)$ is the sum of the various penalties designed to keep the DAM connected, compact, and close to the origin. The minimization is then done as follows (Franke et al. 2009):

1. Begin with a random DAM X_0 at high temperature T_0
2. Change one atom from either solvent to object, or vice versa, to obtain X' [Figure 13].
3. Compute $\Delta = f(X') - f(X_0)$
4. If Δ < 0, move to X', if not move to X' with a probability of $e^{-\Delta/kT}$. Move back to step 2 with either X' or X, depending on which was accepted.
5. Repeat, slowly reducing T until a certain number of total changes have occurred, or a certain number of successful changes have occurred.

Since there are likely multiple DAMs that closely match the experimental scattering curve, this process will likely result in multiple possible DAMs, which can be averaged to get a consensus shape.

2.7 SAXS Methods

The goal of using small angle X-ray scattering (SAXS) in our GluR0 project is to compare the predicted ensemble of conformations from our PMFs with experimental results obtained through SAXS. We begin by isolating a series of structures pulled from snapshots of our MD trajectories. These structures are stripped of waters, ions, etc. and have their ξ_1 and ξ_2 values measured. Those coordinates are saved as PDBs and then run through FOXS (Schneidman-Duhovny et al 2013, Schneidman-Duhovny et al 2016), a program that generates theoretical SAXS curve for a given profile. Because we know the ξ_1 and ξ_2 values for each of the structures used, and we know the energetics associated with those values, we can Boltzmann weight each of those SAXS curves to give an ensemble curve that should match experiment.

SAXS was performed on GluR0 S1S2 LBD obtained from the Mayer lab at the NIH, contained within a PETGq vector (Mayer et al. 2001). Protein was expressed in Rosetta BL21 E. coli. Cultures were grown overnight in 100 mL Luria-Bertani broth (LB) and then diluted 1:40 in 6 L of Terrific Broth (TB). These flasks were then shaken at 37 C to an absorbance of 0.8 and then induced by the addition of .25 mM IPTG. The cultures were then allowed to shake overnight at 16 C and spun down in a Sorvall RC-3B centrifuge with a GSA rotor at 5000 RPM. Cell pellets were then frozen and stored a -80 C. For purification, pellets were resuspended in a solution of 10 mM HEPES pH 7.4, 50 µg/ml DNaseI, and 1 mM PMSF. Resuspended cells were then run through a microfluidizer, and then spun down in a Sorvall RCSC centrifuge, in a SS-34 rotor. The lysate was spun down for 45 minutes at 4 C and a speed of 16000 RPM. The soluble fraction was then incubated with Roche cOmplete His-Tag resin. The slurry was then put into a benchtop gravity column, and washed with 8 column volumes of 10 mM HEPES pH 7.4, 150 mM NaCl. After washing the column was then eluted with 10 mM HEPES pH 7.4, 150 mM NaCl, and 500 mM Imidazole [Figure 14]. Eluted sample was then dialyzed overnight at 4 C in a 10 kDA Molecular Weight Cutoff (MWCO) Snakeskin dialysis tubing against a trypsinolysis buffer of 10 mM HEPES pH 7.4, 200 mM NaCl, 1mM EDTA, 1mM $CaCl_2$. Trypsin lysis was then performed at room temperature for 45 minutes, using a ratio of 1:100 for trypsin to GluR0. Lysis was stopped by the addition of 20mM EDTA and 2mM PMSF. Sample was then dialyzed in 25 kDA MWCO snakeskin overnight against 10 mM HEPES ph 7.4 25mM NaCl, and 1mM EDTA. Further purification was achieved by then running sample over Q-Sepharose anion exchange column [Figure 15]. Sample was then finally dialyzed into 10 mM HEPES ph 7.4, 150 mM NaCl. All purification was done in the presence of 1 mM glutamate or serine. Apo protein was obtained by adding 5% w/v glycerol to all buffers and repeatedly dialyzing away ligand. SAXS experiments were performed both at the home Hopkins source, a Rigaku BioSAXS-2000, and at the SIBLYS beamline in Berkeley.

2.8 SAXS Results

Our goals in using SAXS are to compare the theoretical SAXS curves generated from our PMFs with those observed experimentally. Our first task is to observe if the open and closed states are distinguishable through SAXS. Our results are shown in figure 16. We can clearly distinguish both states, and see that our Boltzmann weighted sample falls somewhere between them.

Next we move on to comparing our Boltzmann weighted curves with actual experimental results. Our initial results were generated through the SIBLYS mail-in SAXS service, with our protein flash frozen in liquid nitrogen, then packed in dry ice and shipped to Berkley. These results can be seen in 17. We can easily see that there is a gulf between our predicted curves and the actual ones. We checked for evidence of aggregation or unfolded protein in our results, which may have thrown off the SAXS curves. For aggregation we looked at the Guinier region for our samples, but found no evidence for the formation of aggregates [Figure 18]. We looked at Kratky plots for the GluR0 LBD, and found sharp, well folded proteins [Figure 19]. Searching for further sources of error, we added an extra filtration step to our protein prep, running the GluR0 through a size exclusion column to filter out any possible contaminants [Figure 20]. None of this managed to change our SAXS profiles or reveal any possible source of our error. We then began to think that it was the process of freezing and shipping our protein to SIBLYS that was throwing off our measurements. To correct for this, we used the Rigaku BioSAXS-2000, available at Hopkins, to analyze our GluR0 without needing to freeze it in liquid nitrogen. Results from the home source are shown [Figures 21 and 22]. Switching to the home source did not improve the agreement between our curves, so we began to look for other ways to explain the discrepancy. We noticed that our experimental radius of gyration calculations where much bigger for our experiment than for our theoretical curves, ~18 Å for the FOXS curves versus ~27 Å for our experiment. We found that by adding hydration layers and increasing the excluded volume we were able to bring the results closer together. GluR0 has a dimerization dissociation constant of 0.8 μM, much stronger than the millimolar dissociation constant associated with the

AMPA receptor (Chen et al. 1999, Ptak et al. 2014). Wondering if the presence of dimer in solution could have thrown off our SAXS curves, we generated a dummy atom model (DAM) using the curves from our home source. We used the DAMMIF algorithm, generating 13 different models, the average of which is shown in figure 23. The resulting model is quite spacious, and much more easily accommodates the dimer GluR0 structure, rather than the monomer. We believe that it is this dimer presence in our experiments that prevents our theoretical and experimental curves from matching up.

Figure 1

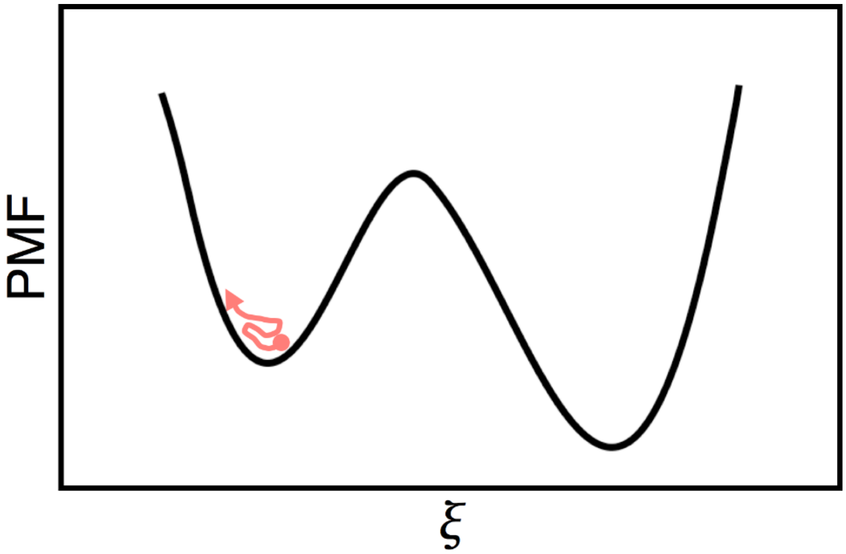

Fig. 1. **Depiction of Energy Landscape**

In unbiased molecular simulations, one or more large free energy barriers along an order parameter, ξ can impede conformational sampling (depicted in red).

Figure 2

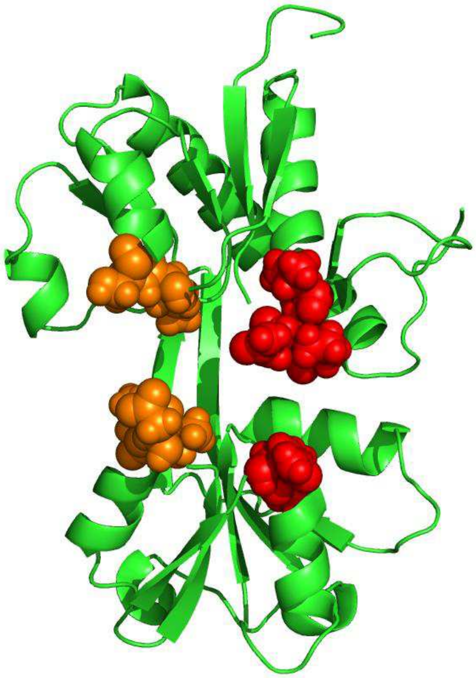

Fig 2. **GluR0 LBD with Umbrella Sampling Restraints**

GluR0 LBD, with highlighted residues showing ξ_1 and ξ_2. ξ_1 includes the 54th and 55th residues and the 124th, 125th, and 126th and is shown in orange. ξ_2 includes the 13th, 14th and 17th residues and the 143rd and 144th residues and is depicted in red. ξ_1 and ξ_2 and are at 13 Å and 14 Å respectively.

Figure 3

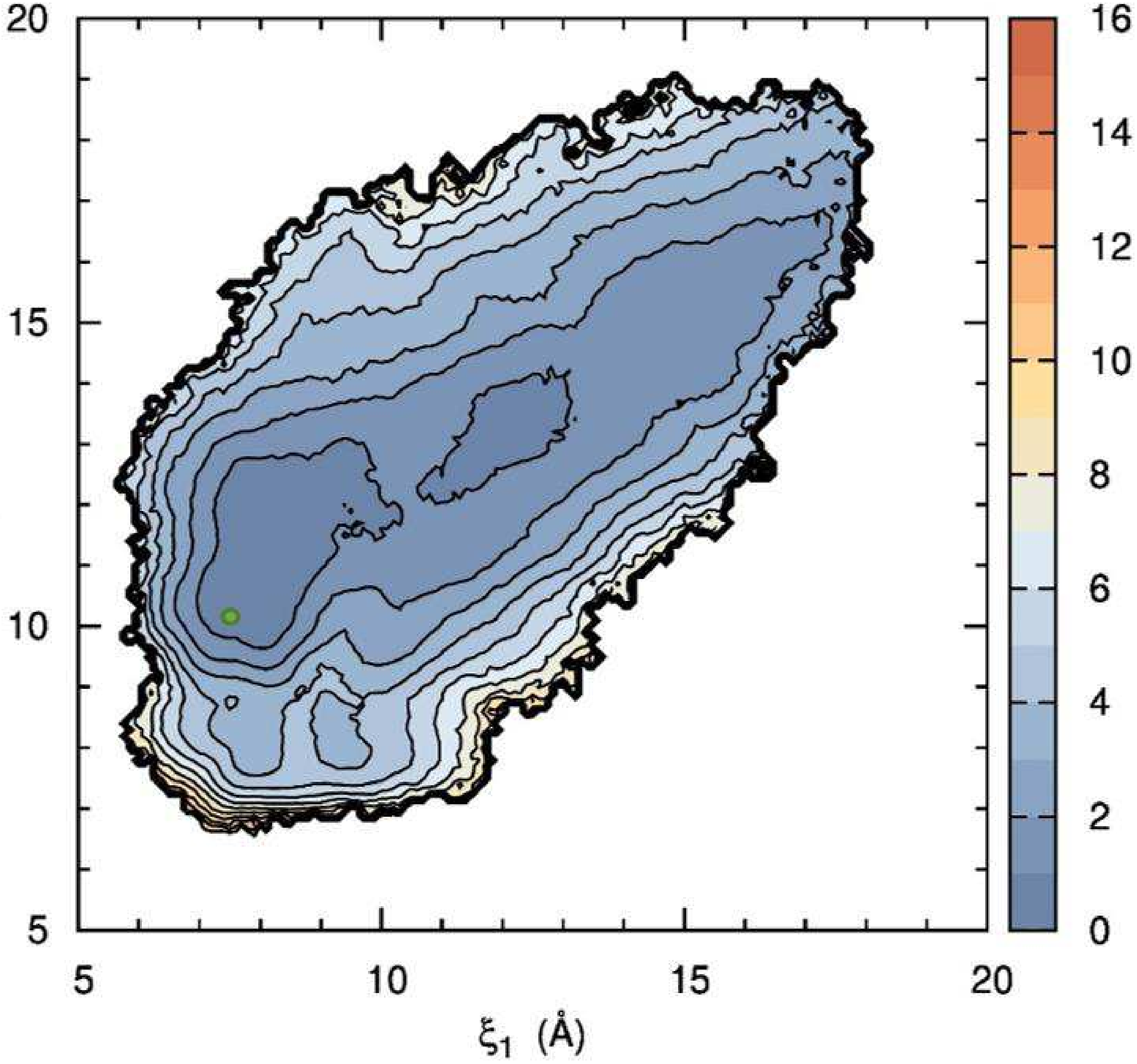

Fig 3. **GluR0 apo PMF**

PMF for the apo state of the GluR0 ligand binding domain. Contour lines correspond to a difference of 1 kcal/mol, with cooler colors being lower in free energy (see color bar). Crystal structure ξ_1 and ξ_2, at 7.7 Å and 10.1 Å, shown as green dot. Crystal structure taken from PDBid 1IIW (Mayer et al. 2001).

Figure 4

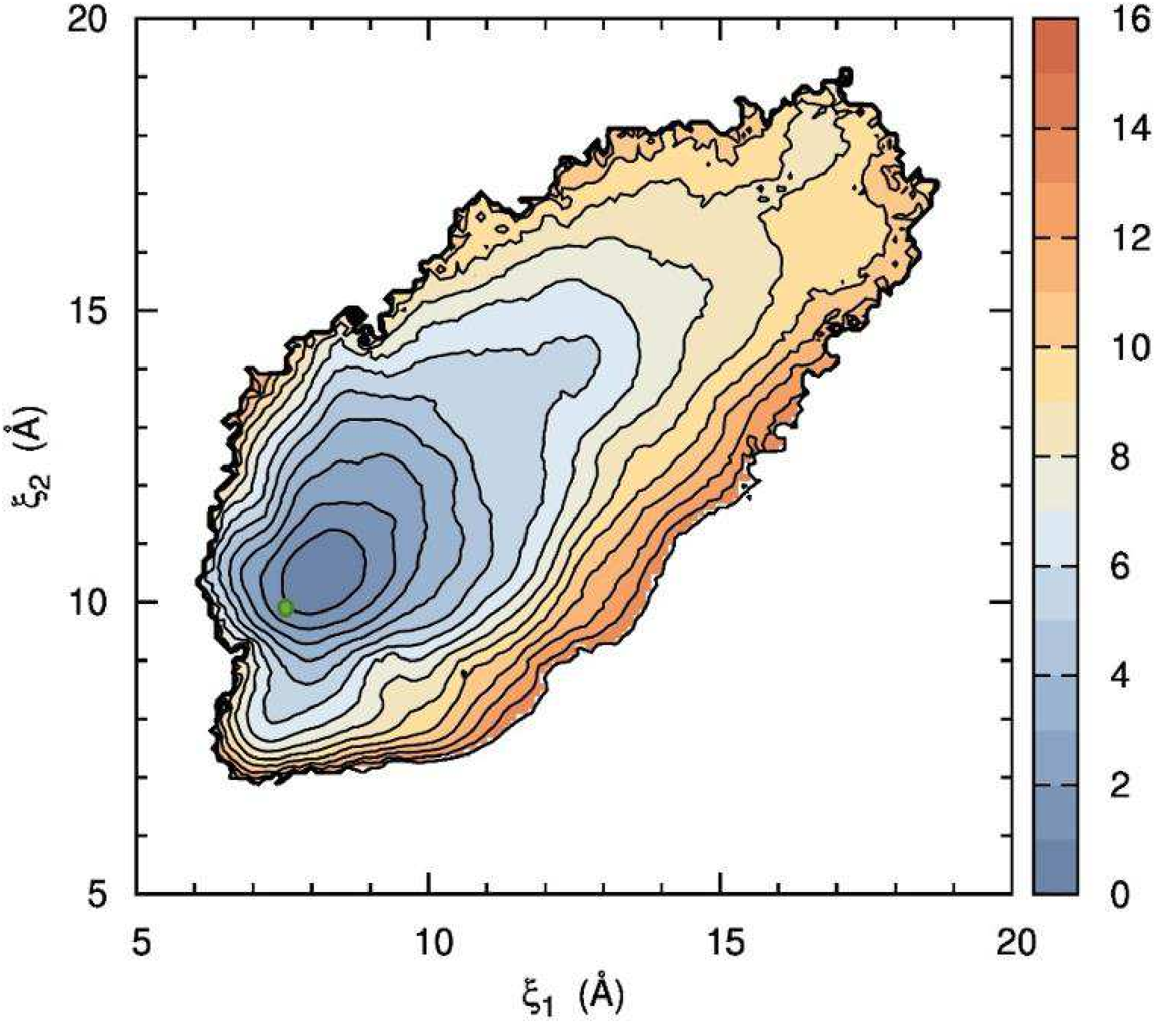

Fig 4. **GluR0 Glutamate Bound PMF**

PMF for the glutamate bound state of the GluR0 ligand binding domain. Contour lines correspond to a difference of 1 kcal/mol, with cooler colors being lower in free energy (see color bar). Crystal structure ξ_1 and ξ_2, at 7.5 Å and 9.9 Å, shown as green dot. Crystal structure taken from PDBid 1II5 (Mayer et al. 2001).

Figure 5.

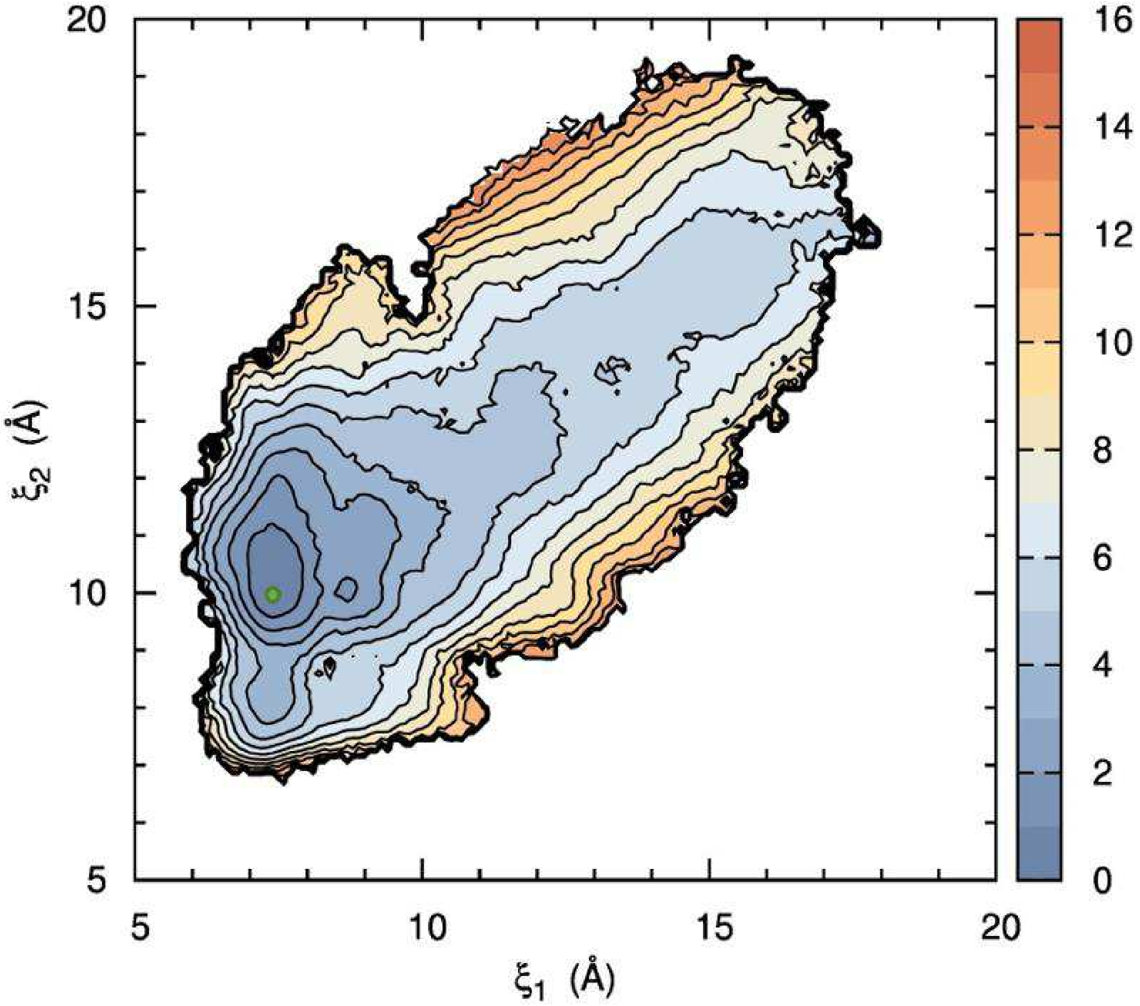

Fig 5. **GluR0 Serine Bound PMF**

PMF for the serine bound state of the GluR0 ligand binding domain. Contour lines correspond to a difference of 1 kcal/mol, with cooler colors being lower in free energy (see color bar). Crystal structure ξ_1 and ξ_2, at 7.6 Å and 9.9 Å, shown as green dot. Crystal structure taken from PDBid 1IIT (Mayer et al. 2001).

Figure 6.

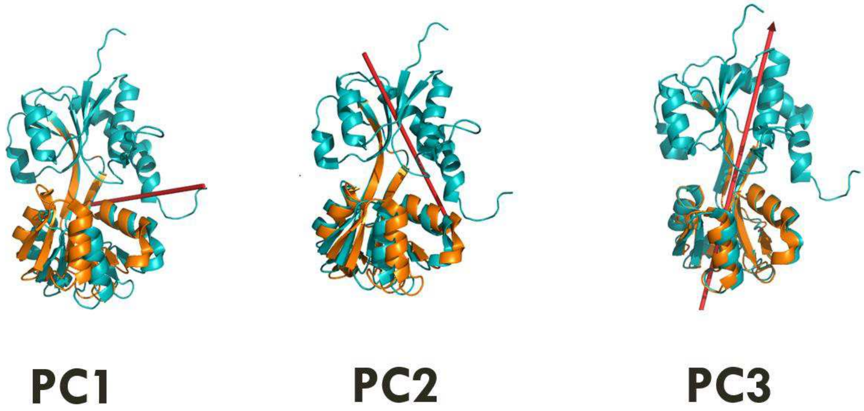

Fig. 6. **GluR0 Principal Components – Apo**

Depiction of principal components for the GluR0 LBD in the apo form. Blue and orange structures represent the maxima of the motion, with the red arrow showing the axis of rotation. The first principal component is a hinge-bending motion, PC2 is a rocking motion, and the final PC is a twist.

Figure 7.

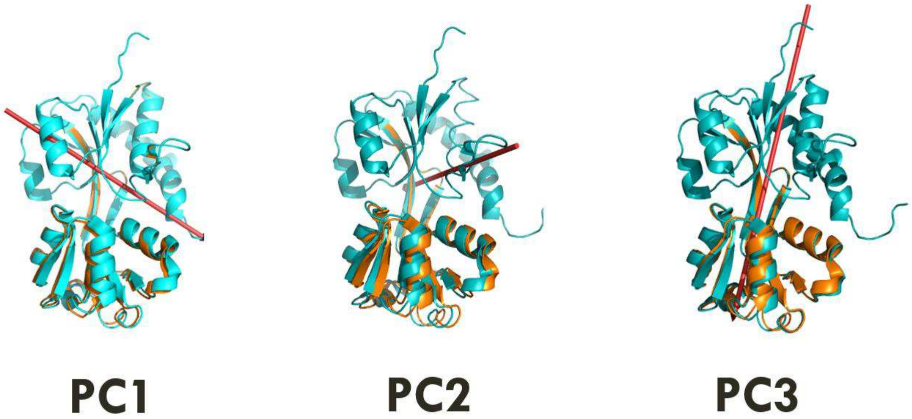

Fig. 7. **GluR0 Principal Components – Glu**

Depiction of principal components for the GluR0 LBD in the glutamate bound form. Blue and orange structures represent the maxima of the motion, with the red arrow showing the axis of rotation. The first principal component is a rocking motion, not the hinge-bending observed in the apo form. Hinge-bending is moved to the second PC, with twist remaining as the third.

Figure 8.

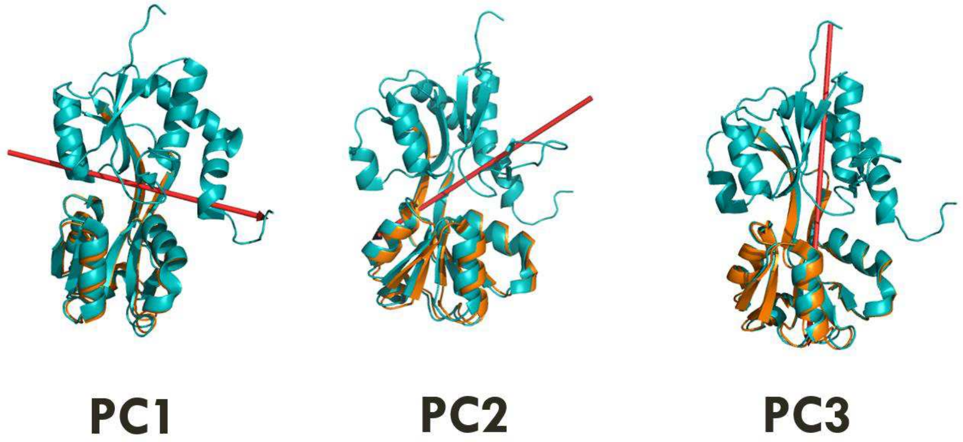

Fig 8. **GluR0 Principal Components – Ser**

Depiction of principal components for the GluR0 LBD in the serine bound form. Blue and orange structures represent the maxima of the motion, with the red arrow showing the axis of rotation. The first principal component is hinge-bending. Rock is the second, and twist the third.

Figure 9.

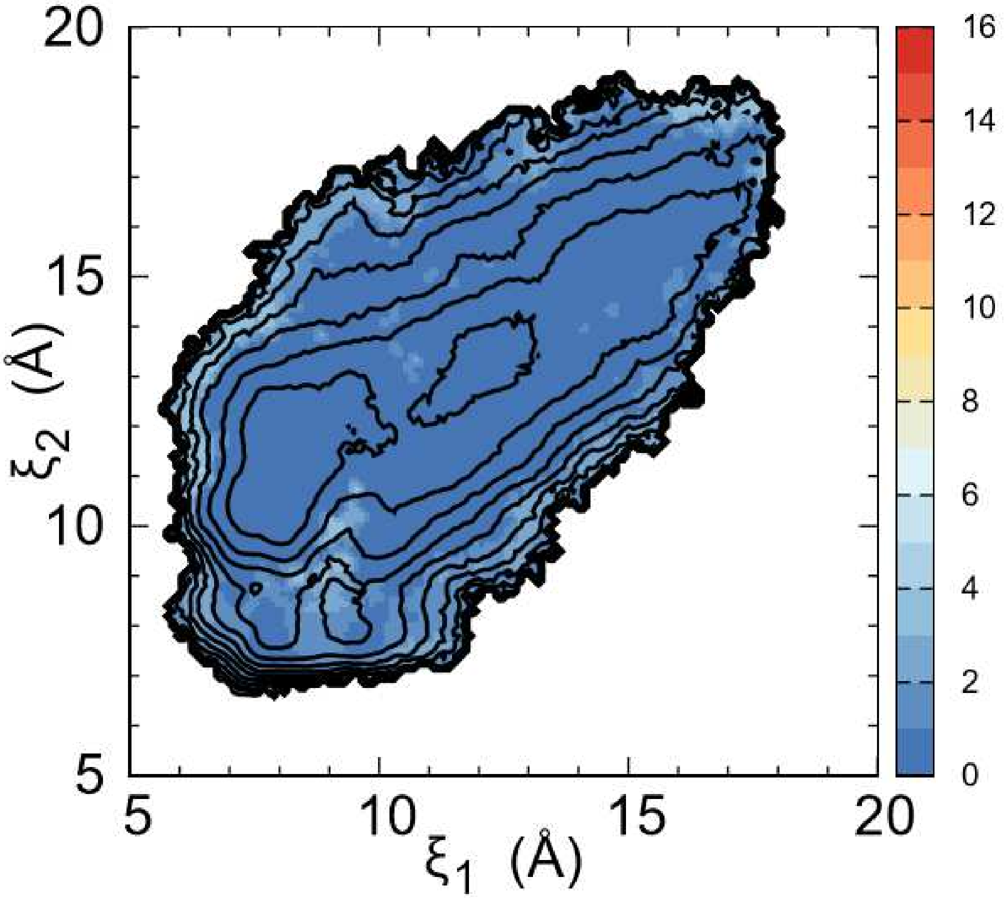

Fig. 9. **PMF Standard Deviation – GluR0 Apo**

Standard deviations are shown in kcal/mol (see the color bar), as determined by block averaging. The contour lines are taken from the 2D PMF in figure 3.

Figure 10.

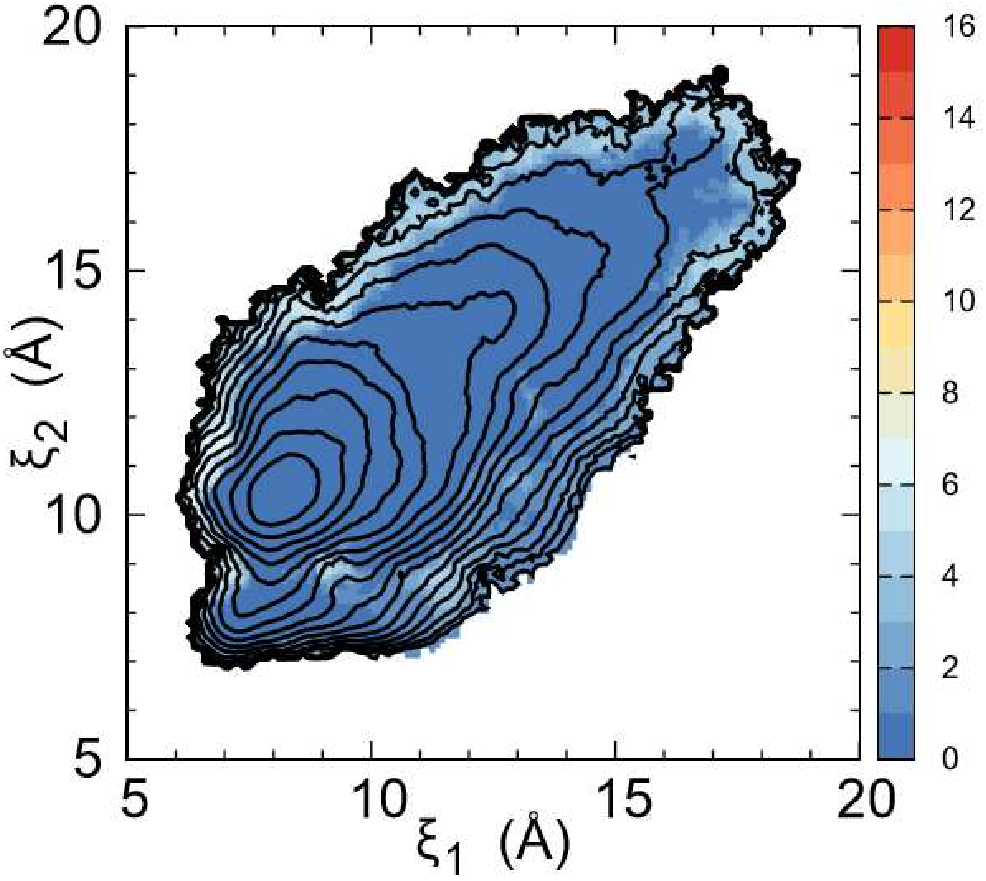

Fig. 10. **PMF Standard Deviation – GluR0 Glutamate Bound**

Standard deviations are shown in kcal/mol (see the color bar), as determined by block averaging. The contour lines are taken from the 2D PMF in figure 4.

Figure 11.

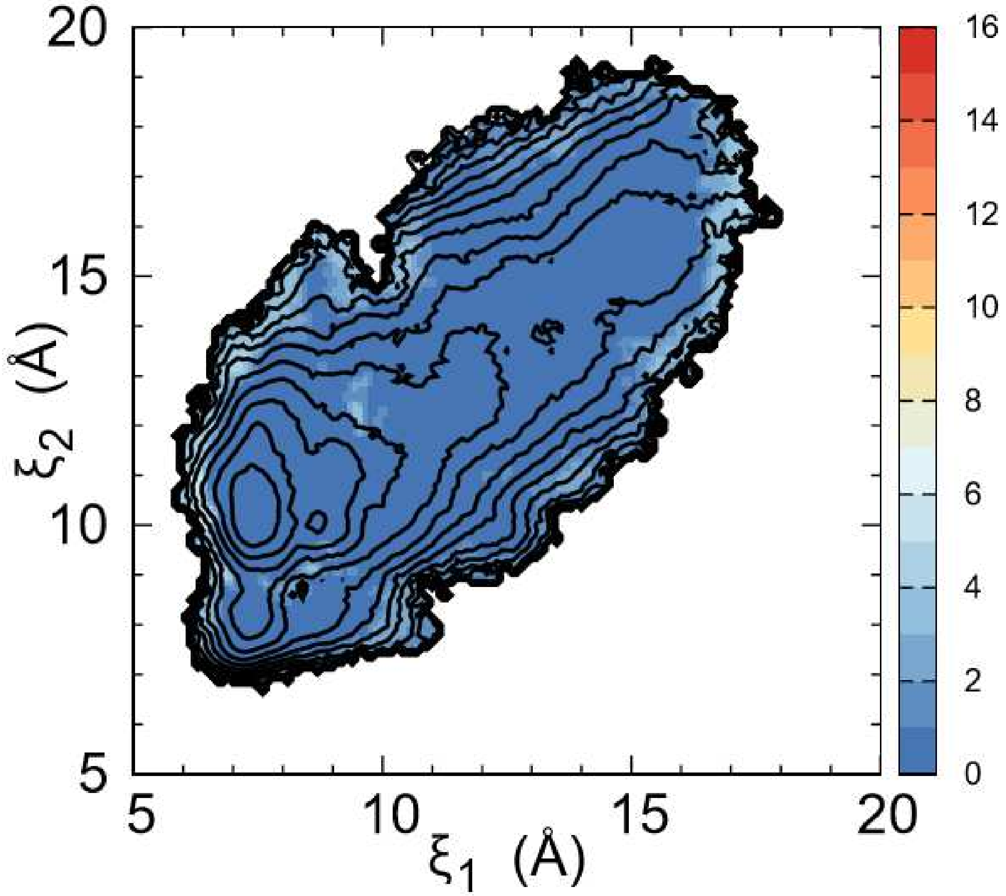

Fig. 11. **PMF Standard Deviation – GluR0 Serine Bound**

Standard deviations are shown in kcal/mol (see the color bar), as determined by block averaging. The contour lines are taken from the 2D PMF in figure 5.

Figure 12.

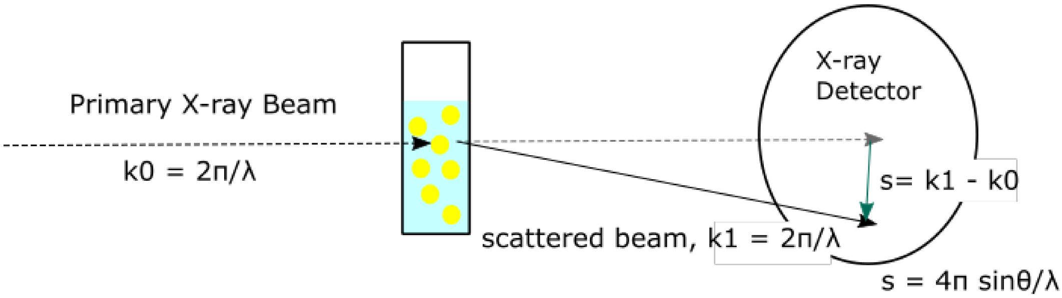

Fig. 12. **Depiction of an X-Ray being scattered by a particle.**

Incoming beam, k0, is scattered by particle in solution. Scattered beam is shown as k1, with the scattering vector s.

Figure 13

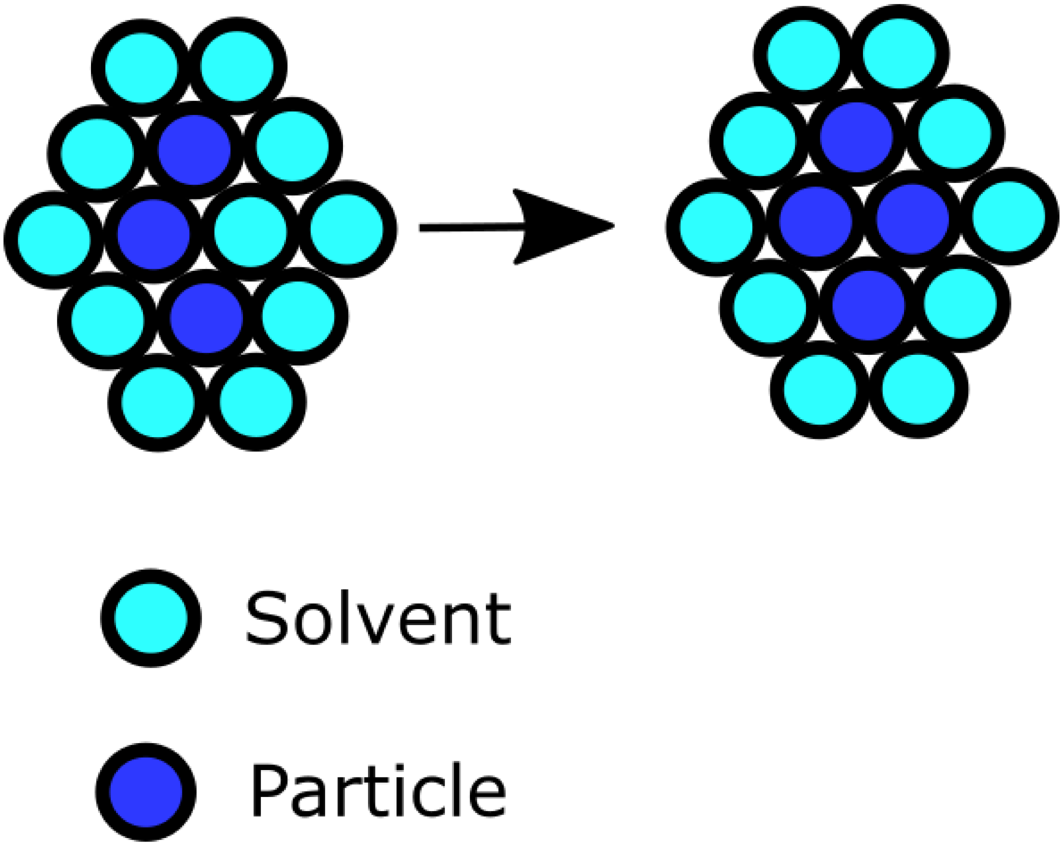

Fig. 13. **Dummy Atom Model**

The DAMMIN and DAMMIF algorithms will flip dummy atoms from solvent to particle to better match experiment.

Figure 14

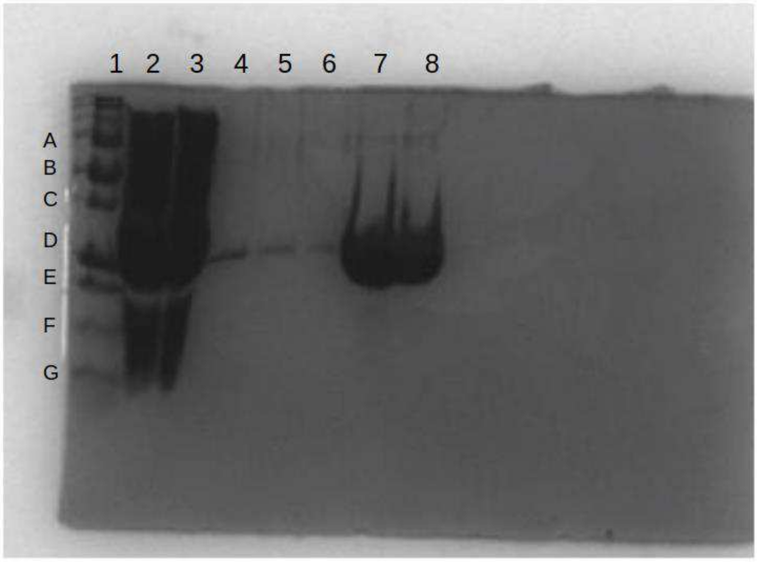

1 - Ladder
2 - Load
3 – Flowthrough
4 – Wash 1
5 – Wash 2
6 – Wash 3
7 – Elution
8 – o/n

A - 75 kD
B - 50 kD
C - 37 kD
D - 25 kD
E - 20 kD
F - 15 kD
G - 10 kD

Fig. 14. **His-tag purification of GluR0 LBD**

GluR0 was easily expressed in E. coli. 4 liters of TB would regularly yield 60 mgs of protein.

Figure 15

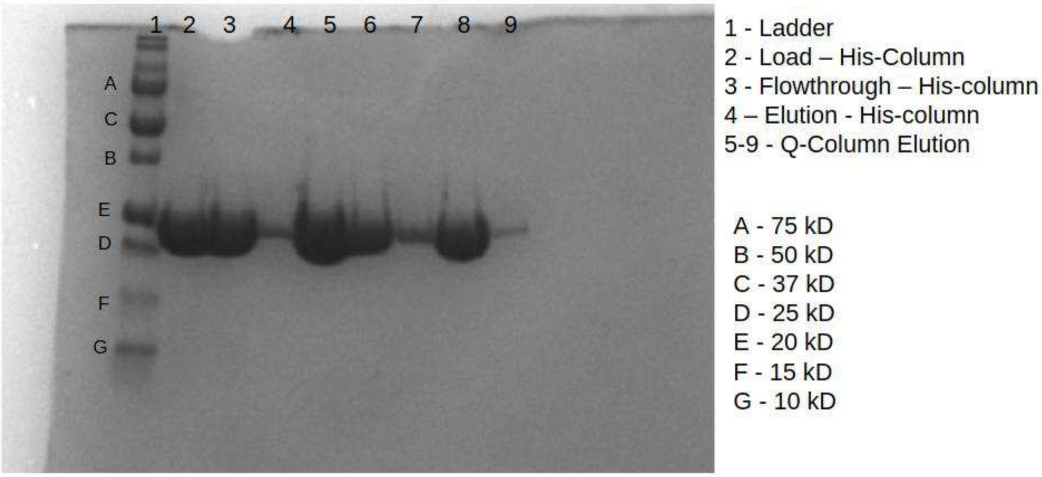

Fig. 15. **Q-Column purification of GluR0 LBD**

GluR0 LBD was clean and concentrated coming off of the Q-column.

Figure 16

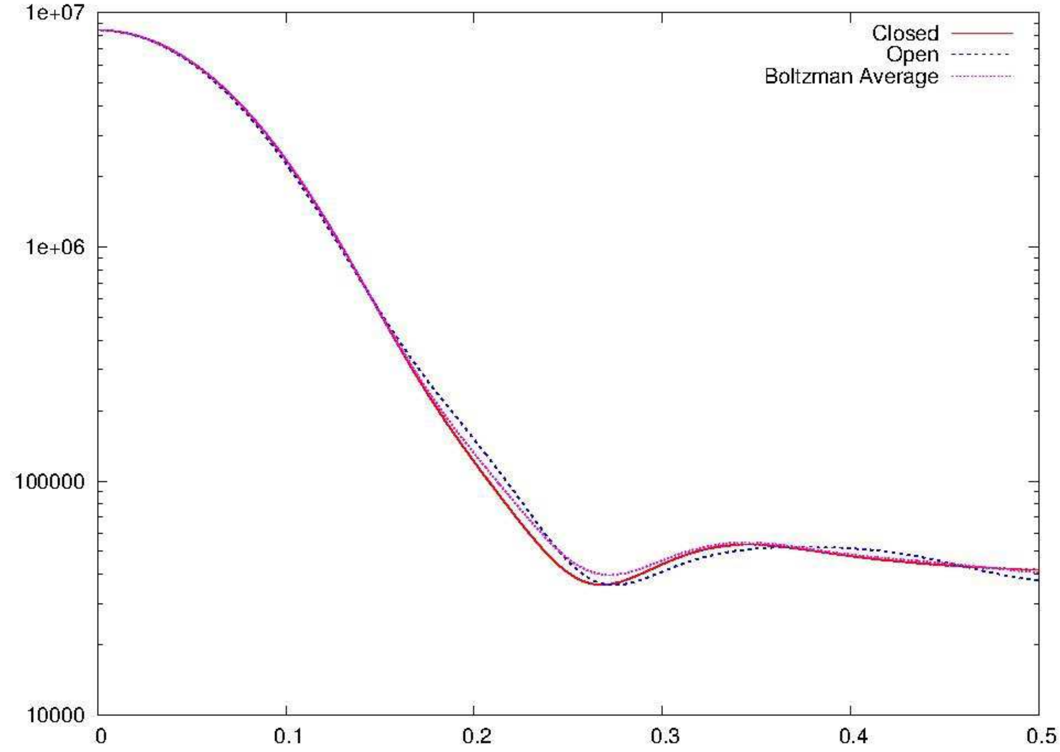

Fig. 16. **Open and Closed SAXS curves for GluR0**

FOXS generated curves for GluR0 in an open (ξ_1, ξ_2) = (13, 14 Å) and closed (ξ_1, ξ_2) = (7, 8 Å) state. In addition, the Boltzmann weighted average curve for GluR0 in the glutamate bound state is distinct from both.

Figure 17

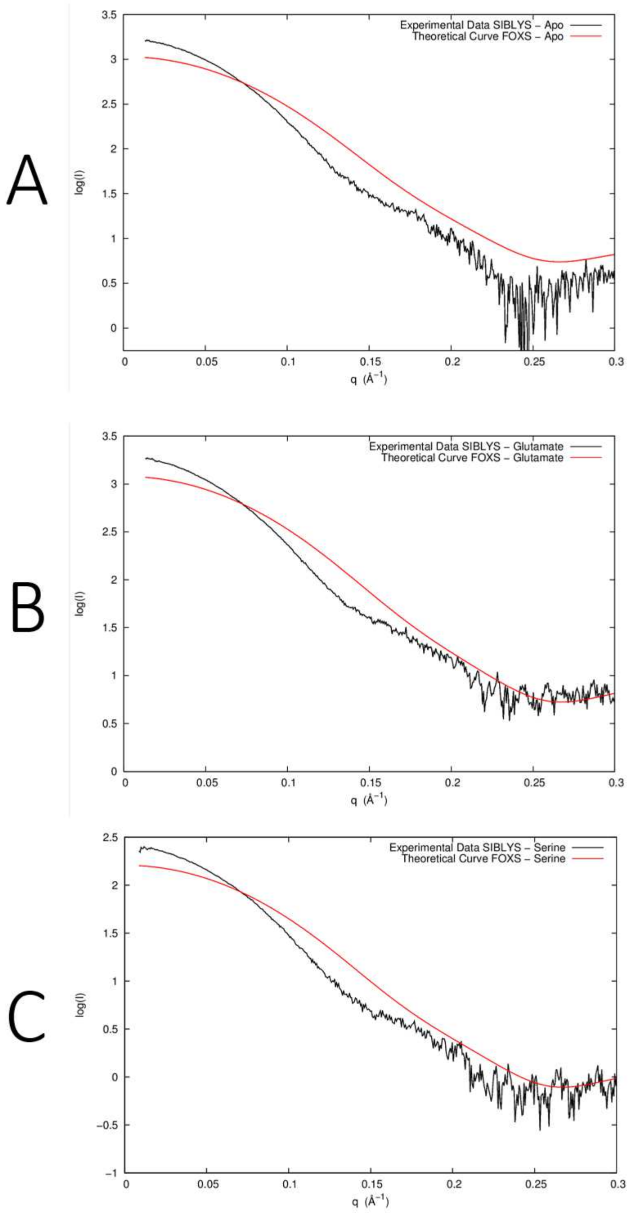

Fig. 17. **Theoretical and Experimental SAXS curves for GluR0**

SAXS curves taken at the SIBLYS beamline in Berkeley in black, with the corresponding theoretical FOXS curve in red. Apo, glutamate bound, and serine bound are in A, B, and C, respectively.

Figure 18

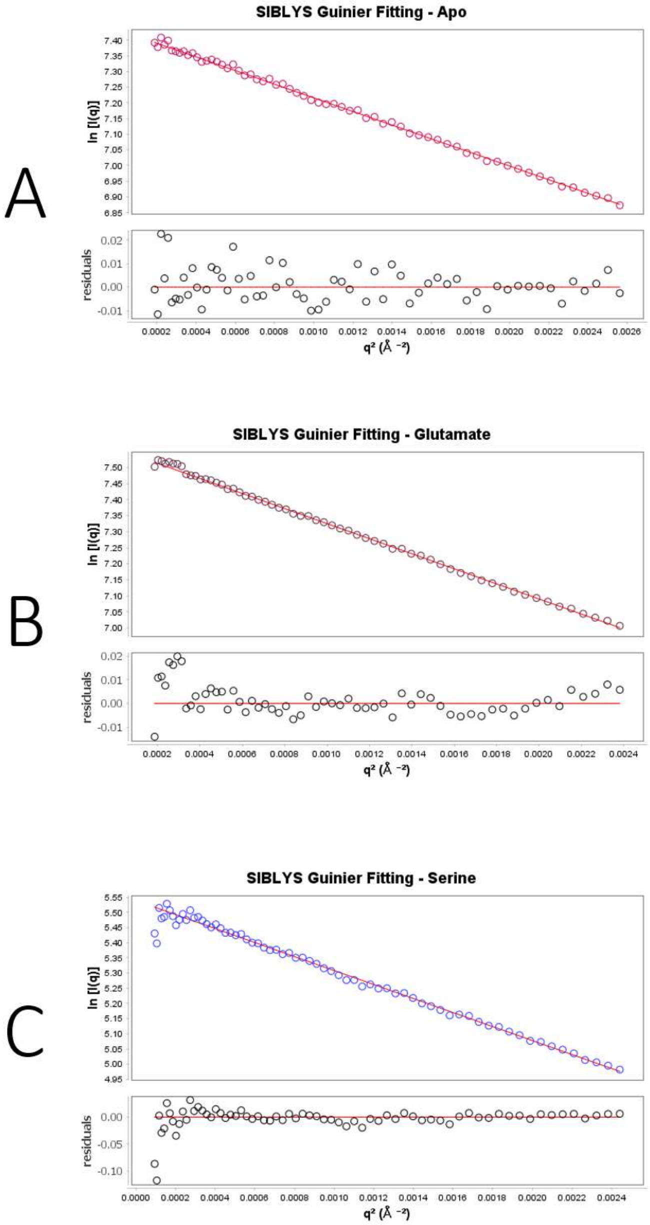

Fig. 18 **Guinier Plots For GluR0 from SIBLYS**

Guinier plots for GluR0 ligand binding domain from the SIBLYS beamline at Berkeley. All versions, both ligand bound and apo, seem free from aggregation, with long straight Guinier plots.

Figure 19

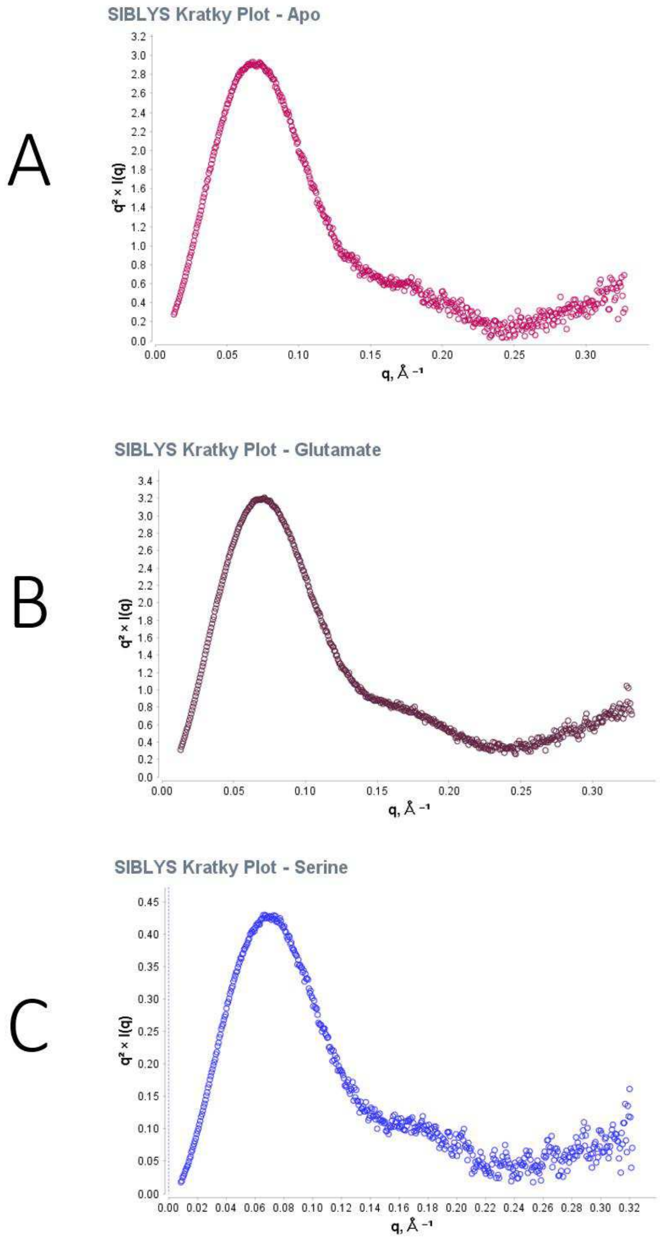

Fig. 19 **Kratky Plots For GluR0 from SIBLYS**

Kratky plots for GluR0 ligand binding domain from the SIBLYS beamline at Berkeley. All versions, both ligand bound and apo, are well folded, with clearly defined peaks.

Figure 20

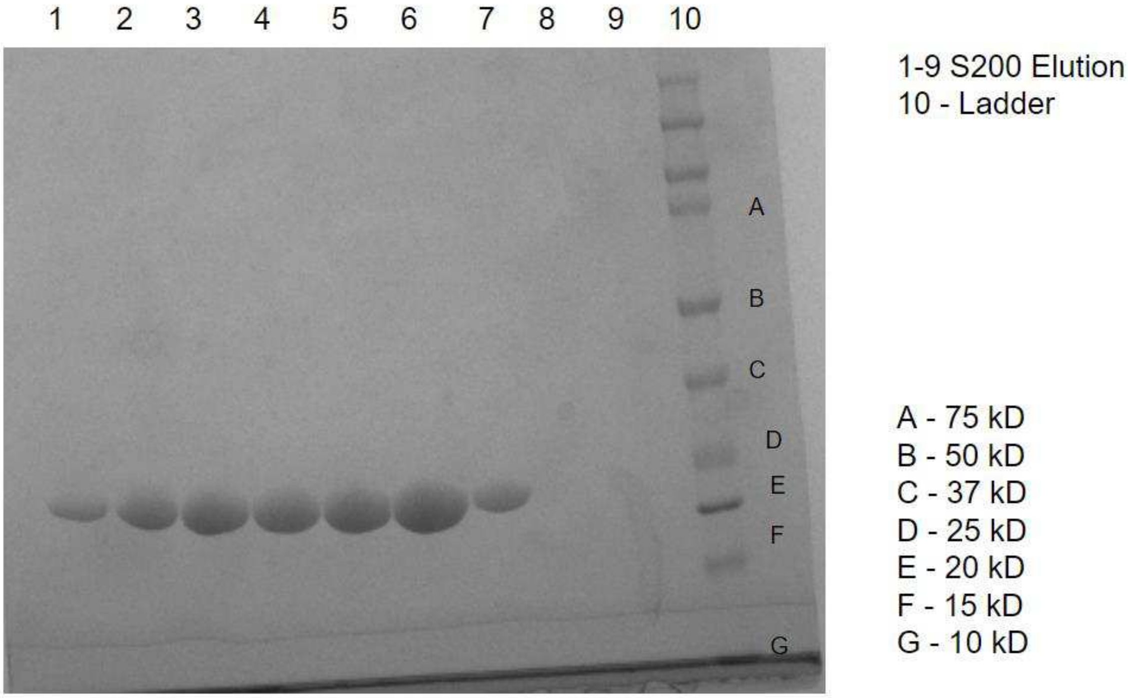

Fig. 20. **GluR0 LBD S200 Purification**

Gel of GluR0 run over an S200 column.

Figure 21

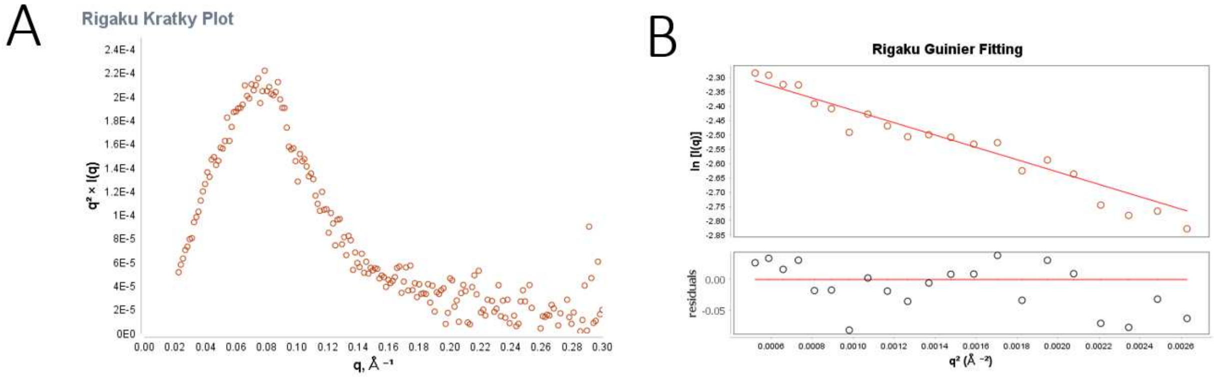

Fig. 21. **Kratky Plots For GluR0 from Rigaku**

Kratky and Guinier plots for serine bound GluR0 taken from the home source Rigaku. The Kratky plot shows one peak, indicative of a well folded protein, and the Guinier region is straight and free from aggregates.

Figure 22

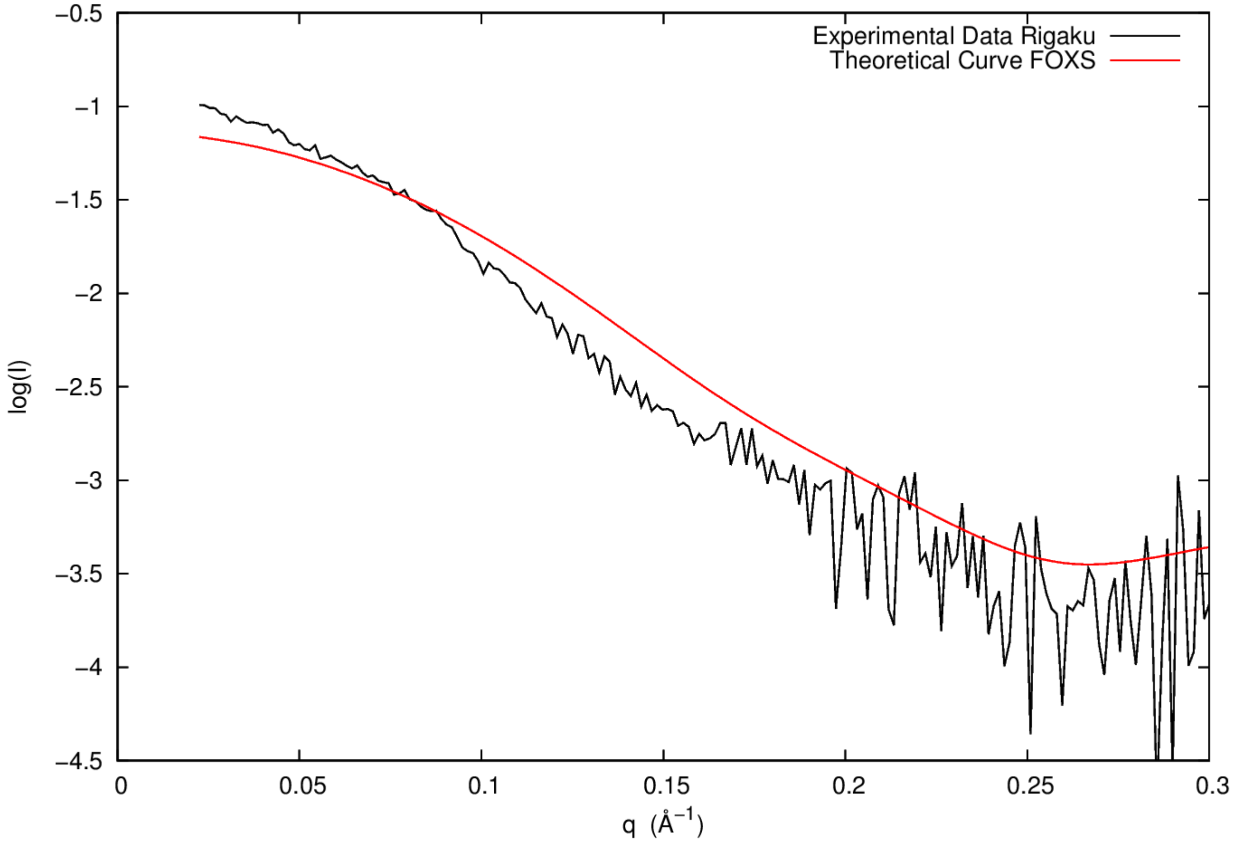

Fig 22. **Theoretical and Experimental SAXS curves for GluR0 – Rigaku**

SAXS curves taken of the serine bound GluR0 LBD at the Rigaku machine at Hopkins, with the corresponding theoretical FOXS curve in red

Figure 23

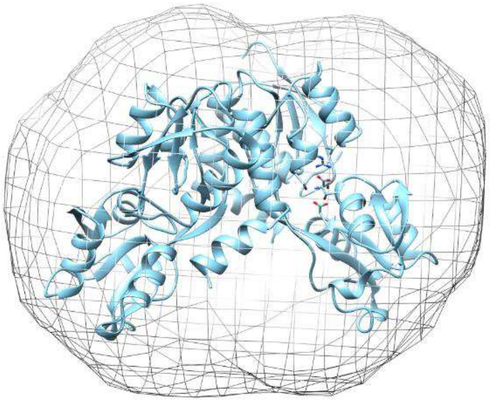

Fig. 23. **Image of SAXS envelope and GluR0 dimer**

Dummy Atom Model generated through the use of serine bound GluR0 scattering curves obtained off of the home source Rigaku. This is the model generated from averaging the 13 structures obtained through the use of the DAMMIF algorithm.

Table 1

	PC1	PC2	PC3
GluR0 - Apo	68.4 %	17.1 %	6.8 %
GluR0 – Glu	38.2 %	22.3 %	11.7 %
GluR0 - Serine	41.6 %	20.3 %	11.0 %

Table 1. **Contribution to variance by each principal component**

Chapter 3: Experimental Characterization of GluA2 Dimer Constructs

Desensitization is the process by which an active iGluR, one that has bound its corresponding agonist, closes its transmembrane domain. This closure occurs even though the agonist remains bound in the ligand binding domain [Figure 1].
Previous studies in the Lau lab have looked at the energetics of the AMPA receptor dimer [Figure 2]. In addition to this computational work, SAXS experiments were performed by Sara Bastos to verify that the ensemble measurements of the SAXS matched those predicted by the dimer PMFs (Unpublished Data). To further observe the behavior of the AMPA dimers and their various mutants, analytical ultracentrifugation (AUC) experiments were performed to look at the shape changes that accompany mutation.

3.1 Desensitization

Glutamate receptor activation occurs when a ligand binds into a ligand binding domain, inducing domain closure. This closure puts strain on the flexible linker regions surrounding the LBD, which is then relieved due to structural rearrangements in the transmembrane domain and the amino terminal domain (Chaudry et al. 2009, Weston et al. 2006). In the transmembrane domain, these rearrangements lead to pore opening, and thus depolarization. Desensitization occurs when the transmembrane domain closes, even though the ligand binding domain is still occupied by an agonist (Meyerson et al 2014). Both of these processes, activation and desensitization, occur on a millisecond long time scale (Weston et al. 2006). Desensitization allows the both the tuning of responses to high frequency synaptic activity, and prevents cell damage from occurring due to excitotoxicity (Weston et al 2006). This occurs through a rearrangement of the ligand binding domains that relieve stress on the linker regions while still maintaining a closed conformation (Meyerson et al. 2014, Weston et al. 2006). It is this rearrangement that is the central question of desensitization.

3.2 Analytical Ultracentrifugation Theory

Analytical Ultracentrifugation is a powerful method for studying the shape and stoichiometry of proteins and protein complexes. AUC works over a variety of concentration ranges, in a wide variety of solvent conditions, and works non-destructively to allow recovery of precious samples after an experiment is completed (Lebowitz et al. 2002). There are two complementary techniques within AUC: sedimentation velocity (SV) and sedimentation equilibrium (SE). SE provides thermodynamic information about properties such as stoichiometry and association constants. SV, which will be the focus of this thesis, provides hydrodynamic information about particle properties such as shape and size (Howlett et al, 2006).

Both the SE and SV experiments start from similar places, with an AUC cell containing both sample and blank spun in a rotor at high speed, anywhere from 10000 to 60000 RPM (Cole et al, 1999). At various times in this experiment, on the order of seconds to minutes for SV and hours to days for SE, the concentration of protein along the column is taken using either interference or absorbance optics. It is this measurement that is the fundamental data point of AUC, with SV experiments concerned with the travel of protein down the column as the experiment progresses, and SE experiments concerned with the equilibrium position of the distribution.

There are two important equations for AUC: the Svedberg equation and the Lamm equation.

The Svedberg equation is:

$$\frac{RTs}{D(1-vp)} = M \qquad (1)$$

Where R is the gas constant, T is the temperature, s is the sedimentation coeffecient, D is the diffusion constant, v is the volume of displaced fluid, p is the density of the solvent, and M is the mass of particle. The above equation allows us to derive unknown qualities of the particle under experiment, such as the diffusion or frictional coefficients, from known quantities such as mass, and the experimental observation s.

Having shown the utility of the experimental quantity s, we must then answer how does one measure that quantity from a SV experiment? While there are a number of methods for deriving this, both historical and contemporary, all start with the Lamm equation (Schuck et al. 2003):

$$\frac{\partial c}{\partial t} = \frac{1}{r}\frac{\partial}{\partial r}\left[rD\frac{\partial c}{\partial r} - \chi \mathrm{s}\mathrm{r}^2\omega^2\right] \qquad (2)$$

With the $rD\frac{\partial c}{\partial r}$ representing flux from diffusion, $\chi \mathrm{s}\mathrm{r}^2\omega^2$ term representing flux due to sedimentation, and χ representing the local concentration of the particle of interest. Solving this equation for s is complicated, and for the purposes of this thesis, we will turn to the c(s) method. This is implemented in the program SEDFIT, developed by Peter Schuck at the NIH. This is a numerical solution to the Lamm equation, shown by:

$$c(r,t) = \int c(s)L(s,r,t,D)ds \; (3)$$

With $c(r,t)$ representing experimental data, $c(s)$ representing the concentration of sedimentation coefficients between s and s+ds, and $L(s,r,t,D)$ representing the Lamm equation. The c(s) method works by generating several theoretical sedimentation profiles for various values of s, and then adjusts their concentration in the ensemble in order to minimize the difference between the experimental and theoretical data.

3.3 Methods

Sedimentation velocity experiments were performed on two different GluA2 dimer constructs, a Leucine-483 to tyrosine (L483Y) mutant known to promote stabilization of the dimer (Hansen et al, 2007), and a triple mutant of Leucine-483 to alanine, Leucine-748 to alanine, and Lysine-752 to alanine, (3M) designed to destabilize the dimer (Horning et al 2004). All constructs were designed with a seven amino acid extension of the C-Terminus: GGGASCS. This linker was designed to promote dimer formation in the constructs by allowing the cysteine to form a disulfide bond, linking two LBDs together.

All constructs were expressed in PET vectors and grown in Rosetta E. Coli. Cultures were grown overnight in 100mL Luria Broth (LB) and then diluted 1:40 in 6 L of Terrific Broth (TB). These flasks were then shaken at 37°C to an absorbance of 0.8 and then induced with .25 mM of IPTG. The cultures were then allowed to shake overnight at 16°C and spun down in a Sorvall RC-3B centrifuge with a GSA rotor. Cell pellets were then frozen and stored a -80°C.

For purification, pellets would be resuspended in a solution of 20 mM TRIS pH 8.0, 150 mM NaCl, 5mM Methionine, 1mM Glutamate, 5 mM $MgSO_4$, 1mM PMSF, and 25 µg/mL of DNAse1. Resuspended cells were then lysed with a microfluidizer, and then spun down in a Sorvall RCSC centrifuge, in a SS-34 rotor at 16000 RPM. The lysate was then spun down for 45 minutes at 4°C. The soluble fraction was then incubated with Roche cOmplete His-Tag resin [Figures 3 and 5]. The slurry was poured into a benchtop gravity column, and washed with 8 column volumes of 20 mM TRIS pH 8.0, 150 mM NaCl, 5mM Methionine, and 1mM Glutamate. After washing, the protein was then eluted with 20 mM TRIS pH 8.0, 150 mM NaCl, 5mM Methionine, 1mM Glutamate, and 500 mM Imidazole. Eluted sample was then dialyzed overnight at 4°C in a 10 kDA (Molecular Weight Cut Off) MWCO Snakeskin dialysis tubing against a trypsinolysis buffer of 20 mM TRIS pH 7.4, 200 mM NaCl, 1mM Glutamate, 5mM Methionine, 1mM EDTA, 1mM $CaCl_2$. Trypsin lysis was then performed at room temperature for 45 minutes, using a ratio of 1:100 for trypsin to GluA2. Lysis was stopped by the addition of 20mM EDTA and 2mM PMSF. Sample was then dialyzed in 25 kDA MWCO snakeskin overnight against 20 mM HEPES ph 7.0 20mM NaCl, 10 mM glutamate, 1mM EDTA. Sample was concentrated and run over a S200 gel filtration column [Figures 4 and 6]. Peak fractions were pooled and dialyzed in 25 kDA MWCO snakeskin overnight against 20 mM HEPES ph 7.0 140mM NaCl 10mM Glutamate 1mM EDTA.

Sedimentation velocity (SV) experiments were performed on a Beckman XL-I centrifuge at a speed of 42000 RPM, in an AN60Ti rotor. All runs were done at 4 C, and collected using absorbance optics at 280 nM with 0.001 cm radial steps.in a buffer of 20 mM HEPES ph 7.0 140mM NaCl 10mM Glutamate 1mM EDTA. All SV was done at a concentration of ~0.8 mg/mL. All runs were analyzed in SEDFIT (Schuck 2000) and plotted using GUSSI.

3.4 Results

The Lamm equation reads as:

$$\frac{\partial c}{\partial t} = \frac{1}{r}\frac{\partial}{\partial r}\left[rD\frac{\partial c}{\partial r} - \chi s r^2 \omega^2\right] \qquad (4)$$

One of the fitting parameters for the Lamm equation is D, the diffusion coefficient. D is itself dependent on f/f_0 as shown:

$$D\left(s, \frac{f}{f_0}\right) = \frac{\sqrt{2}}{18\pi}\frac{kT}{\sqrt{s}}\left(\eta\frac{f}{f_0}\right)^{-3/2}\sqrt{\frac{1-\mathrm{vp}}{\mathrm{v}}} \qquad (5)$$

f/f_0 is a representation of the proteins deviation from an ideal spherical shape (Smith et al 2008). The f/f_0 scale begins at 1, for an ideal sphere. Most globular proteins will have a value of 1.05 to 1.3, and as f/f_0 increases the shape becomes more and more oblong [Figure 7]. As we perform c(s) analysis on our AUC runs, we fit for both the sedimentation coefficient and for the ensemble average f/f_0 value. We expect that as we fit f/f_0 for both the L483Y and the 3M mutants of our GluA2 LBD, we will see a higher value for the 3M mutant than the L483Y, reflecting the destabilization of the dimer interface. Our plots for the c(s) fits is shown in figures 8-11. The table of values is shown in table 1.

We see sharp and distinct peaks for both of our mutants. This allows us to be fairly certain that the cysteine linkers are working, otherwise we would see a mixture of dimer and monomer peaks. Even in the absence of a cysteine linker, the L483Y mutant should show a significant dimer signal, given the nanomolar affinity the mutation gives to the ligand binding domain. There is some evidence for higher order oligomers, especially in the L483Y run. Further experiments are needed verify that we are measuring the dimer state of GluA2 in our AUC. Running the same experiment in the presence of reducing agent should confirm this. For the L483Y we should see similar results, while the triple mutant should show a lower sedimentation coefficient without the cysteine linkers to hold them together.

Overall, we see evidence that the 3M mutant is showing a higher f/f_0, reflecting an elongated shape relative the L438Y mutant, although each is within the error range of the other. More accurate f/f_0 values are only going to be accessible through performing global fits on both S and f/f_0. This will require performing more runs at a variety of speeds and concentrations. Even then, while we may be able to differentiate between both of the GluA2 mutants and the wild type dimer, the basic f/f_0 measurement may not be able to reveal the structural changes these dimers undergo. A more detailed view of the dimer interactions may require synthesizing results from multiple shape determining experiments, such as SAXS or multi angle light scattering (MALS) to complete the whole picture.

Figure 1:

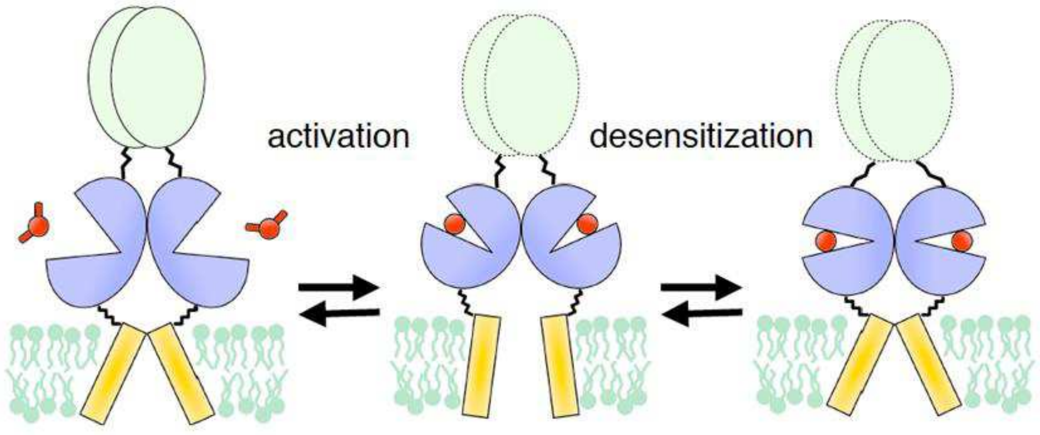

Fig 1. **Model of Desensitization** (Courtesy Albert Lau)

Activation and desensitization of glutamate receptors works as a three step process. Glutamate binds into apo ligand binding domain, inducing hinge closure. This closure then opens the transmembrane domain. Finally, the LBDs reorient themselves to allow both the LBD and TMD to remain closed.

Figure 2: GluA2 Dimer PMF

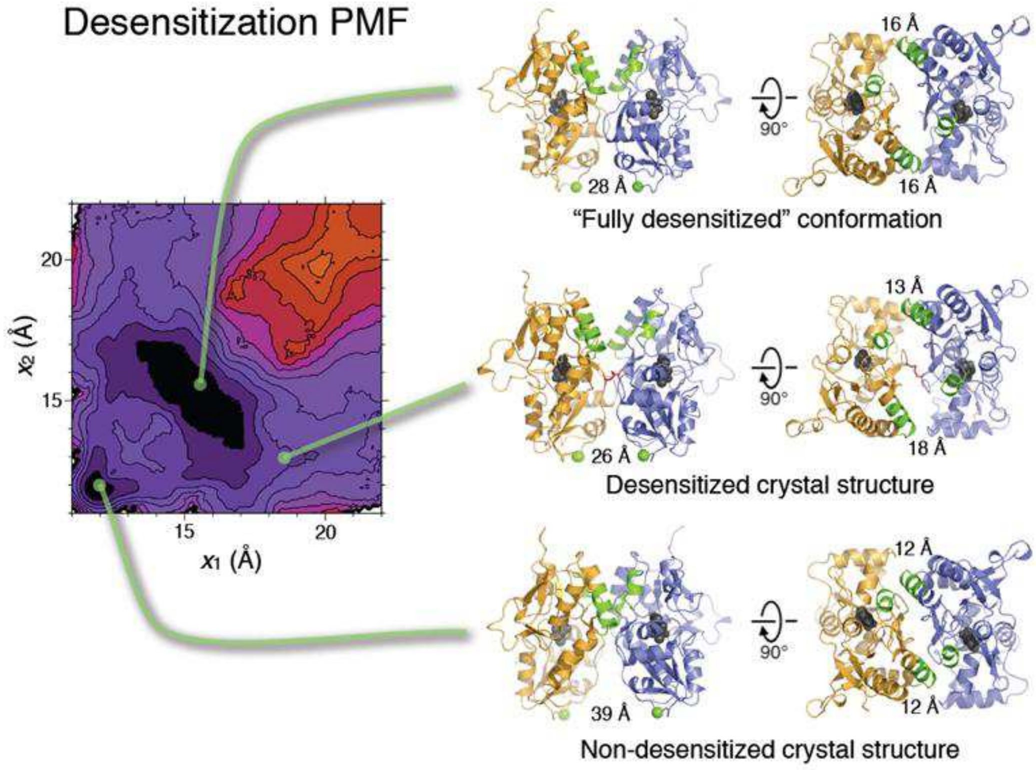

Fig 2. **GluA2 Dimer PMF**

Structural energetics associated with various LBD orientations. Individual ligand binding domains are colored wheat and blue, and residues known to be important in dimer formation are colored green.

Figure 3 GluA2 L483Y

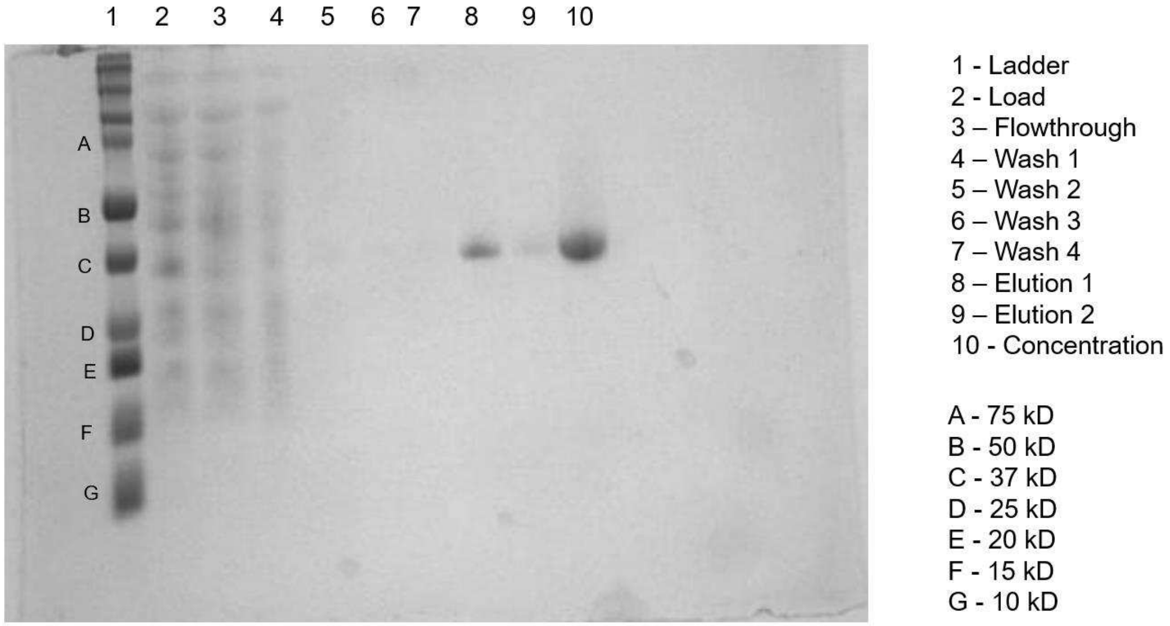

Fig 3. **GluA2 L483Y His-tag Purification**

GluA2 L483Y purified from Rosetta E. coli. Washes 1-4 took place in 20 mM TRIS pH 8.0, 150 mM NaCl, 5mM Methionine, and 1mM Glutamate. Elutions used 20 mM TRIS pH 8.0, 150 mM NaCl, 5mM Methionine, 1mM Glutamate, and 500 mM Imidazole. GluA2 L483Y came off clean and without any noticeable contamination. Lane 10 is the elution lanes from 8 and 9; pooled and concentrated.

Figure 4

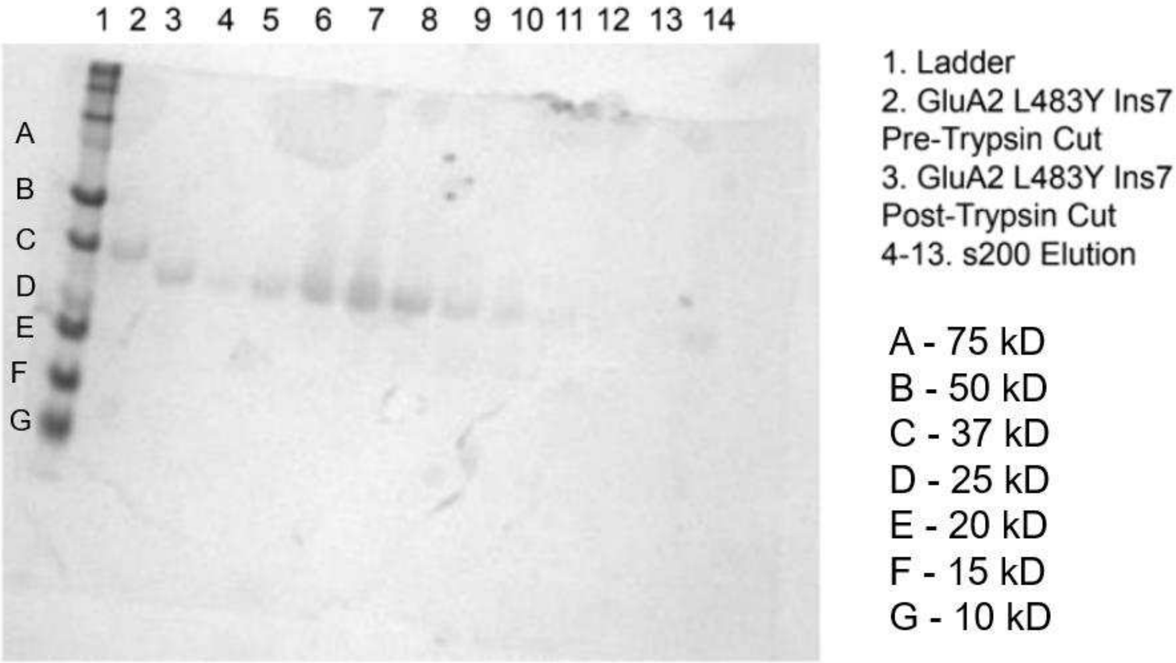

Fig 4. **GluA2 L483Y Size Exclusion Purification**

GluA2 L483Y was run through an S200 and eluted in 20 mM HEPES ph 7.0 20mM NaCl, 10 mM glutamate, 1mM EDTA. GluA2 L483Y came off clean and without any noticeable contamination.

Figure 5

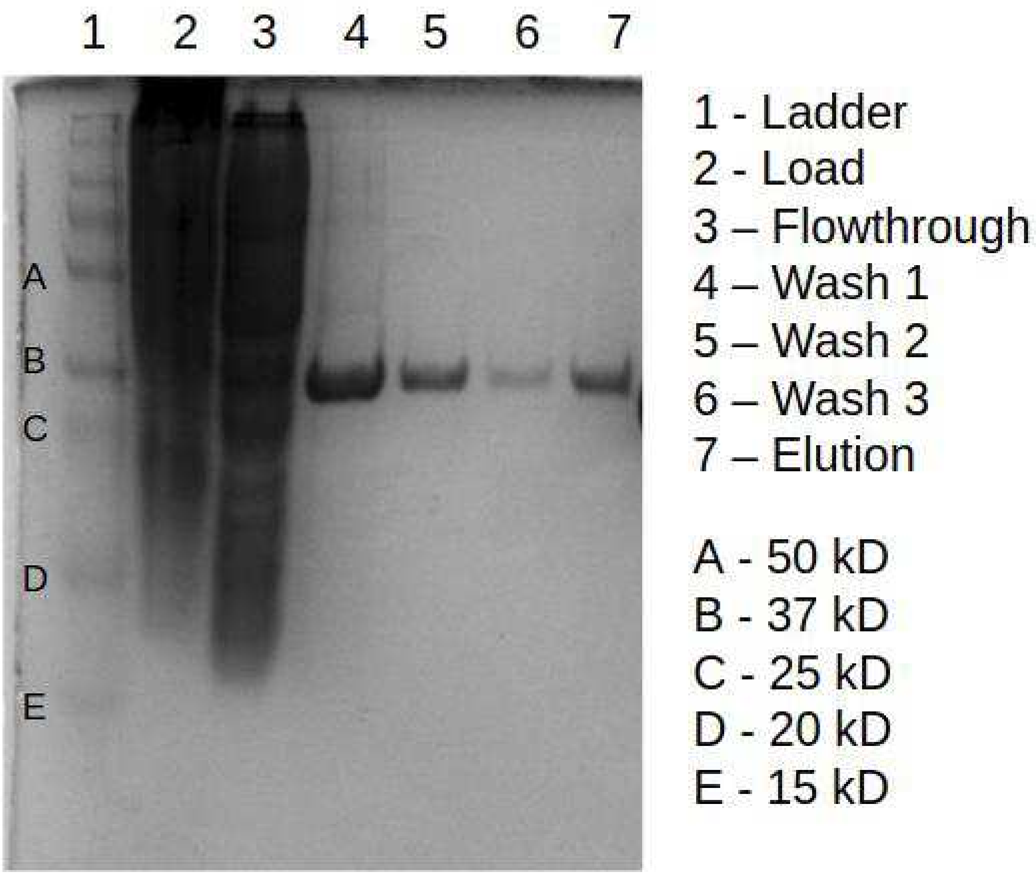

Fig 5. **GluA2 Triple Mutant His-Tag Purification**

GluA2 triple mutant purified from Rosetta E. coli. Washes 1-4 took place in 20 mM TRIS pH 8.0, 150 mM NaCl, 5mM Methionine, and 1mM Glutamate. Elutions used 20 mM TRIS pH 8.0, 150 mM NaCl, 5mM Methionine, 1mM Glutamate, and 500 mM Imidazole. GluA2 triple mutant came off clean and without any noticeable contamination.

Figure 6

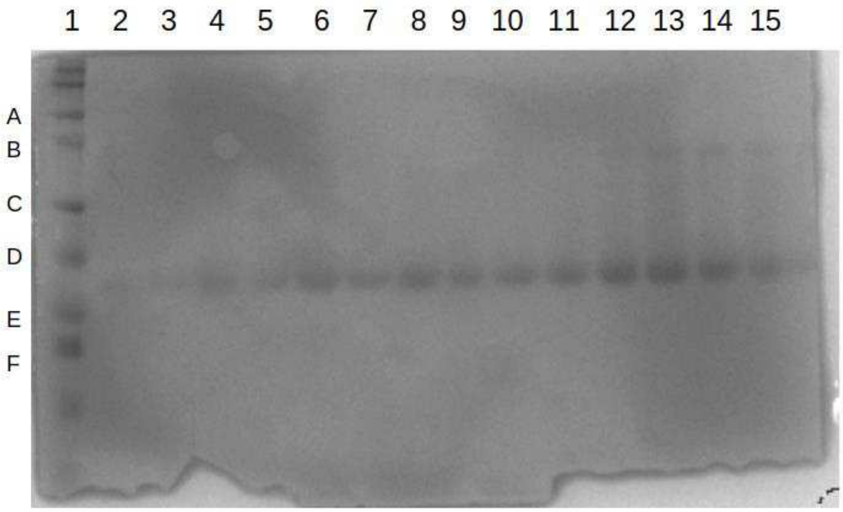

1 - Ladder
2-15 S200 Elution GluA2-3M Ins 7

A - 100 kD
B - 75 kD
C - 50 kD
D - 37 kD
E - 25 kD
F - 20 kD

Fig 6. **GluA2 Triple Mutant Size Exclusion Purification**

GluA2 triple mutant was run through an S200 and eluted in 20 mM HEPES ph 7.0 20mM NaCl, 10 mM glutamate, 1mM EDTA. GluA2 triple mutant showed some bands at ~75 kD in later elutions, which were not pooled with the other fractions.

Figure 7: f/f0 sizes and Associated Shape

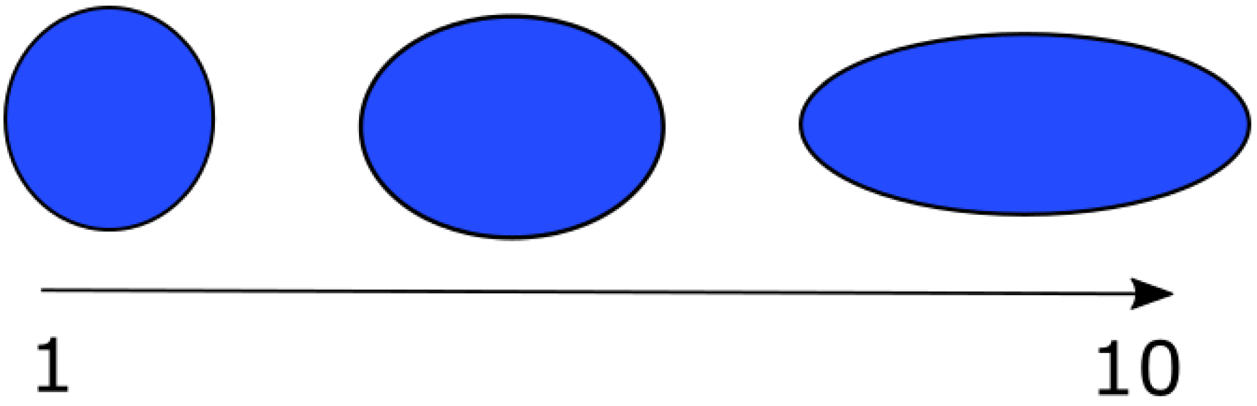

Fig 7. **Shapes associated with f/f_0 values**

The particle of interest adopts a more and more elongated shape as the ratio of f to f_0 grows higher.

Figure 8: GluA2 L483Y c(s)

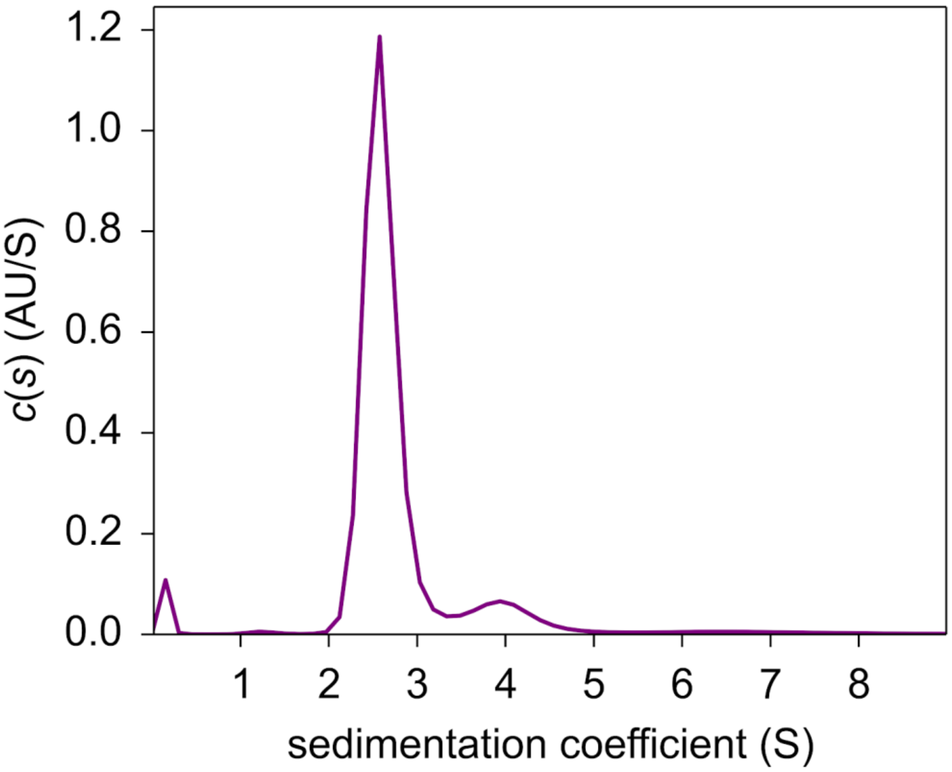

Fig 8. **c(s) graph for GluA2 L483Y mutant**

Main peak is at 2.7 S, with a smaller peak at 3.9 S. Main peak should be dimer, with the higher S contribution coming from higher order oligomers.

Figure 9: GluA2 L483Y c(s) fit and residuals

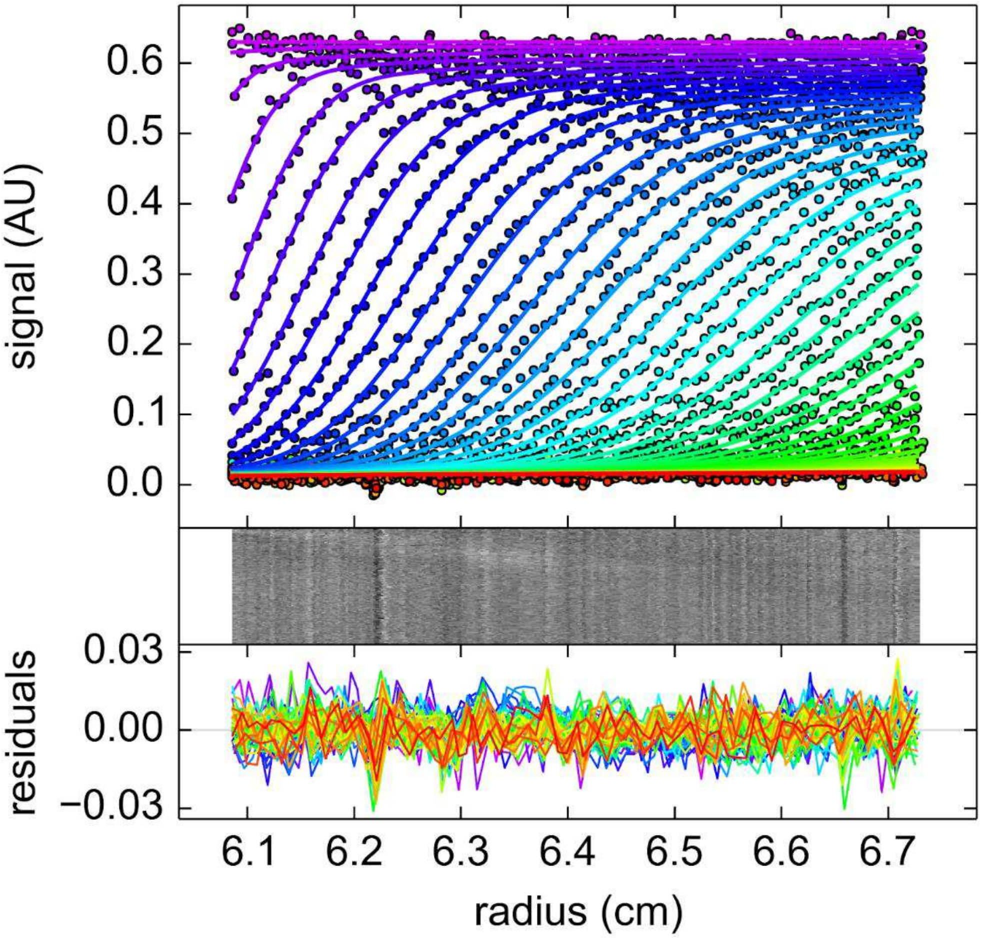

Fig 9. **Fit and residuals for L483Y mutant c(s) analysis**

Top graph shows fit between experimental and c(s) data, with each scan color coded.

Residuals are shown in the bottom two graphs.

Figure 10:

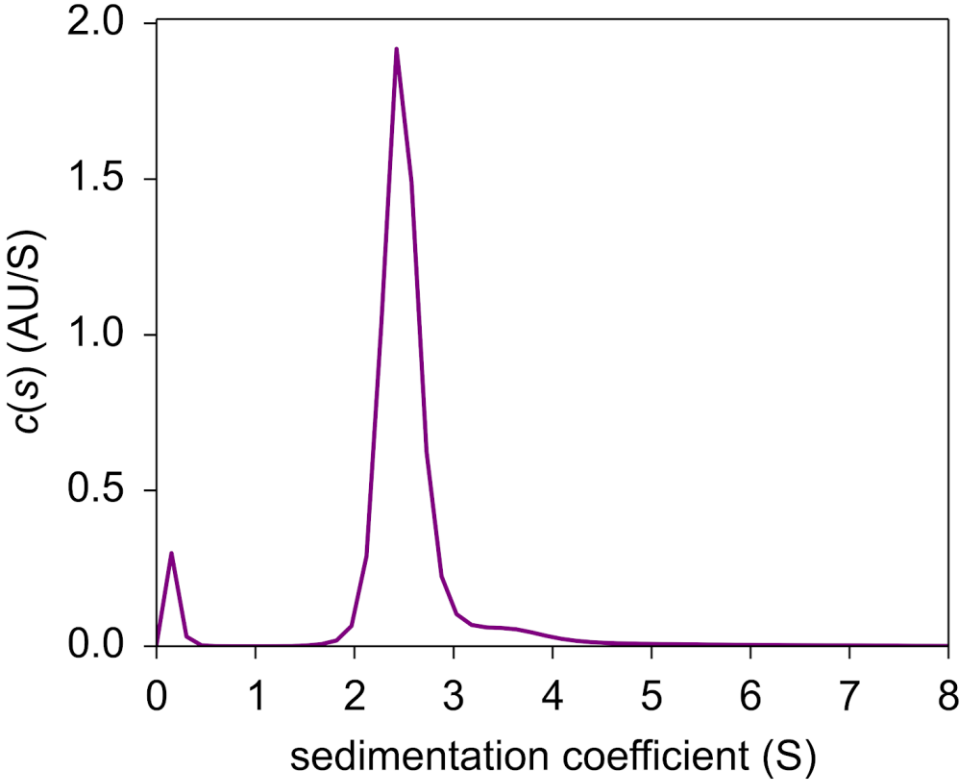

Fig 10. **c(s) graph for GluA2 Triple mutant**

Main peak is at 2.7 S. Some signal in the higher S region, but less so than in the L483Y mutant. The higher dimer affinity of the L483Y mutant may explain the sharp distinct peak in the higher S region lacking here.

Figure 11: GluA2 3M c(s) fit and residuals

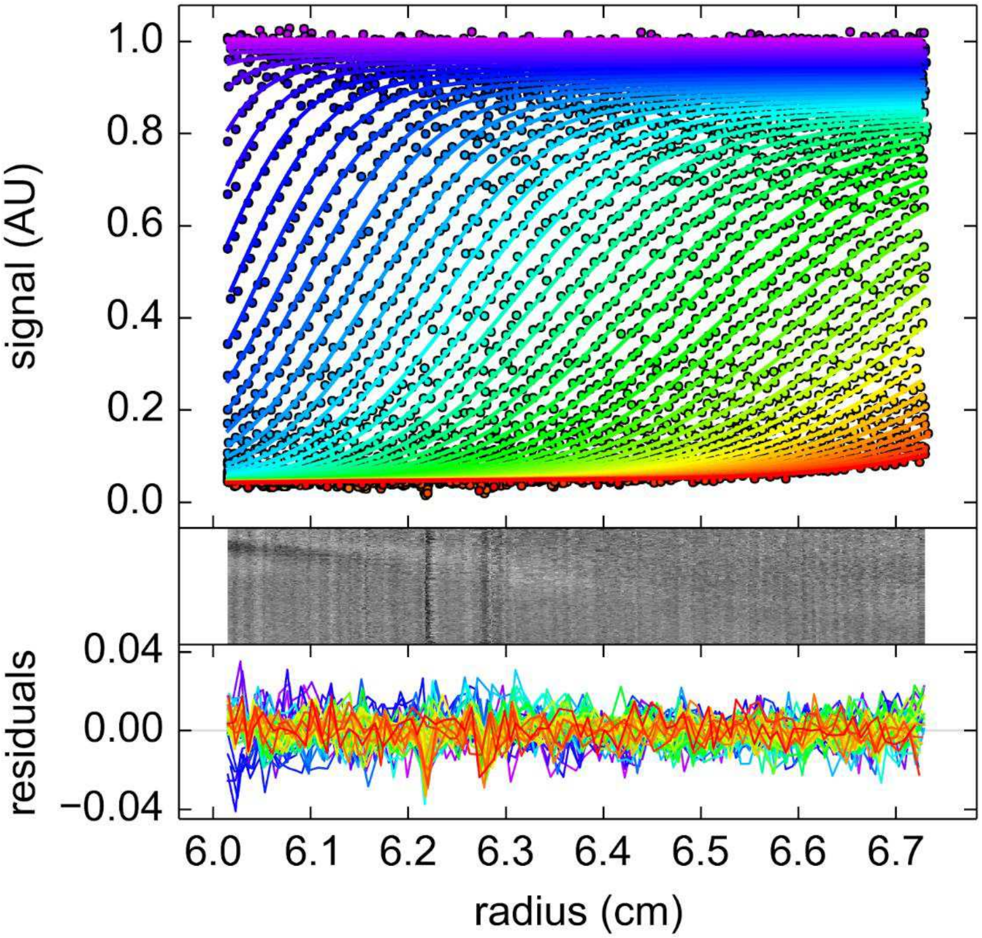

Fig 11. **Fit and residuals for Triple mutant c(s) analysis**

Top graph shows fit between experimental and c(s) data, with each scan color coded.

Residuals are shown in the bottom two graphs.

Table 1: f/f0 Values for GluA2 dimer constructs

L483Y	3M
2.24 ± .11	2.32 ± .10

Chapter 4: Principal Component Analysis of GluN Ligand Binding Domains

Reproduced in part from:

Conformational Analysis of NMDA Receptor GluN1, GluN2, and GluN3 Ligand-Binding Domains Reveals Subtype-Specific Characteristics, Structure vol.21 issue 10 8 October 2013
by

Yongneng Yao, John Belcher, Anthony J. Berger, Mark L. Mayer, and Albert Y. Lau

4.1 GluN Ligand Binding Domain Simulations

The NMDA receptor family of glutamate receptor ion channels is formed by obligate heteromeric assemblies of GluN1, GluN2, and GluN3 subunits. GluN1 and GluN3 bind glycine, whereas GluN2 binds glutamate. Dr. Albert Lau performed umbrella sampling simulations yielding the PMFs in Figures 1-3.

4.2 Bootstrapping of GluN Ligand Binding Domain Simulations

The range of variation in each PMF was estimated using a bootstrapping approach (Wehrens et al 2000). ξ_1 and ξ_2 for each GluN umbrella window was resampled using a window of 300 ps. On average, correlated fluctuations in ξ_1 and ξ_2 decay reasonably close to zero within these windows, as assessed from a calculation of the autocorrelation function (Box et al, 2008):

$$r_k = \frac{\sum_{i=1}^{N-k}(x_i - \bar{x})(x_{i+k} - \bar{x})}{\sum_{i=1}^{N}(x_i - \bar{x})^2} \quad (1)$$

Where N is the total number of time steps, k is the number of time steps corresponding to a given lag time, x is either ξ_1 or ξ_2, and the overbar indicates an average.
The error range for these plots are shown in figures 1-3.

4.3 Principal Component Analysis Methods

Hinge-bending motions are the dominant large-scale structural variations observed in crystallographic analyses of GluR LBDs when agonist complexes are compared with the apo state or antagonist complexes (Bjerrum and Biggin, 2008; Mayer, 2011; Pøhlsgaard et al., 2011; Stawski et al., 2010). These motions are highly correlated with the order parameter (ξ_1,ξ_2). Additional modes of interlobe motions orthogonal to (ξ_1,ξ_2), however, may also contribute to the conformational dynamics of receptor activation (Birdsey-Benson et al., 2010). Such secondary modes are difficult to distinguish from hinge bending using only (ξ_1,ξ_2) as an indicator. In principle, additional order parameters could be used to differentiate among the various conformational modes, but incorporating them into an umbrella sampling strategy would require substantially more computational time because sampling scales exponentially with the number of order parameters. We thus sought to characterize LBD motions using principal component analysis (PCA), which can determine the large-scale characteristic motions of a protein from an ensemble of protein configurations (García, 1992; Grossfield and Zuckerman, 2009; Levy et al., 1984).

PCA calculations involve the diagonalization of the covariance matrix Cij of positional deviations among an ensemble of protein structures (Grossfield and Zuckerman, 2009; Levy et al., 1984):

$$C_{ij} = cov(X_i, X_j) = E\left[(X_i - \mu_i)(X_j - \mu_j)\right] \text{ (2)}$$

Where X_i represents a specific Cα coordinate, E is an operator that denotes the mean of its argument, and μ_i is the average positional value for the i-th Cα. The eigenvectors, or principal components (PCs), represent the characteristic motions observed in the ensemble, and each eigenvalue is the mean square fluctuation associated with the corresponding eigenvector. The ensemble, generated separately for each iGluR LBD in either the apo- or glycine/glutamate-bound state, consists of protein conformers from all umbrella sampling windows in which W(ξ_1,ξ_2) is less than 2 kcal/mol. This subset includes the vast majority of conformations that are expected to be observed in a Boltzmann-weighted ensemble while excluding conformations that are energetically difficult to access. This is a cruder calculation than the one presented in chapter 2. Here every conformation is weighted equally, in contrast to the Boltzmann weighting shown earlier. PCs were also computed using cutoffs of 1 and 3 kcal/mol, and the results were similar. Only Cα coordinates were used in the calculations. All conformers were first superimposed onto lobe 1 of a reference structure using a selection of Cα atoms that excludes flexible loops. The references for GluN1, GluN2A and GluN3A are PDB ID codes 4KCC, 2A5S, 4KCD(A), respectively. Next, the lobe 1 Cα atoms of the reference structure were joined to the lobe 2 Cα atoms of each simulated conformer to construct an ensemble of pseudo-rigid-body structures. The ensembles for apo- and glycine-bound GluN1 include 22,262 and 7,007 conformers, respectively. The ensembles for apo- and glutamate-bound GluN2A include 12,685 and 7,436 conformers. The ensembles for apo- and glycine-bound GluN3A include 11,917 and 4,709 conformers. PCA calculations were performed using Bio3D (Grant et al., 2006). The axes of rotation characterizing PC1–PC3 were calculated using the DomainSelect method provided by the DynDom server (Hayward and Berendsen, 1998). Endpoint coordinates were generated using Bio3D. Lobe 1 is the ‘‘fixed’’ domain, and lobe 2 is the ‘‘moving’’ domain. For GluN1, lobe 1 is defined as residues 399–534 and 758–786, and lobe 2 is defined as residues 537–754. For GluN2A, lobe 1 is defined as residues 407–529 and 761–789, and lobe 2 is defined as residues 532–757. For GluN3A, lobe 1 is defined as residues 515–649 and 873–901, and lobe 2 is defined as residues 652–869.

4.4 Principal Component Analysis Results

The dominant three PCs that characterize interlobe conformational transitions are described for each of the LBDs (Figures 4-6; Table 1). For the apo LBDs, PC1 corresponds, as expected, to a hinge-bending motion (Figures 4A, 5C, 6A) and accounts for the majority of the proportion of variance in large-scale transitions, with additional eigenvectors accounting for increasingly smaller contributions (Table 1). PC2 corresponds to a sweeping motion for the apo GluN1 and GluN3A LBDs but a rocking motion for the apo GluN2A LBD (Figures 4B, 5D, 6B). PC3 corresponds to a twisting motion for the apo LBDs (Figures 4C, 5C, 6C). The difference between the sweeping and twisting motions is that the sweeping rotational axis falls ‘‘behind’’ lobe 2, whereas the twisting axis penetrates lobe 2. The first two eigenvectors have previously been computed for the apo GluN1 LBD (Kaye et al., 2006), and they are similar to the PCs described here.

Upon glycine or glutamate binding to the LBD, PC1 retains a hinge-bending motion for all LBDs except GluN3A, which converts to a rocking motion (Figures 4A, 5A, 6A). Upon glycine binding, PC2 converts from a sweeping to a rocking motion for GluN1 and from a sweeping to a hinge-bending motion for GluN3A (Figures 5D). By contrast, upon glutamate binding, PC2 retains rocking and sweeping motions for GluN2A (Figure 6). PC3 retains a twisting motion for all LBDs upon either glycine or glutamate binding (Figures 4-6), although the axis of rotation undergoes a tilt for the glycine-binding LBDs. Note that because the PCs were calculated separately for the apo- and glycine/ glutamate-bound LBDs, the same eigenvalue does not necessarily correspond to the same conformation. The proportion of variance accounted for by each of the different PCs is provided in Table 1.

In comparing the PC motions with (ξ_1,ξ_2), the hingebending motions generally fall along a positive-slope diagonal in (ξ_1,ξ_2), whereas the other PCs are described in part by configurations off this diagonal. The PMFs indicate that cleft opening appears to be skewed to be greater along ξ_1 than ξ_2 for the three NMDA receptor LBDs compared with GluA2. This skew is reflected in the tilt of the rotational axes corresponding to hinge bending, which is steeper for the glycine binding subunits.

4.5 Modelling of Principal Components within a GluN2A/GluN1 Tetramer

With the availability of a full length crystal structure of a GluN2B/GluN21 crystal structure, we can see how motions along the principal components we calculated for our LBDs affect their intra-tetramer differences (Lee et al. 2014).

The full length NMDA crystal structure consists of GluN1 in chains A and C, and GluN2B in chains B and D. For our model we superimposed the maxima and minima of our principal components on to the ligand binding domain for one of the appropriate chains. For GluN1 we modeled our PCs on chain A, and for GluN2A we superimposed our structures onto chain B. For GluN1 the distances were measured from the Cα of the 155th residue, to the Cα of glycine 728 in chain B, the Cα of glycine 740 in chain C, and the Cα of serine 736 in chain B. For GluN2A the distances were measured from the Cα atom of the 143rd residue, to the Cα of glycine 740 in chain C, the Cα of glycine 728 in chain C, and the Cα of glycine 740 in chain B. Distance was measured between the maxima and minima for the principal component and each chain.

The first principal component for GluN1, hinge-bending, mainly varies the distance between chain A and D, with a much smaller change for both the B and C chains [Figure 7]. The second principal component, sweeping, inverts this. PC2 for GluN1 in the apo state affects the distance from chain A to chain B or C to a greater extent than the A-D distance [Figure 8]. PC3 affects inter-lobe distances equally between all three chains and chain A [Figure 9].

Upon ligand binding we see the motions are damped in general, with our greatest amplitude of motion being 2.1 Å compared to 5.0 Å in the apo form. Glycine bound PC1 still mostly affects the A-D distance, with smaller contributions to A-C, and A-B [Figure 10]. PC2, which converts from sweeping in the apo state to rocking here, has a greater effect on the chain A to chain C and chain B distances, rather than the chain A to chain D distance [Figure 11]. PC3 has hardly any effect and inter-lobe distances, with its greatest amplitude of motion only being 0.5 Å between chain A and chain B [Figure 12].

The principal components of the apo form of GluN2A have a similar effect as the principal components of the apo form of GluN1. Hinge-bending primarily effects the B-C distance in the tetramer, with smaller contributions to B-D and B-A distances [Figure 13]. PC2 has almost no effect on B-C distance (-0.6 Å) with a much greater change in B-D and B-A distances, -2.5 Å and -2.6 Å respectively [Figure 14]. PC3 contributes little in the apo form, with its greatest amplitude being 0.5 Å for the B-C distance [Figure 15].

Glutamate binding has an effect on the magnitude of inter-lobe differences, but not on their distribution. Once again PC1 primarily affects B-C distance [Figure 16]. PC2 has a much greater effect on B-D and B-A distances, and a smaller one on the B-C distance [Figure 17]. PC3 once again has little effect on any inter-chain differences, with its greatest magnitude of motion being only 0.4 Å [Figure 18].

4.6 Discussion

The dominant three principal components for all four LBDs may be classified as hinge bending, sweeping, rocking, or twisting motions. For the apo LBDs, PC1 corresponds to hinge bending, and PC3 corresponds to twisting. PC2 corresponds to sweeping for all apo LBDs except GluN2A, which is rocking. The characteristic motion for PC2 therefore does not differentiate between glycine- and glutamate-binding LBDs. Upon glutamate binding to GluN2A, the characteristic motions for PC 1–3 remain the same. By contrast, many of these motions change upon glycine binding to GluN1 and GluN3A: sweeping converts to rocking for GluN1 (PC2), and for GluN3A, hinge bending goes to rocking (PC1), and sweeping to hinge bending (PC2). Additionally, the rotational axis for twisting undergoes a tilt (PC3). The different behaviors for the glycine- and glutamate-binding LBDs may result from the different binding site architectures and mechanics required to selectively bind glycine versus glutamate.

Looking at how these principal components effect inter-lobe distances, we can see that principal component 1, hinge-bending, has a much greater effect of changing the distance between the moving domain and one of its neighbors. In the case of the chain A GluN1, this neighbor is chain D GluN2B. In the case of GluN2A chain B, this neighbor is the chain C GluN1. The fact that the primary motion for both of these LBDs has a ‘preferred’ partner may tell us more about what possible interactions may be necessary to gate and desensitize these receptors. Looking further ahead, we may wish to look for interactions between these LBDs to try and observe possible interactions between these paired ligand binding domains.

Figure 1:

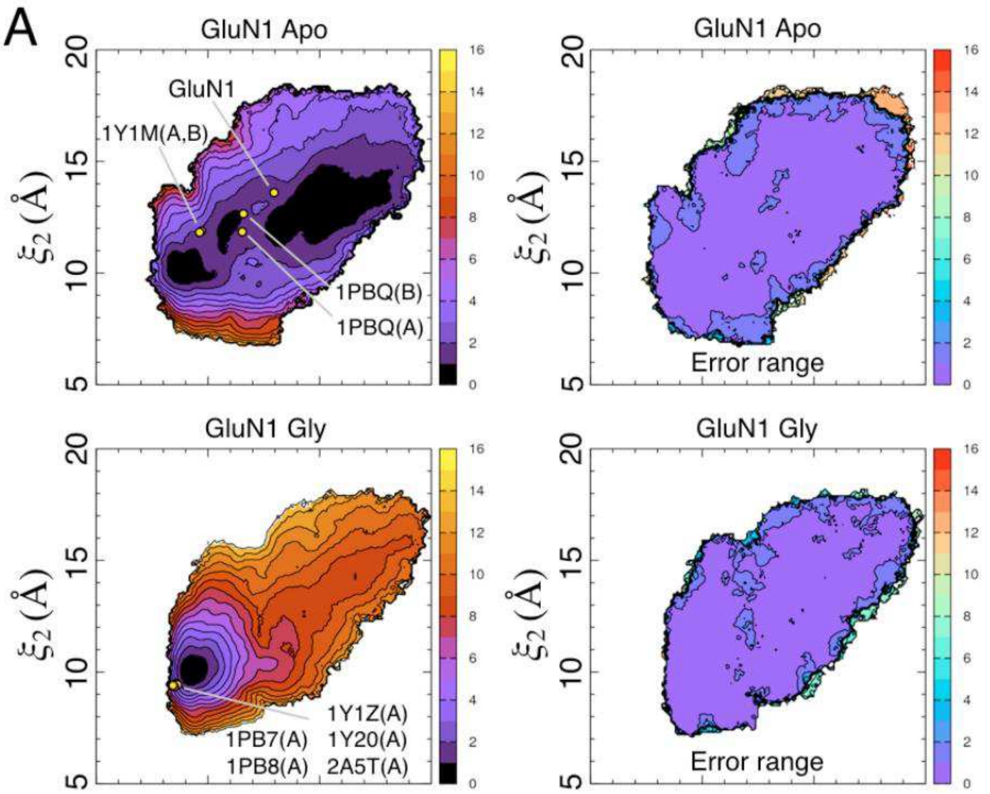

Fig.1. **PMFs and Bootstrapping results for GluN1 in the apo and glycine bound forms.**

PMF for the apo and glycine bound states of the GluN1 ligand binding domain are shown on the left. Contour lines correspond to a difference of 1 kcal/mol, with cooler colors being lower in free energy (see color bar). Crystal structures are shown as yellow dots along with their corresponding PDBids. On the right is the error range calculated through bootstrapping for each of the corresponding PMFs.

Figure 2:

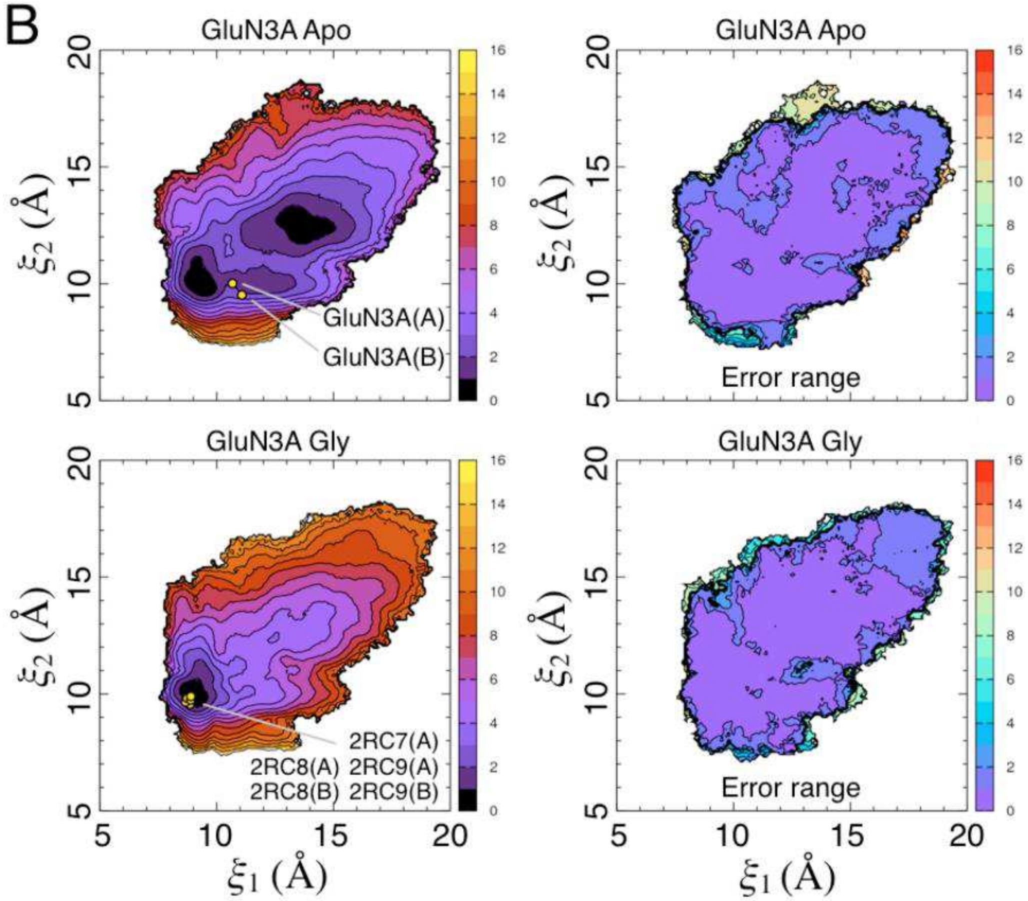

Fig.2. **PMFs and Bootstrapping results for GluN3A in the apo and glycine bound forms.**

PMF for the apo and glycine bound states of the GluN3A ligand binding domain are shown on the left. Contour lines correspond to a difference of 1 kcal/mol, with cooler colors being lower in free energy (see color bar). Crystal structures are shown as yellow dots along with their corresponding PDBids. On the right is the error range calculated through bootstrapping for each of the corresponding PMFs.

Figure 3

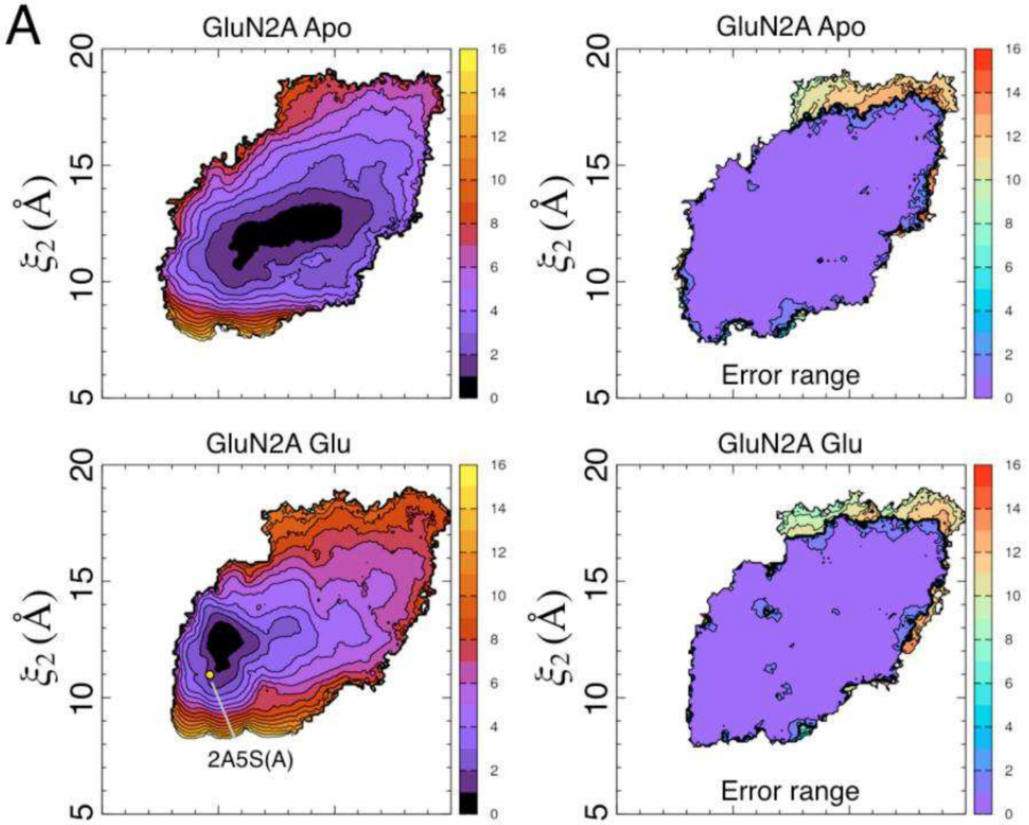

Fig.3. **PMFs and Bootstrapping results for GluN2A in the apo and glutamate bound forms.**

PMF for the apo and glutamate bound states of the GluN2A ligand binding domain are shown on the left. Contour lines correspond to a difference of 1 kcal/mol, with cooler colors being lower in free energy (see color bar). Crystal structures are shown as yellow dots along with their corresponding PDBids. On the right is the error range calculated through bootstrapping for each of the corresponding PMFs.

Figure 4: GluN1 Apo PCAs

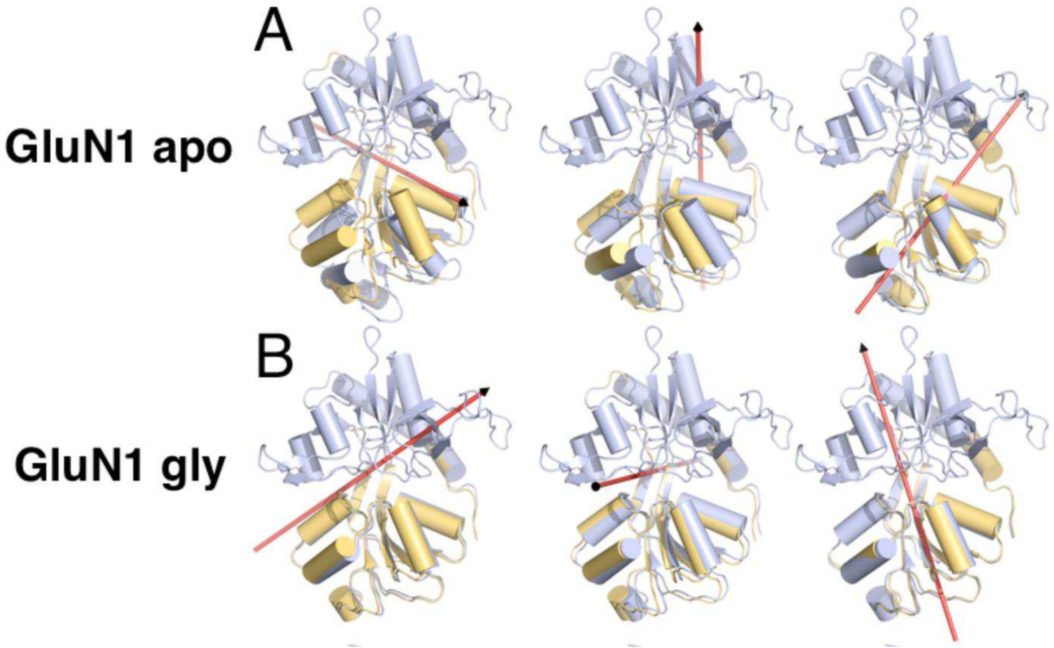

Fig.4. **Principal Component Analysis of GluN1 in the apo and glycine bound forms.**

Depiction of principal components for the GluN1 LBD in the apo and glycine bound forms. Blue and wheat structures represent the maxima of the motion, with the red arrow showing the axis of rotation.

Figure 5:

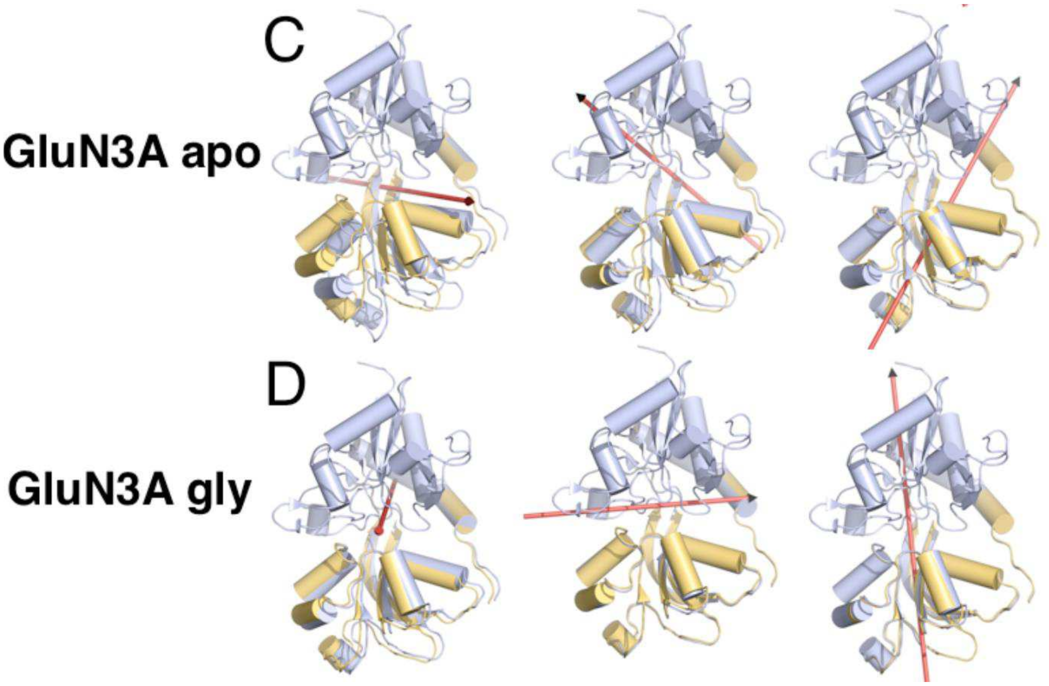

Fig.5. **Principal Component Analysis of GluN3A in the apo and glycine bound forms.**

Depiction of principal components for the GluN3A LBD in the apo and glycine bound forms. Blue and wheat structures represent the maxima of the motion, with the red arrow showing the axis of rotation.

Figure 6

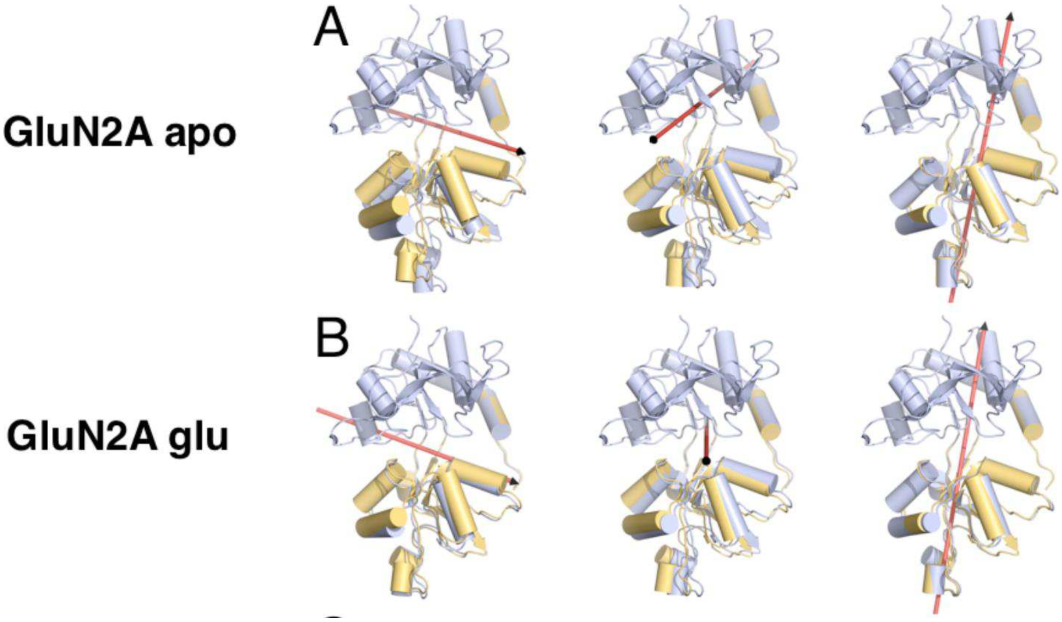

Fig.6. **Principal Component Analysis of GluN2A in the apo and glutamate bound forms.**

Depiction of principal components for the GluN2A LBD in the apo and glutmate bound forms. Blue and wheat structures represent the maxima of the motion, with the red arrow showing the axis of rotation.

Figure 7

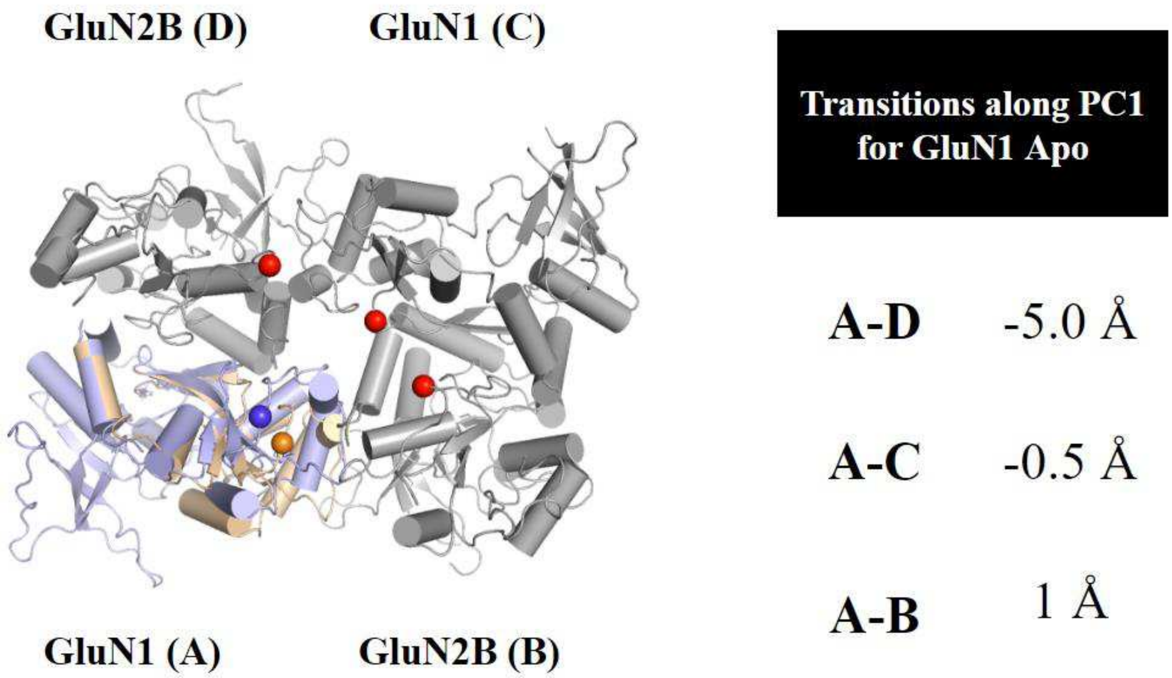

Fig.7. **Motions along the First Principal Component of GluN1 Apo Modeled on Tetramer Structure**

Maxima and minima, colored wheat and blue respectively, of GluN1 principal component 1, superimposed onto the ligand binding domain of chain A of the full length NMDA tetramer (PDBid: 4TLL) (Lee et al. 2014). Orange and blue dots are the Cα atoms of residue 155 in the GluN1 ligand binding domain. In chain D, red dot is the Cα of glycine 728. In chain C, red dot is the Cα of glycine 740. In chain B, red dot is the Cα of serine 736. Distance was measured between the maxima and minima for the principal component and each chain by using the aforementioned resides.

Figure 8

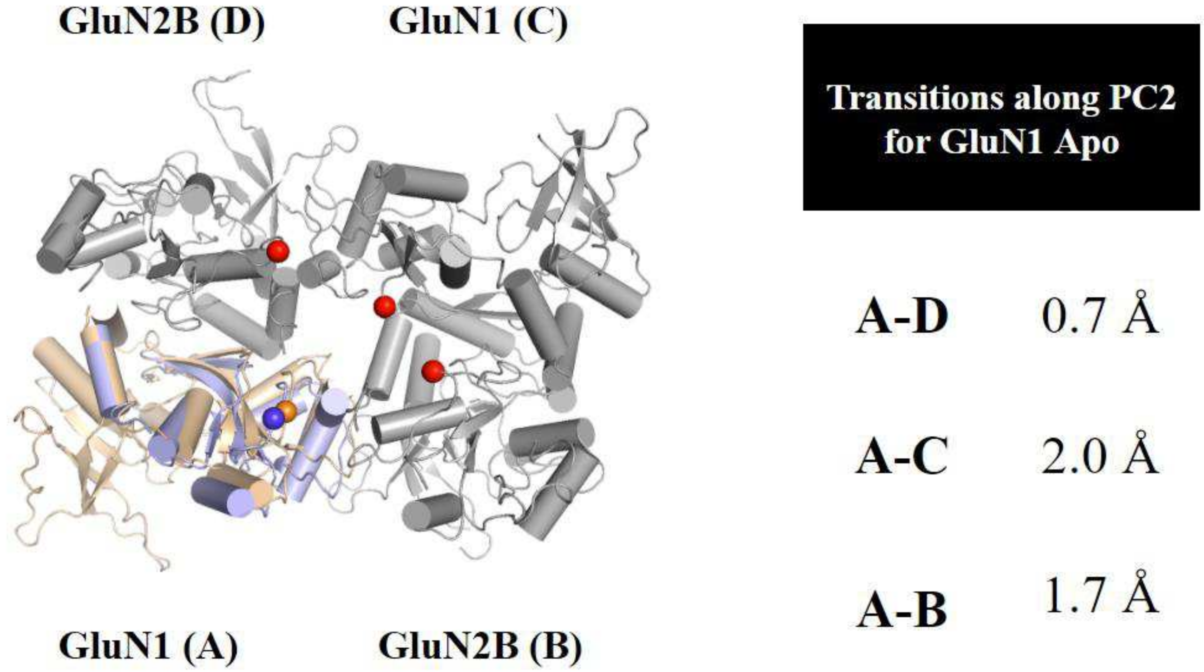

Fig.8. **Motions along the Second Principal Component of GluN1 Apo Modeled on Tetramer Structure**

Maxima and minima, colored wheat and blue respectively, of GluN1 principal component 2, superimposed onto the ligand binding domain of chain A of the full length NMDA tetramer (PDBid: 4TLL) (Lee et al. 2014). Orange and blue dots are the Cα atoms of residue 155 in the GluN1 ligand binding domain. In chain D, red dot is the Cα of glycine 728. In chain C, red dot is the Cα of glycine 740. In chain B, red dot is the Cα of serine 736. Distance was measured between the maxima and minima for the principal component and each chain. Distance was measured between the maxima and minima for the principal component and each chain by using the aforementioned resides.

Figure 9

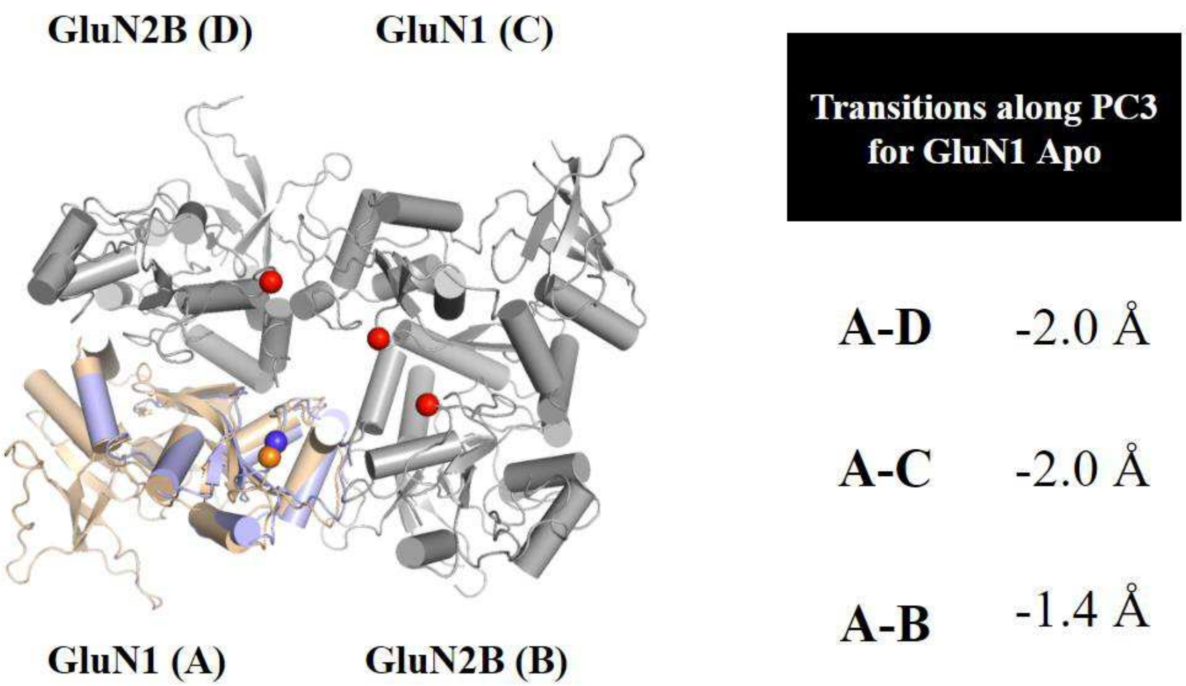

Fig.9. **Motions along the Third Principal Component of GluN1 Apo Modeled on Tetramer Structure**

Maxima and minima, colored wheat and blue respectively, of GluN1 principal component 3, superimposed onto the ligand binding domain of chain A of the full length NMDA tetramer (PDBid: 4TLL) (Lee et al. 2014). Orange and blue dots are the Cα atoms of residue 155 in the GluN1 ligand binding domain. In chain D, red dot is the Cα of glycine 728. In chain C, red dot is the Cα of glycine 740. In chain B, red dot is the Cα of serine 736. Distance was measured between the maxima and minima for the principal component and each chain. Distance was measured between the maxima and minima for the principal component and each chain by using the aforementioned resides.

Figure 10

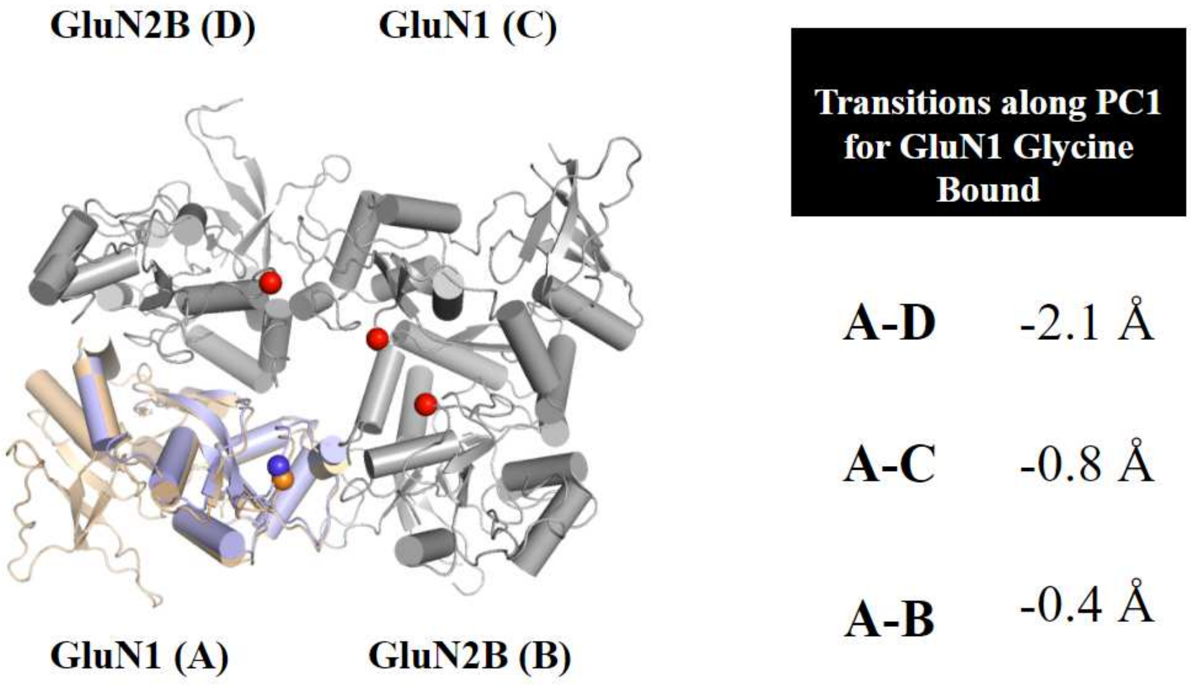

Fig.10. **Motions along the First Principal Component of GluN1 Glycine Bound Modeled on Tetramer Structure**

Maxima and minima, colored wheat and blue respectively, of GluN1 principal component 1, superimposed onto the ligand binding domain of chain A of the full length NMDA tetramer (PDBid: 4TLL) (Lee et al. 2014). Orange and blue dots are the Cα atoms of residue 155 in the GluN1 ligand binding domain. In chain D, red dot is the Cα of glycine 728. In chain C, red dot is the Cα of glycine 740. In chain B, red dot is the Cα of serine 736. Distance was measured between the maxima and minima for the principal component and each chain. Distance was measured between the maxima and minima for the principal component and each chain by using the aforementioned resides.

Figure 11

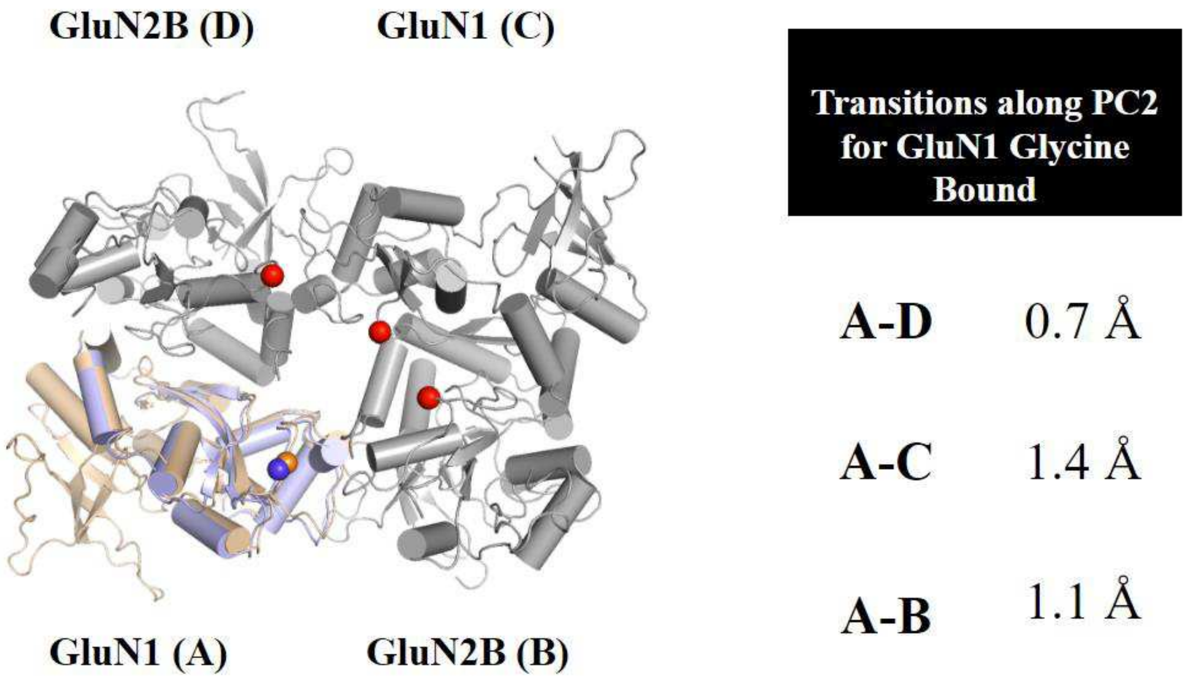

Fig.11. **Motions along the Second Principal Component of GluN1 Glycine Bound Modeled on Tetramer Structure**

Maxima and minima, colored wheat and blue respectively, of GluN1 principal component 2, superimposed onto the ligand binding domain of chain A of the full length NMDA tetramer (PDBid: 4TLL) (Lee et al. 2014). Orange and blue dots are the Cα atoms of residue 155 in the GluN1 ligand binding domain. In chain D, red dot is the Cα of glycine 728. In chain C, red dot is the Cα of glycine 740. In chain B, red dot is the Cα of serine 736. Distance was measured between the maxima and minima for the principal component and each chain. Distance was measured between the maxima and minima for the principal component and each chain by using the aforementioned resides.

Figure 12

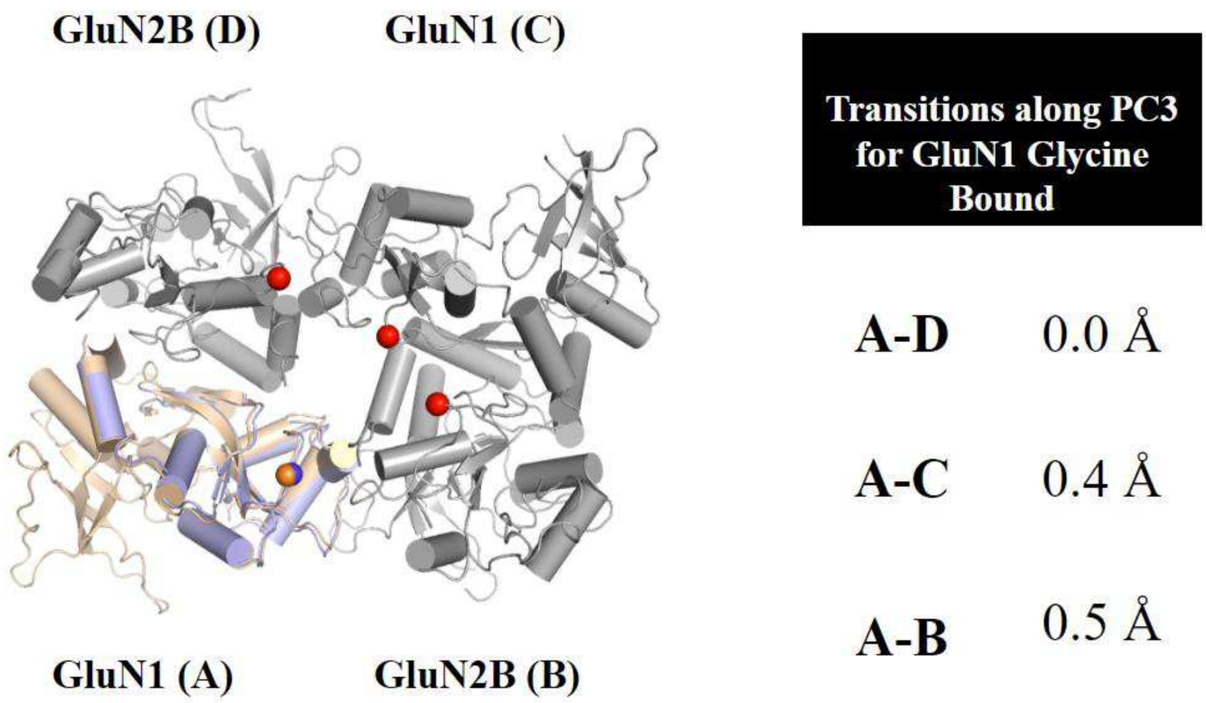

Fig.12. **Motions along the Third Principal Component of GluN1 Glycine Bound Modeled on Tetramer Structure**

Maxima and minima, colored wheat and blue respectively, of GluN1 principal component 3, superimposed onto the ligand binding domain of chain A of the full length NMDA tetramer (PDBid: 4TLL) (Lee et al. 2014). Orange and blue dots are the Cα atoms of residue 155 in the GluN1 ligand binding domain. In chain D, red dot is the Cα of glycine 728. In chain C, red dot is the Cα of glycine 740. In chain B, red dot is the Cα of serine 736. Distance was measured between the maxima and minima for the principal component and each chain. Distance was measured between the maxima and minima for the principal component and each chain by using the aforementioned resides.

Figure 13

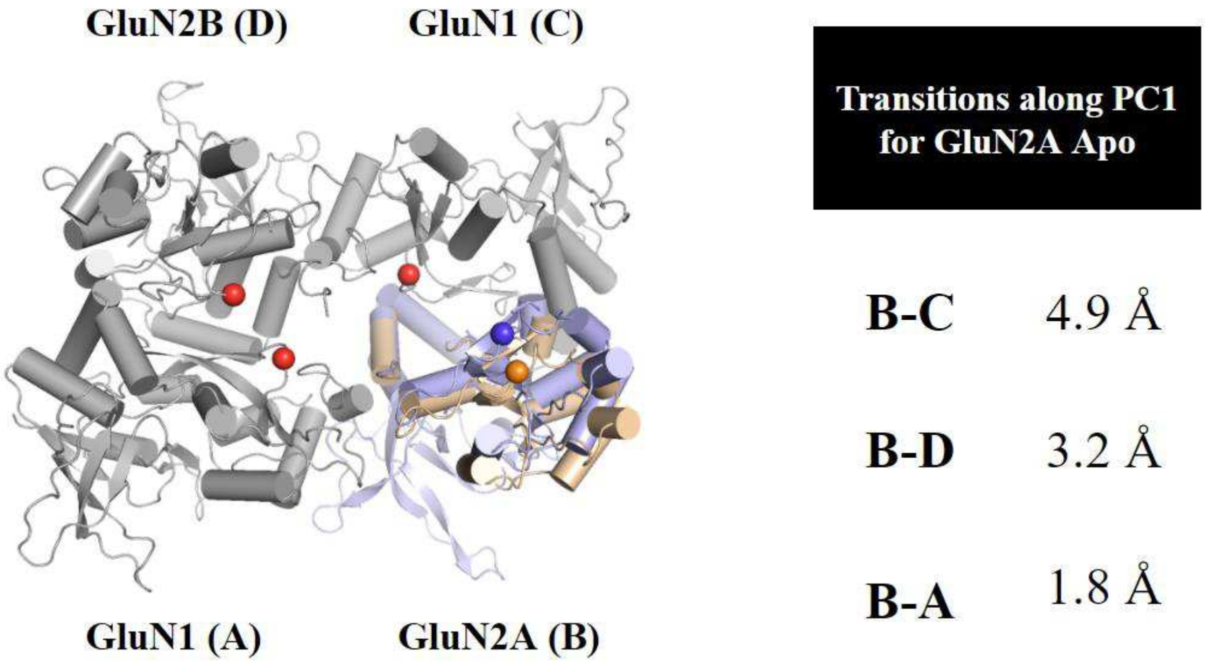

Fig.13. **Motions along the First Principal Component of GluN2A Apo Modeled on Tetramer Structure**

Maxima and minima, colored wheat and blue respectively, of GluN2A principal component 1, superimposed onto the ligand binding domain of chain B of the full length NMDA tetramer (PDBid: 4TLL) (Lee et al. 2014). Orange and blue dots are the Cα atoms of residue 143 in the GluN2A ligand binding domain. In chain A, red dot is the Cα of glycine 740. In chain C, red dot is the Cα of glycine 740. In chain D, red dot is the Cα of glycine 728. Distance was measured between the maxima and minima for the principal component and each chain. Distance was measured between the maxima and minima for the principal component and each chain by using the aforementioned resides.

Figure 14

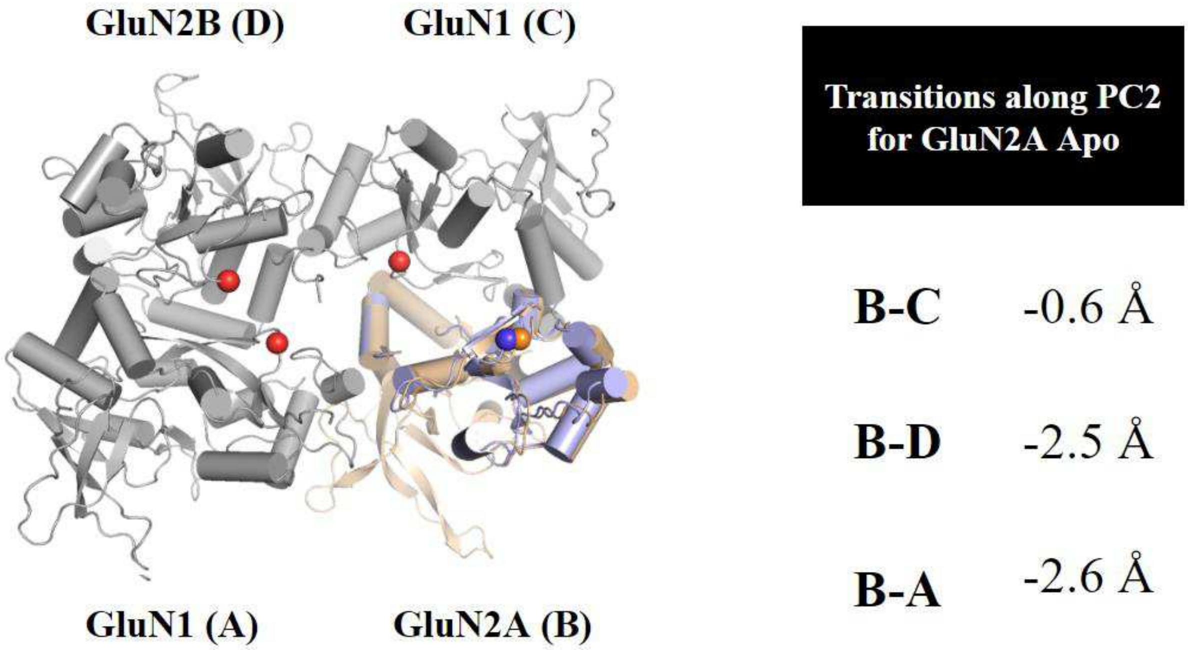

Fig.14. **Motions along the Second Principal Component of GluN2A Apo Modeled on Tetramer Structure**

Maxima and minima, colored wheat and blue respectively, of GluN2A principal component 2, superimposed onto the ligand binding domain of chain B of the full length NMDA tetramer (PDBid: 4TLL) (Lee et al. 2014). Orange and blue dots are the Cα atoms of residue 143 in the GluN2A ligand binding domain. In chain A, red dot is the Cα of glycine 740. In chain C, red dot is the Cα of glycine 740. In chain D, red dot is the Cα of glycine 728. Distance was measured between the maxima and minima for the principal component and each chain. Distance was measured between the maxima and minima for the principal component and each chain by using the aforementioned resides.

Figure 15

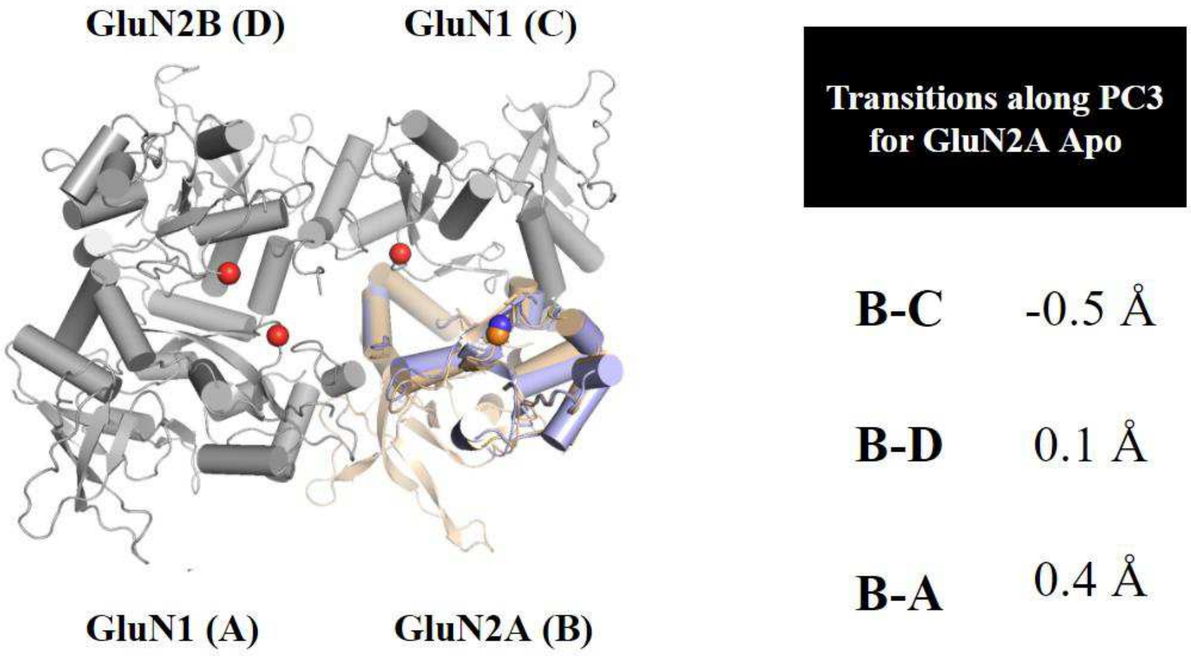

Fig.15. **Motions along the Third Principal Component of GluN2A Apo Modeled on Tetramer Structure**

Maxima and minima, colored wheat and blue respectively, of GluN2A principal component 1, superimposed onto the ligand binding domain of chain B of the full length NMDA tetramer (PDBid: 4TLL) (Lee et al. 2014). Orange and blue dots are the Cα atoms of residue 143 in the GluN2A ligand binding domain. In chain A, red dot is the Cα of glycine 740. In chain C, red dot is the Cα of glycine 740. In chain D, red dot is the Cα of glycine 728. Distance was measured between the maxima and minima for the principal component and each chain. Distance was measured between the maxima and minima for the principal component and each chain by using the aforementioned resides.

Figure 16

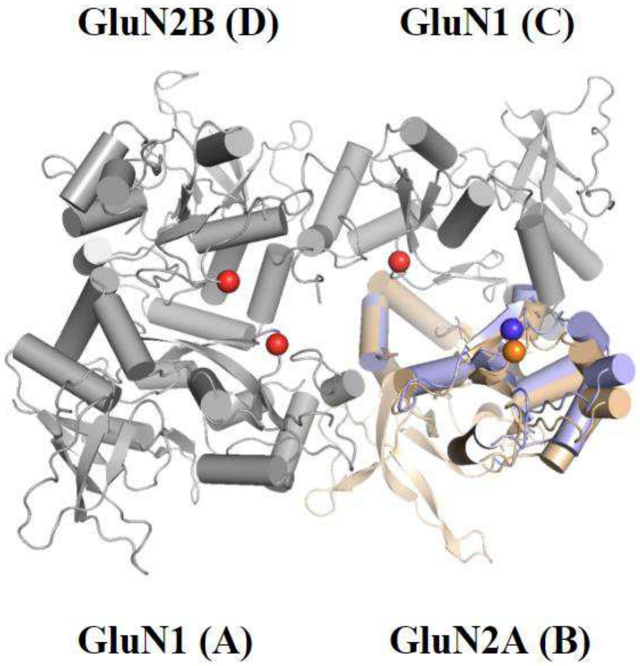

Transitions along PC1 for GluN2A Glutamate Bound

B-C	-2.1 Å
B-D	-0.8 Å
B-A	-0.4 Å

Fig.16. **Motions along the First Principal Component of GluN2A Glutamate Bound Modeled on Tetramer Structure**

Maxima and minima, colored wheat and blue respectively, of GluN2A principal component 1, superimposed onto the ligand binding domain of chain B of the full length NMDA tetramer (PDBid: 4TLL) (Lee et al. 2014). Orange and blue dots are the Cα atoms of residue 143 in the GluN2A ligand binding domain. In chain A, red dot is the Cα of glycine 740. In chain C, red dot is the Cα of glycine 740. In chain D, red dot is the Cα of glycine 728. Distance was measured between the maxima and minima for the principal component and each chain. Distance was measured between the maxima and minima for the principal component and each chain by using the aforementioned resides.

Figure 17

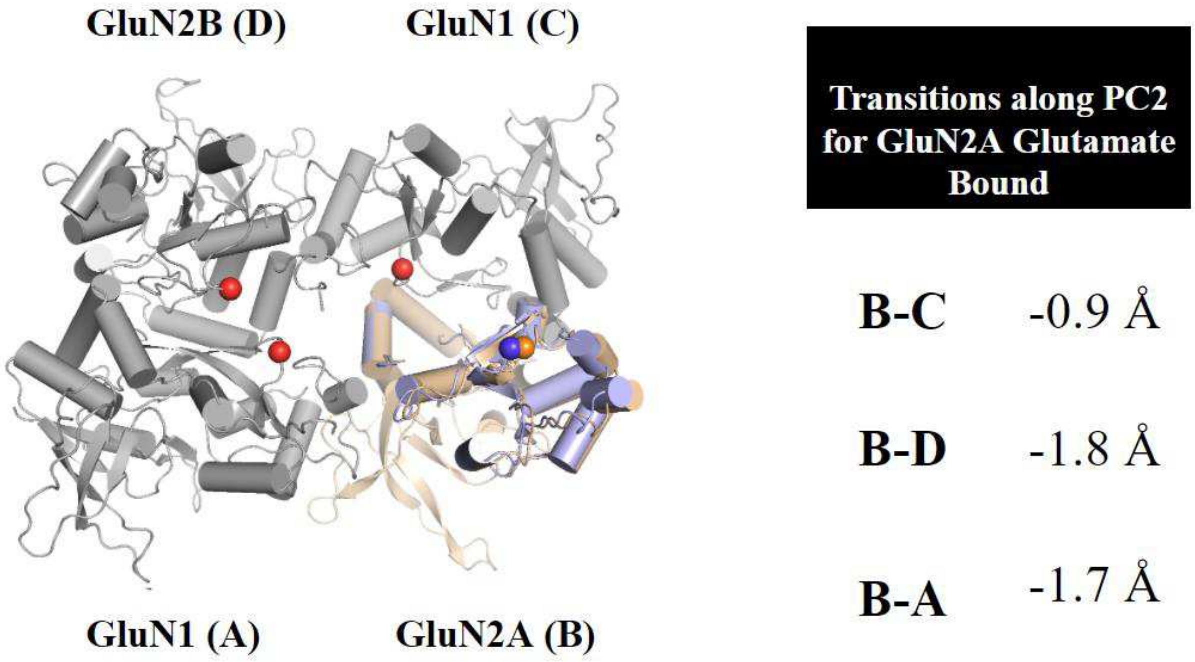

Fig.17. **Motions along the Second Principal Component of GluN2A Glutamate Bound Modeled on Tetramer Structure**

Maxima and minima, colored wheat and blue respectively, of GluN2A principal component 2, superimposed onto the ligand binding domain of chain B of the full length NMDA tetramer (PDBid: 4TLL) (Lee et al. 2014). Orange and blue dots are the Cα atoms of residue 143 in the GluN2A ligand binding domain. In chain A, red dot is the Cα of glycine 740. In chain C, red dot is the Cα of glycine 740. In chain D, red dot is the Cα of glycine 728. Distance was measured between the maxima and minima for the principal component and each chain. Distance was measured between the maxima and minima for the principal component and each chain by using the aforementioned resides.

Figure 18

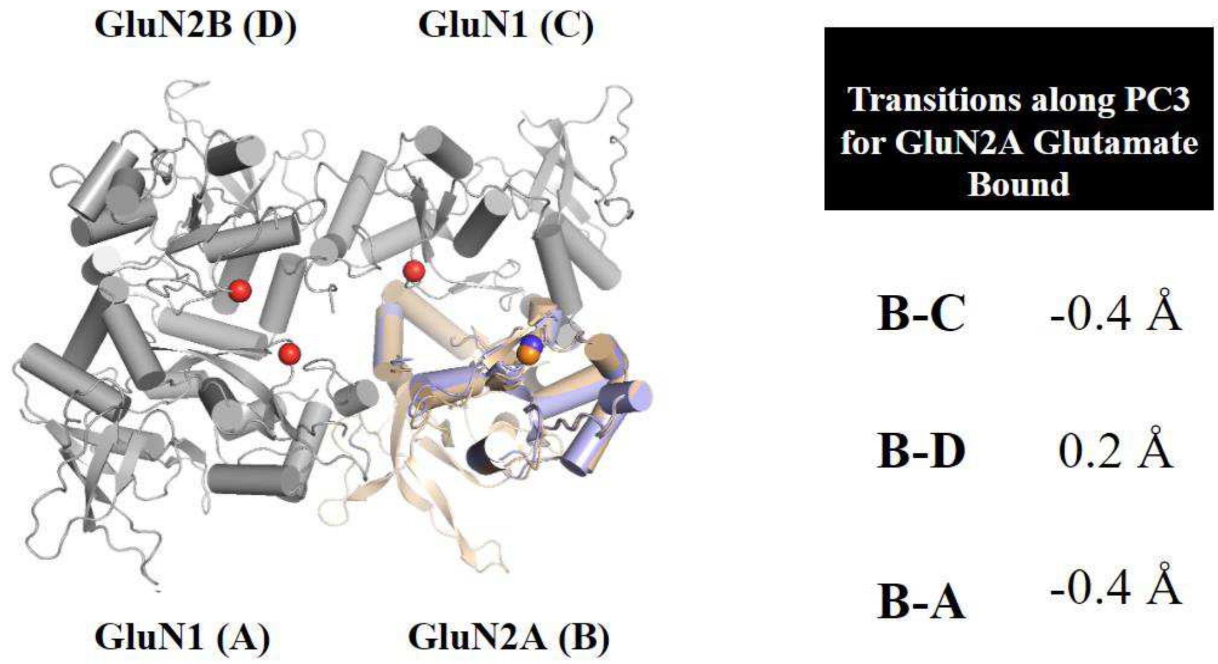

Fig.18. **Motions along the Third Principal Component of GluN2A Glutamate Bound Modeled on Tetramer Structure**

Maxima and minima, colored wheat and blue respectively, of GluN2A principal component 3, superimposed onto the ligand binding domain of chain B of the full length NMDA tetramer (PDBid: 4TLL) (Lee et al. 2014). Orange and blue dots are the Cα atoms of residue 143 in the GluN2A ligand binding domain. In chain A, red dot is the Cα of glycine 740. In chain C, red dot is the Cα of glycine 740. In chain D, red dot is the Cα of glycine 728. Distance was measured between the maxima and minima for the principal component and each chain. Distance was measured between the maxima and minima for the principal component and each chain by using the aforementioned resides.

Table 1

	PC1	PC2	PC3
GluN1 - Apo	69.4	20.1	4.2
GluN1 – Gly	27.5	21.5	13.3
GluN2A – Apo	70.8	15.8	4.5
GluN2A – Glu	53.9	18.1	7.3
GluN3A – Apo	74.1	13.2	4.2
GluN3A – Gly	30.3	23.3	9.1

Table 1. **Contribution to variance by each principal component**

Chapter 5: Future Directions

5.1 GluR0 Future Directions

Further work on GluR0 should focus on three things: working on making a SAXS measurement of the monomer, observing how glutamate and other agonists bind to the ligand binding domain, and looking at how the dimer interface affects the energy landscape available

Ideally we would measure a monomeric version of the GluR0 LBD to complement our experimental work. Currently we believe that the presence of dimer within our SAXS measurements is preventing our theoretical results from matching up with our experimental ones. There are a few ways to approach this problem. First, we could try making measurements at lower concentrations of protein. Our current SAXS experiments have a minimum protein concentration of 3 mgs/mL. Lowering that concentration could push more of the signal to come from the monomer, although it is likely that we would need to return to SIBLYS to measure what may be a low signal. In addition to lowering the amount of protein in our SAXS experiments, we can look at making mutations that will disrupt the dimer interface. Work has been done on GluR0 derived from another organism, Nostoc punctiforme, another cyanobacteria (Lee et al. 2008). It has been found that a one amino acid switch, a glutamate to a lysine, completely abolishes dimerization, as observed through analytical ultracentrifugation (Lee et al. 2008). This NPGluR0 however, does have a different dimer interface than our synechococcus GluR0, with a lower dissociation constant of 15.4 mM as compared to our SGluR0 dissociation constant of 0.8 μM (Lee et al. 2008). Despite their differences, we may be able to use the NPGluR0 dimer interface as a model to mutate our SGluR0 into a form that does not strongly dimerize in solution.

Another interesting question to consider with regards to the GluR0 LBD, is how it acts in a dimer. Because this prokaryotic glutamate receptor lacks the amino terminal domain of its eukaryotic counterparts, much of the assembly of the extracellular domain is left to the LBDs themselves. In addition to lacking the aid of the amino terminal domain in assembling the receptor, the dimer interface of GluR0 is believed to only involve amino acids on the upper lobe (Mayer et al. 2001). Looking at how our PMFs change in the presence of the GluR0 dimer would be instructive on explaining some of the behavior of GluR0 electrophysiology experiments. While we observe a flexible LBD that can access both open and closed states, the dimer interface may prevent the apo form from accessing either. Similar arguments can be made for the glutamate and serine bound forms. Ultimately, in looking only at the monomer, we are looking at the GluR0 LBD in its simplest state. Understanding how these receptors work requires looking at them in their physiological state, and for GluR0 that means scaling up the monomer simulation into a dimer.

A final question is how glutamate binds into the GluR0 ligand binding domain. Previous studies done in the lab (Yu and Lau 2017) have shown how binding of the ligand to the LBD can be guided by residues outside of the binding pocket. Using both the string method (Meng et al. 2016) and large scale simulations such as those on ANTON, we can see if the prokaryotic glutamate receptor uses a similar binding path, or if there are multiple ways to steer glutamate into the binding pocket. Comparing the glutamate binding pathway with the serine binding pathway would allow us to see if

GluR0 binding partners share binding pathway, or if binding multiple ligands means there are multiple paths to the bound state.

5.2 GluA2 Future Directions

Future work on GluA2 needs to do three things: verify that our AUC measurements are being done on the dimer state of GluA2 in both mutants, derive more accurate frictional ratios by performing global fits on the AUC data, and use the AUC data to construct more accurate shape models for our GluA2 mutants.

The first step is to verify that our AUC results are for the GluA2 dimer. As described in chapter 3, performing the same experiments in the presence of reducing agents should eliminate the disulfide bonds holding our LBDs together. We expect that we would then see a more slowly sedimenting species appear in our AUC runs, corresponding to a higher presence of GluA2 monomer. This difference should be much more noticeable in the triple mutant than in the L483Y, with its lower affinity for dimerization.

Frictional ratios cannot be accurately calculated from only one sedimentation velocity experiment (Brown and Schuck 2006). Global fits of f/f_0 are necessary in order to improve the resolution of our frictional ratio values. More sedimentation velocity experiments, ones in which the concentration of protein and the speed of the rotor are varied, are needed. These global fits should improve the resolution of our f/f_0, and enable us to differentiate between the two mutants and the wild type GluA2.

Further work on GluA2 would involve more shape determining experiments done on the dimer. The first would be to use previous work done using SAXS to generate a bead model of the dimer and compare the various mutants and the wild type to see how the envelope changes. These changes could then be checked against sedimentation velocity experiments to ensure their accuracy.

5.3 GluN Future Directions

In chapter 4 we showed how the motions along the principal components of GluN1 and GluN2B affect distances between ligand binding domains in the tetramer, and thus how these motions may contribute to the function of the receptor. A future analysis is super imposing GluN3 onto the GluN1 chains of the full length structure. Although both are glycine binding domains, the tetramers they form with the glutamate binding NMDA receptors have several differences in receptor properties (Low and Wee 2010). Assuming that GluN3 and GluN1 assemble in similar ways with GluN2B, we may be able to see if some of these differences are the result of motions along any of the principal components.

Bibliography

Armstrong N, Gouaux E, Mechanisms for Activation and Antagonism of an AMPA-Sensitive Glutamate Receptor: Crystal Structures of the GluR2 Ligand Binding Core, *Neuron*, Volume 28, Issue 1, 2000, Pages 165-181, ISSN 0896-6273

Bigge CF, Ionotropic glutamate receptors, *Current Opinion in Chemical Biology*, Volume 3, Issue 4, 1999, Pages 441-447, ISSN 1367-5931

Bjerrum EJ, Biggin PC. Rigid body essential X-ray crystallography: distinguishing the bend and twist of glutamate receptor ligand binding domains. Proteins. 2008;72:434–446.

Box GEP, Jenkins GM, Reinsel GC. Time series analysis: forecasting and control. Hoboken, N.J: John Wiley; 2008.

Boczko EM, Brooks CL III Constant-Temperature Free Energy Surfaces for Physical and Chemical Processes. *J Phys Chem* 1993;97:4509–4513

Brown PH, Schuck P. Macromolecular Size-and-Shape Distributions by Sedimentation Velocity Analytical Ultracentrifugation. *Biophysical Journal*. 2006;90(12):4651-4661. doi:10.1529/biophysj.106.081372.

Chaudhry C., Plested A.J.R., Schuck P., Mayer M.L. 2009a. Energetics of glutamate receptor ligand binding domain dimer assembly are modulated by allosteric ions. Proc. Natl. Acad. Sci. USA.106:12329–12334

Chen GQ, Cui C, Mayer ML and Gouaux E. Functional characterization of a potassium-selective prokaryotic glutamate receptor *Nature* 402, 817-821 16 December 1999

Cheng Q, Thiran S, Yernool D, Gouaux E, Jayaraman V. A vibrational spectroscopic investigation of interactions of agonists with GluR0, a prokaryotic glutamate receptor. Biochemistry. 2002 Feb 5;41(5):1602-8.

Choi YB, Lipton SA Identification and Mechanism of Action of Two Histidine Residues Underlying High-Affinity Zn2+ Inhibition of the NMDA Receptor *Neuron* 1999 Volume 23 , Issue 1 , 171 – 180

Cole JL, Lary JW, Moody T, Laue TM. Analytical Ultracentrifugation: Sedimentation Velocity and Sedimentation Equilibrium. *Methods in cell biology*. 2008;84:143-179. doi:10.1016/S0091-679X(07)84006-4.

Dingledine R, Borges K, Bowie D and Traynelis SF The Glutamate Receptor Ion Channels *Pharmacological Reviews* March 1999, 51 (1) 7-62

Ferrenberg AM, Swendsen RH Optimized Monte Carlo data analysis. *Phys Rev Lett* 1989;63:1195–1198

Fiser A, Do RK, and Sali A. Modeling of loops in protein structures, Protein Science 9. 1753-1773, 2000.

Franke D, Svergun DI. DAMMIF, a program for rapid ab-initio shape determination in small-angle scattering. *Journal of Applied Crystallography*. 2009;42(Pt 2):342-346. doi:10.1107/S0021889809000338

Freire E. Statistical thermodynamic linkage between conformational and binding equilibria. Adv Protein Chem. 1998;51:255–279.

Furukawa H, Gouaux E (2003) Mechanisms of activation, inhibition and specificity: crystal structures of the NMDA receptor NR1 ligand-binding core. EMBO J 22(12): 2873–2885

Furukawa H. Structure and function of glutamate receptor amino terminal domains. *The Journal of Physiology*. 2012;590(Pt 1):63-72. doi:10.1113/jphysiol.2011.213850.

García AE. Large-amplitude nonlinear motions in proteins. Phys Rev Lett. 1992;68:2696–2699.

Gielen M, Retchless BS, Mony L, Johnson JW, Paoletti P. Mechanism of differential control of NMDA receptor activity by NR2 subunits. *Nature*. 2009;459(7247):703-707. doi:10.1038/nature07993.

Grant, Rodrigues, ElSawy, McCammon, Caves, Bio3D: An R package for the comparative analysis of protein structures. *Bioinformatics* 2006;22, 2695-2696

Grossfield, A., and Zuckerman, D.M. Quantifying uncertainty and sampling quality in biomolecular simulations. *Annu. Rep. Comput. Chem*. 2009;5, 23–48.

Hansen KB, Yuan H, Traynelis SF. Structural aspects of AMPA receptor activation, desensitization and deactivation. Curr Opin Neurobiol. 2007;17:281–288.

Haydyn D.T. Mertens, Dmitri I. Svergun, Structural characterization of proteins and complexes using small-angle X-ray solution scattering, *Journal of Structural Biology*, Volume 172, Issue 1, 2010, Pages 128-141, ISSN 1047-8477, https://doi.org/10.1016/j.jsb.2010.06.012

Hayward, S., and Berendsen, H.J. Systematic analysis of domain motions in proteins from conformational change: new results on citrate synthase and T4 lysozyme. *Proteins* 1998;30, 144–154

Horning MS, Mayer ML (2004) Regulation of AMPA receptor gating by ligand binding core dimers. Neuron 41(3):379–388.

Howlett GJ, Minton AP, Rivas G (2006) Analytical ultracentrifugation for the study of protein association and assembly. Curr Opin Chem Biol 10: 430–436.

Institute of Medicine (US) Forum on Neuroscience and Nervous System Disorders. *Glutamate-Related Biomarkers in Drug Development for Disorders of the Nervous System: Workshop Summary*. Washington (DC): National Academies Press (US); 2011. 2, Overview of the Glutamatergic System.

Jacques DA, Trewhella J. Small-angle scattering for structural biology—Expanding the frontier while avoiding the pitfalls*. Protein Science : A Publication of the Protein Society*. 2010;19(4):642-657. doi:10.1002/pro.351

Karakas E, Regan MC, Furukawa H. Emerging structural insights into the function of ionotropic glutamate receptors *Trends in Biochemical Sciences* Volume 40, Issue 6, 2015 Pages 328-337

Kästner J Umbrella sampling. *WIREs Comput Mol Sci* 2011;1(6):932–942

Kaye SL, Sansom MSP, Biggin PC. Molecular dynamics simulations of the ligand-binding domain of an N-methyl-D-aspartate receptor. J Biol Chem. 2006;281:12736–12742.

Kikhney Alexey G. and Svergun Dmitri I. (2015), A practical guide to small angle X-ray scattering (SAXS) of flexible and intrinsically disordered proteins, *FEBS Letters*, 589, doi: 10.1016/j.febslet.2015.08.027

Kirkwood JG Statistical mechanics of fluid mixtures. *J Chem Phys* 1935;3:300

Krieger J, Bahar I, Greger IH. Structure, Dynamics, and Allosteric Potential of Ionotropic Glutamate Receptor N-Terminal Domains. *Biophysical Journal*. 2015;109(6):1136-1148. doi:10.1016/j.bpj.2015.06.061.

Kumar S, Bouzida D, Swendsen RH, Kollman PA, Rosenberg JM The weighted histogram analysis method for free-energy calculations on biomolecules. I. The method. *J Comp Chem* 19923;13:1011–1021

Lebowitz J, Lewis MS, Schuck P. Modern analytical ultracentrifugation in protein science: A tutorial review. *Protein Science : A Publication of the Protein Society*. 2002;11(9):2067-2079.

Lee, J.H., Kang, G.B., Lim, H.H., Jin, K.S., Kim, S.H., Ree, M., Park, C.S., Kim, S.J., and Eom, S.H. (2008). Crystal structure of the GluR0 ligand-binding core from Nostoc punctiforme in complex with L-glutamate: structural dissection of the ligand interaction and subunit interface. J. Mol. Biol. 376, 308–316.

Lee C-H, Lü W, Michel JC, et al. NMDA receptor structures reveal subunit arrangement and pore architecture. *Nature*. 2014;511(7508):191-197. doi:10.1038/nature13548.

Levy, R.M., Srinivasan, A.R., Olson, W.K., and McCammon, J.A. Quasiharmonic method for studying very low frequency modes in proteins. *Biopolymers* 1984;23, 1099–1112

Low CM, Zheng F, Lyuboslavsky P, Traynelis SF Molecular determinants of coordinated proton and zinc inhibition of *N*-methyl-D-aspartate NR1/NR2A receptors *Proceedings of the National Academy of Sciences* Sep 2000, 97 (20) 11062-11067; DOI:10.1073/pnas.180307497

Low, CM, Wee, KS (2010) New insights into the not-so-new NR3 subunits of *N*-methyl-d-aspartate receptor: localization, structure, and function. Mol Pharmacol 78:1–11.

Ma B, Kumar S, Tsai CJ, Nussinov R. Folding funnels and binding mechanisms. Protein Eng. 1999;12:713–720

Mayer ML, Olson R, Gouaux E, Mechanisms for ligand binding to GluR0 ion channels: crystal structures of the glutamate and serine complexes and a closed apo state *Journal of Molecular Biology*, Volume 311, Issue 4, 2001, Pages 815-836, ISSN 0022-2836, https://doi.org/10.1006/jmbi.2001.4884.

Mayer ML. Emerging models of glutamate receptor ion channel structure and function. Structure. 2011;19:1370–1380

Meyerson JR, Kumar J, Chittori S, et al. Structural mechanism of glutamate receptor activation and desensitization. *Nature*. 2014;514(7522):328-334. doi:10.1038/nature13603.

Meng, Y.; Shukla, D.; Pande, V. S.; Roux, B. Transition Path Theory Analysis of c-Src Kinase Activation Proc. *Natl. Acad. Sci. U. S. A*. 2016, 113, 9193– 9198 DOI: 10.1073/pnas.1602790113S

Monod J, Wyman J, Changeux JP. On the nature of allosteric transitions: a plausible model. J Mol Biol. 1965;12:88–118

Pøhlsgaard J, Frydenvang K, Madsen U, Kastrup JS. Lessons from more than 80 structures of the GluA2 ligand-binding domain in complex with agonists, antagonists and allosteric modulators. Neuropharmacology. 2011;60:135–150.

Purves D, Augustine GJ, Fitzpatrick D, et al., editors. *Neuroscience*. 2nd edition. Sunderland (MA): Sinauer Associates; 2001. Summation of Synaptic Potentials

Ptak CP, Hsieh C-L, Weiland GA, Oswald RE. Role of Stoichiometry in the Dimer-Stabilizing Effect of AMPA Receptor Allosteric Modulators. *ACS Chemical Biology*. 2014;9(1):128-133. doi:10.1021/cb4007166.

Roux B The calculation of the potential of mean force using computer simulations. *Comput Phys Commun* 1995;91:275–282

Sali A amd Blundell TL. Comparative protein modelling by satisfaction of spatial restraints. J. Mol. Biol. 234, 779-815, 1993.

Schauder DM, Kuybeda O, Zhang J, et al. Glutamate receptor desensitization is mediated by changes in quaternary structure of the ligand binding domain. Proceedings of the National Academy of Sciences of the United States of America. 2013;110(15):5921-5926. doi:10.1073/pnas.1217549110.

Schneidman-Duhovny D, Hammel M, Tainer JA, and Sali A. Accurate SAXS profile computation and its assessment by contrast variation experiments. *Biophysical Journal* 2013. 105 (4), 962-974

Schneidman-Duhovny D, Hammel M, Tainer JA, and Sali A. FoXS, FoXSDock and MultiFoXS: Single-state and multi-state structural modeling of proteins and their complexes based on SAXS profiles *NAR* 2016

Shepherd J.D., Huganir R.L. The cell biology of synaptic plasticity: AMPA receptor trafficking. Annu. Rev. Cell Dev. Biol. 2007;23:613–643

Stawski P, Janovjak H, Trauner D. Pharmacology of ionotropic glutamate receptors: A structural perspective. Bioorg Med Chem. 2010;18:7759–7772.

Svergun DI. Restoring low resolution structure of biological macromolecules from solution scattering using simulated annealing. *Biophysical Journal*. 1999;76(6):2879-2886.

Torrie GM, Valleau JP Monte-Carlo free energy estimates using non-Boltzmann sampling. Application to the subcritical Lennard-Jones fluid. *Chem Phys Lett* 1974;28(4):578–581

Wang Q, Canutescu AA, Dunbrack RL. SCWRL and MolIDE: Computer programs for side-chain conformation prediction and homology modeling. *Nature protocols*. 2008;3(12):1832-1847. doi:10.1038/nprot.2008.184.

Weston M.C., Schuck P., Ghosal A., Rosenmund C., Mayer M.L. 2006. Conformational restriction blocks glutamate receptor desensitization. Nat. Struct. Mol. Biol. 13:1120–1127

Yalini A, Biggin PC, Shrivastava IH. and Sansom M A prokaryotic glutamate receptor: homology modelling and molecular dynamics simulations of GluR0 2003 FEBS Letters, 553,

Yao Y, Belcher J, Berger AJ, Mayer ML, Lau AY, Conformational Analysis of NMDA Receptor GluN1, GluN2, and GluN3 Ligand-Binding Domains Reveals Subtype-Specific Characteristics, *Structure*, Volume 21, Issue 10, 2013, Pages 1788-1799, ISSN 0969-2126, https://doi.org/10.1016/j.str.2013.07.011.

Yu A and Lau AY Energetics of Glutamate Binding to an Ionotropic Glutamate Receptor *The Journal of Physical Chemistry B* 2017 121 (46), 10436-10442

Yuan H, Hansen KB, Vance KM, Ogden KK, Traynelis SF. Control of *N*-methyl-D-aspartate Receptor Function by the NR2 Subunit Amino-Terminal Domain. *The Journal of neuroscience : the official journal of the Society for Neuroscience*. 2009;29(39):12045-12058. doi:10.1523/JNEUROSCI.1365-09.2009.

Zhu F, Hummer G. Convergence and error estimation in free energy calculations using the weighted histogram analysis method. *J Comput Chem.* 2012;33(4):453–465

JOHN BELCHER

3601 Greenway #908, Baltimore, MD 21218 | 210-831--8897 | jbelche1@jhu.edu

EDUCATION

Johns Hopkins School of Medicine Baltimore MD
PhD in Molecular Biophysics **2018**
Dissertation: "Computational and Experimental Analysis of Glutamate Receptor Ligand Binding Domains"

University of Texas at San Antonio
B.S. in Physics **2009**
Minor: Mathematics
Cum Laude

AWARDS

Francis D. Carlson Fellowship	2010 – 2012
GEBS Summer Scholar	2009
Ronald E. McNair Scholar	2008 – 2009

PRESENTATIONS

Computational and Experimental Studies of a Prokaryotic Glutamate Receptor
Platform speaker at 60th Annual Meeting of the Biophysical Society 2016

Principal Component Analysis of Glutamate Receptor Ligand Binding Domains
Poster presented at 58th Annual Meeting of the Biophysical Society 2014

Molecular Mechanisms of Glutamate Receptor Activation and Regulation
Poster presented at 57th Annual Meeting of the Biophysical Society 2013

Molecular Mechanisms of Glutamate Receptor Activation and Regulation
Poster presented at HHMI Conference on Structural Biology of Membrance Proteins 2013

Structural Thermodynamics of NMDA Receptor Ligand Binding Domains
Poster presented at 56th Annual Meeting of the Biophysical Society 2012

PUBLICATIONS

Yu A, Weid T, **Belcher J**, Lau AY. (2015) "Computing Conformational Free Energies of iGluR Ligand-Binding Domains." In: Ionotropic Glutamate Receptor Technologies., Popescu GK ed., NeuroMethods Springer pg. 119-132

Yao Y*, **Belcher J***, Berger AJ, Mayer ML, Lau AY. (2013) Conformational Analysis of NMDA Receptor GluN1, GluN2, and GluN3 Ligand-Binding Domains Reveals Subtype-Specific Characteristics. Structure. Oct 8;21(10) pg. 1788-1799. PMID: 23972471

Valdez R, Johnson EM, **Belcher J**, Fuini JF, Brancaleon L. (2009) Porphyrins Affect The Self-Assembly of Tubulin in Solution. Biophysical Chemistry. Dec;145(2-3) pg. 98-104. PMID: 19819610

Belcher J, Sansone S, Fernandez NF, Haskins WE and Brancaleon L. (2009) Photoinduced Unfolding of Lactoglobulin Mediated by a Water-Soluble Porphyrin. J. Phys. Chem. B. Apr 30;113 pg. 6020-30. PMID: 1935116

*denotes equal contribution to authorship

MEMBERSHIPS

Biophysical Society